Nordic Concrete
Research

NCF Nordic Concrete Federation

NORDIC CONCRETE RESEARCH

Preface

Sustainability is the key word for the current society and this is also reflected in both the concrete industry and the concrete research. There are several ways to reduce the environmental footprint from the concrete industry and this is of vital importance since the cement production stands for a substantial part of the global carbon dioxide emissions. In this volume of *Nordic Concrete Research* (NCR) almost all papers are devoted to sustainability in some way. Deterioration mechanisms and durability have been extensively researched during more than 50 years in the Nordic countries aiming at prolonging the service life of concrete structures and this volume contains five papers on various aspects of this subject. Another two papers are devoted to alternative binders which currently constitute the main solution to reducing carbon dioxide emissions. The last paper discusses a matter that has importance for using more prestressed concrete structures. The prestressing leads to a more favourable use of the concrete that in turn leads to material savings.

Another aspect of sustainability is the transfer from publishing on paper to electronically publishing leading to substantial savings of trees and woods. NCR is currently in this process through a co-operation with the publishing company De Gruyter. As the loyal reader of NCR knows, the Nordic Concrete Federation and its Research Committee, that also constitutes the Editorial Board of NCR, have decided that NCR shall transfer from a paper journal to an electronic journal, where readers may read all papers free of charge. This system is called "Open Access" and is recommended by both universities and research councils to facilitate dissemination of new knowledge. Thereby, we are confident that NCR will attract both more authors and more readers. Due to highly appreciated financial support from the Nordic cement industry, also submitting papers will be free of charge.

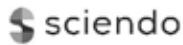Stockholm in December 2018

Johan Silfwerbrand
Editor of NCR

PUBLICATION NO. 59   2/2018

CONTENTS

$ sciendo

The Influence of Production Parameters on Pozzolanic Reactivity of Calcined Clays

Tobias Danner
PhD
Researcher
SINTEF Building and Infrastructure
Pb 4760 Torgarden,
7465 Trondheim, Norway tobiasdanner@sintef.no

Harald Justnes
PhD
Chief Scientist
SINTEF Building and Infrastructure
Pb 4760 Torgarden,
7465 Trondheim, Norway
harald.justnes@sintef.no

ABSTRACT
Calcined clays are gaining increasing interest as future supplementary cementitious materials for the production of blended cements. Besides the mineralogy, the right production conditions can affect the pozzolanic activity of calcined clays. In this paper, the pozzolanic reactivity of two calcined natural clays in dependence of burning temperature, residence time in the furnace, cooling conditions and particle size of the final product is investigated. The highest pozzolanic reactivity was found at calcination temperatures between 600 and 800°C. While different cooling conditions had no identified effect on reactivity, decreased particle size and residence time increased the reactivity.

Key words: Calcined clay, pozzolana, lime consumption, heating, particle size.

1.   INTRODUCTION

Portland cement is the key binder for concrete production. However, cement production is a highly energy intensive process which emits around 900 kg CO_2 for every ton clinker produced [1]. The cement industry was identified to be the amongst the largest carbon dioxide emitters with about 5-7% of the total global CO_2 emissions [2]. About 60% of the CO_2 emissions derive from the decomposition of limestone during firing. The remaining 40% are combustion related emissions like the use of fossil fuels as well as the energy requirement during processes like drying and grinding [3]. Possible measures to reduce these CO_2 emissions are (1) improvement of energy efficiency of cement plants; (2) utilization of alternative fuels; (3) carbon dioxide capture and (4) producing blended cements with less clinker content [4-6]. In the short term, the most promising approach to lower CO_2 emissions from the cement industry is the production of blended cements. i.e. replacing increasing amounts of cement clinker with supplementary cementitious materials e.g. calcined clays [7]. Reducing the amount of cement clinker by e.g. calcined clays in binders, directly reduces the CO_2 emissions associated with clinker productions. Additionally, the production of calcined clays happens at lower temperatures compared to cement and less energy is required for grinding calcined clay lumps.

The most commonly used supplementary cementitious materials (SCMs) in the cement industry today are granulated blast furnace slag (GBFS) from the steel industry and fly ash from coal power plants. These SCMs proved suitable to reduce the clinker content while maintaining or enhancing the properties of the final product. However, the availability of these materials is potentially getting limited and cannot meet the future demand of the large cement industry on a sustained basis. As these materials derive from processes associated with CO_2 emissions themselves, their supply may drop in the long-run when coal fired power plants and blast furnace plants are replaced by less CO_2 intensive processes [6, 8]. Consequently, for the long term the right choice of the replacing material is mainly a question of availability [9].

Natural pozzolanic materials like clays are a promising alternative SCMs as they are abundant and widespread with huge deposits distributed all over the world. Mining and transportation costs would be rather low so that these materials have the potential to serve the cement industry sufficiently for a sustainable future. Still, clays are very complex materials regarding the chemical and mineralogical composition. It is well known, that the right calcination temperature to produce reactive calcined clays depends a lot on the clay mineralogy [10-14]. Depending on the mineral composition, calcination at temperatures usually between 600 and 800°C, leads to the formation of an active metastable state with high pozzolanic activity [10, 11]. Kaolinite clays show higher pozzolanic reactivity than smectite or illite clays. The clays presented in this study have been investigated by the present authors in earlier studies. It was shown that replacement of up to 50% cement by calcined clay can result in equal or higher 28 day compressive strength [10, 15-19].

Besides the mineralogy and calcination temperature, other parameters during production potentially influence the reactivity of the final product. In addition to calcination temperature, this paper focuses on the effect of cooling rate, residence time in the furnace and particle size after milling, on the pozzolanic reactivity of two natural calcined clays. The understanding of the effect of these parameters can contribute to optimisation of potential industrial scale production of calcined clays.

2.   MATERIALS AND METHODS

2.1   Materials

Tables 1 and 2 show the bulk mineralogy of crystalline phases and the chemical composition of the two investigated clays. In earlier work on the pozzolanic activity of 7 different clays, Clay A and Clay B showed highest reactivity [10] and were therefore chosen for further investigations on the impact of production parameters. The main mineral phases of Clay A are kaolinite, quartz and feldspar. Clay B is a smectite rich clay with about 25% calcite. Calcined Clay B has been extensively studied by the present authors and was published under the name "calcined marl" for simplicity [15-19]. However, it should actually be categorized as "calcareous mudstone". Clay B is a tertiary sediment and was deposited between the middle and late Eocene (56 to 33.9 million years ago) in a marine depositional environment [20]. The calcite content derives to a large portion from coccoliths.

Calcium hydroxide ($Ca(OH)_2$) used in lime consumption tests was laboratory grade from Merck company.

Table 1 - Mineralogical composition of the raw clays in weight%.

Phase	A (%)	B (%)
Kaolinite	46.7	8.4
Smectite	—	53.5
Illite	—	4.4
Muscovite	1.5	
Quartz	17.5	4.3
K-feldspar	34.3	—
Calcite	—	24.7
Siderite	—	3.1
Pyrite	—	1.3

Table 2 - Chemical composition of the investigated clays in weight%.

Oxide	A (%)	B (%)
SiO_2	60.6	48.7
Al_2O_3	30.0	17.8
Fe_2O_3	3.4	10.4
CaO	0.1	13.8
K_2O	3.2	2.4
Na_2O	—	0.7
MgO	0.4	2.8
MnO	0.0	0.2
P_2O_5	0.10	0.2
TiO_2	0.4	1.0

2.2   Methods

A detailed characterisation of the raw and calcined clays including quantitative X-Ray powder diffraction (XRPD) using the Rietveld method, infrared spectroscopy (FT-IR), scanning electron microscopy (SEM), nuclear magnetic resonance spectroscopy (NMR) and møssbauer spectroscopy is presented in [21]. The mineralogical analysis of the raw clays (Table 1) was performed with XRD. The bulk mineralogy of Clay A and B was determined on dried and

ground samples using the back-loading technique. The $\leq 2\,\mu m$ fraction (clay fraction) was separated from the bulk by sedimentation, smeared on a glass plate and dried in air. The clay fraction was then investigated under three different conditions (a-c); a: untreated, b: after treatment with ethylene glycol vapours in a desiccator for 24 h at 60°C, c: after heating at 500 °C for 1 h. For analysis, a PAN Analytical X'Pert Pro MPD equipped with an X'Celerator RTMS detector, an automatic divergence slit and a Cu-K<alpha> X-ray source was used. The samples were measured from 2 to 65° 2θ using a step size of 0.0170° 2θ and a step time of 20 s. Data were collected at 45 kV and 40 mA. More details on the procedure of quantitative mineralogical analysis can be found in [22, 23].

XRPD was also used to qualitatively analyse the calcined clay samples and check possible differences in the phase assemblage in dependence of the different burning conditions. Here, XRPD measurements were done with a D8 Focus from Bruker, equipped with a Cu Kα X-Ray source and Lynx Eye detector. Data were collected with a step size of 0.2° 2Theta and a time of 1 s per step.

The chemical composition (Table 2) of the investigated clays was measured with X-Ray fluorescence (XRF) using a Bruker AXS S8 Tiger WDXRF instrument. Dried and powdered clay samples were ignited at 850 °C. Then 0.5 g of the dried clay sample was added to 5.0 g of a 2:1 mix of lithium- tetraborate and metaborate and 60 μg of lithium iodide. The mixture was fused in a Pt crucible and moulded to a glass disk.

Samples of about 15 g raw Clay A or Clay B were burned at different temperatures in a laboratory electrical furnace. Raw clay was weight in a platinum crucibles and placed in a chamber furnace from Nabertherm (Model: LH 60/14) at temperatures between 400 and 1100°C. The clays were placed directly into the furnace at the desired burning temperature.

To test the effect of cooling rate on the pozzolanic reactivity, the clays were hold for 2 h at constant temperature. After heating, one sample was taken out of the furnace and quenched in air for immediate cooling. A second sample was left in the furnace to cool down slowly to room temperature overnight.

To test the effect of particle size on the pozzolanic reactivity, half the amount of the clays, burned under the same conditions as mentioned above, was milled down to <50 μm. The remaining amount was milled down to particle sizes <10 μm. Milling of the calcined samples was done by hand using an agate mortar. The clay powder was milled and sieved until the desired particle size was reached. Only particles passing the sieve with a 50 and 10 μm mesh size respectively, were used for the tests.

To test the effect of heating rate on the pozzolanic activity, an additional set of samples was hold in the furnace for 30 min at a given temperature. The samples burned for 30 min were cooled down rapidly as described above and milled down to <10 μm.

To investigate the pozzolanic activity of the calcined clays, pastes of calcined clay and calcium hydroxide (Ca(OH)$_2$) were mixed. From here, the term lime will be used for Ca(OH)$_2$. Pastes were mixed in a calcined clay/lime ratio of 1/1 and a water to binder ratio of about 0.9. To simulate pore solution of cement pastes an alkaline solution of pH 13.2 and a KOH/NaOH ratio of 2/1 was used as mixing water. The pastes were mixed by hand during 60 s and transferred into glass bottles. The sealed glass bottles were cured during 28 days at 20°C. After 28 day curing the hydration was stopped by solvent exchange. Pastes were crushed and washed with

ethanol several times. The filtrated powder was dried in a closed desiccator at 35% RH upon saturated $CaCl_2$ solution. The amount of lime left in the pastes after 28 days was measured with thermogravimetric analysis (TG). The lime consumption gives a direct correlation to the pozzolanic activity of the calcined clays.

TG analysis was performed with a Mettler Toledo TGA/SDTA 851. First, samples were dried at 40°C for two hours in the TG apparatus. In a second step, the samples were heated from 40 to 1100°C with a heating rate of 10°C/min. The purge gas was in both steps nitrogen (N_2) with a flow of 30 ml/min. The decomposition of $Ca(OH)_2$ takes place between 450 and 550°C and shows in a clear weight loss. By measuring this weight loss the remaining $Ca(OH)_2$ content after 28 days relative to the content in the initial mixture was calculated. The exact boundaries for the temperature interval of $Ca(OH)_2$ were read from the 1st derivative curve of thermogravimetric analysis (DTG). The weight loss calculated from the difference of the horizontal tangents in the TG signal was multiplied with the molar ratio 74/18 for $Ca(OH)_2$ and H_2O, respectively.

3. RESULTS AND DISCUSSION

3.1 Effect of cooling rate on the pozzolanic activity

Figure 1 and 2 show the XRD diffractograms of Clay A and Clay B calcined between 400 and 1100°C. In both cases the clays were hold for 2 h in the furnace at a given temperature and then taken out from the furnace and quenched in air, i.e. fast cooling. In case of Clay A there was no difference detectable in the crystalline phase assemblage between the fast and slow cooled samples. Kaolinite disappeared above 600°C. This might be due to dehydroxylation of the clay mineral structure and transformation to metakaolin [11]. Muscovite peaks are visible up to 1000°C. Feldspar and quartz were not affected by the heat treatment up to 1000°C. At 1100°C recrystallization of mullite was observed. Recrystallization of other high temperature phases was not observed.
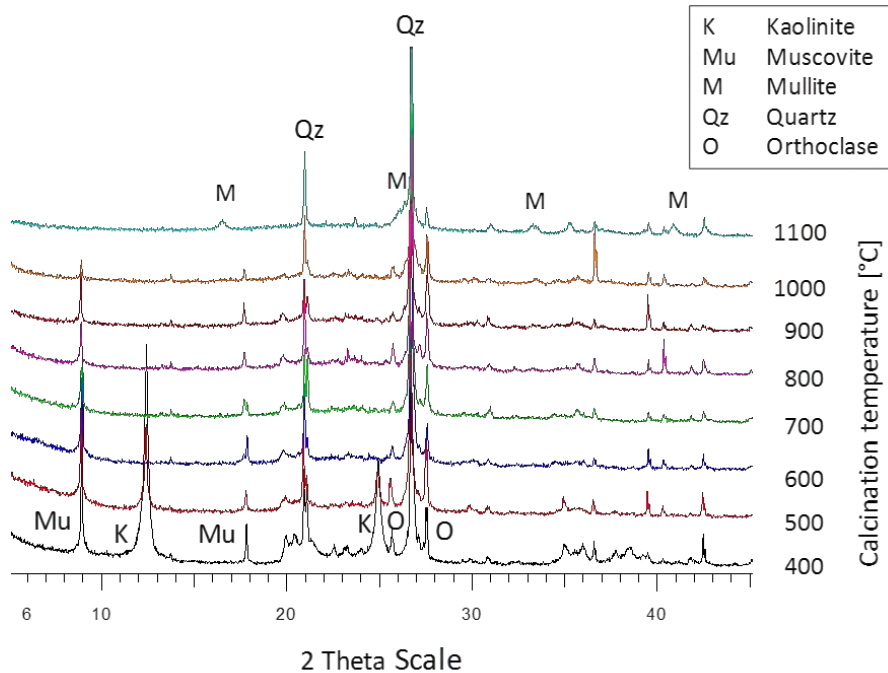
Figure 1 - XRD diffractograms of Clay A burned between 400 and 1100°C with fast cooling.

In case of Clay B, minor differences were observed in the phase assemblage of the fast and slow cooled samples. At 800°C calcite was completely decomposed in both samples. The main calcite peak at 29.4° 2Theta was visible until 700°C. The smectite peak at about 9° 2Theta steadily decreased from 400 to 800°C and completely disappeared at 900°C. It can be seen that the smectite peak is at about the same 2Theta angle than the muscovite peak in Clay A. Originally, non dried smectite shows a main peak at about 6° 2Theta. However, due to drying and the loss of interlayer water the distance between the different layers in the smectite structure decreases, causing a peak shift to higher 2 Theta values. Recrystallization of anorthite, diopside - wollastonite and hematite was detected between 900 and 1100°C. Gehlenite was only found as anintermediate phase at 1000°C in the fast cooled sample. Gehlenite might be a metastable phase transforming to more stable phases like anorthite when cooled down slowly [10]. The intense peaks at ~ 21 and 43° 2Theta in the sample calcined at 700°C belong to quartz (Figure 2). The high intensity in just this sample might be be explained with an effect called spottiness, i.e. large quartz grains in diffraction position.
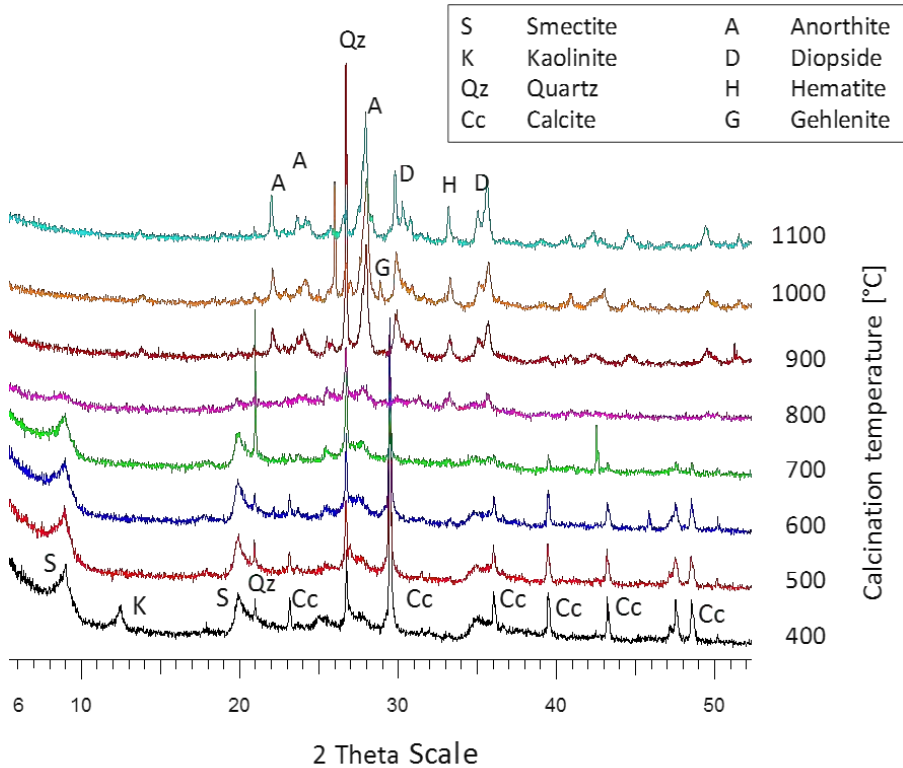
Figure 2 - XRD diffractograms of Clay B burned between 400 and 1100°C with fast cooling.

The lime consumption of fast and slowly cooled Clay A and Clay B burned between 400 and 1000°C is shown in Figure 3. Here, all clays were milled to a particle size <10 μm. The accuracy of the lime consumption values is about 5% [10]. The reactivity of both clays seemed not be affected by slow or fast cooling. Clay A showed the highest pozzolanic reactivity between 600 and 800°C with a lime consumption between 0.61 and 0.64 g lime/g clay. The low reactivity at 400 and 500°C might be due to the not yet dehydroxylated kaolinite and hence the incomplete transformation to metastable metakaolin. At a calcination temperature above 900°C the reactivity decreased as a result of starting recrystallization of new stable phases. In earlier investigations [10] it was suggested that to reach the maximum pozzolanic reactivity of Clay B, calcite should not be completely decomposed. This was confirmed in Figure 3. At 700°C, when calcite is still present to a certain amount, the pozzolanic reactivity is higher, compared to the sample calcined at 800°C. At 800°C, calcite was completely decomposed (Figure 2). The considerable drop in pozzolanic reactivity from 800 to 900°C was due to recrystallization of high temperature phases (Figure 2). It can be seen that Clay A in total has a higher pozzolanic reactivity with higher lime consumption than Clay B. This is because kaolinite clay minerals are more reactive than smectite clay minerals when calcined [11].

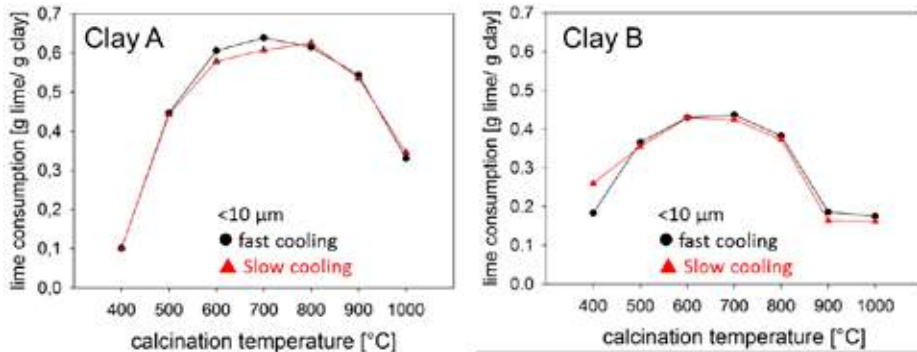*Figure 3 - Lime consumption in g lime/g clay for Clay A and Clay B burned between 400 and 1000°C with fast and slow cooling. Particle size was <10 μm.*

3.2 Effect of residence time on the pozzolanic activity

Figure 4 shows the comparison of the lime consumption of Clay A and Clay B calcined for 120 min and 30 min between 400 to 1000°C. New samples were produced with shorter residence time of 30 min. The new samples were burned from 400 to 900°C in steps of 50°C. All samples were *rapidly* cooled and milled down to particle sizes <10 μm.

In case of Clay A, a shorter residence time of 30 min increased the pozzolanic reactivity by about 0.1 g lime/g clay between 550 to 650°C. It is also shown that the lime consumption was rather stable between 550 and 900°C. In earlier investigations it was shown that lime consumption of the investigated clays shows a good correlation to 28 day compressive strength of mortars with 20% replacement of cement by calcined clay [10]. A lime consumption of about 0.7 g lime/g clay of Clay A corresponded to a compressive strength increase of about 15% when 20% cement was replaced with calcined Clay A [10]. Taking this correlation into account, we can assume that Clay A can be burned in this wide temperature range with a relatively short residence time in the kiln, without changing its pozzolanic properties in cementitious systems considerably. This can be important for production, where minor temperature variations should not have a big effect on the final product.

In case of Clay B, the pozzolanic reactivity increased slightly when calcined with lower residence times of 30 min. The reactivity had a peak at 650°C and decreased continuously above that temperature. This shows that Clay B is more sensitive to temperature with a narrower window of highest reactivity.
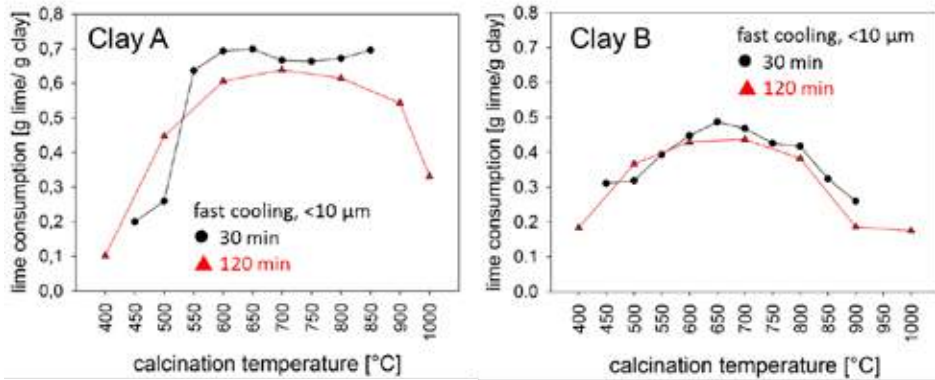
Figure 4 - Lime consumption in g lime/g clay for Clay A and Clay B burned between 400 and 1000°C with a residence time of 30 and 120 min in the furnace.

3.3   Effect of particle size on the pozzolanic activity

Figure 5 and 6 show the lime consumption of slowly and rapidly cooled Clay A and Clay B, respectively, as a function of their particle size. For both calcined clays the finer ground samples showed higher pozzolanic reactivity. In case of Clay A the lime consumption was increased by about 0.1 g lime/g clay (20% increase) when the particle size was decreased from <50 to <10 μm. For Clay B (Figure 6) the difference in lime consumption was even higher between the fine and coarse ground samples. In the Clay B samples with particle sizes <50 μm, the lime consumption was almost constant between 500 and 800°C.
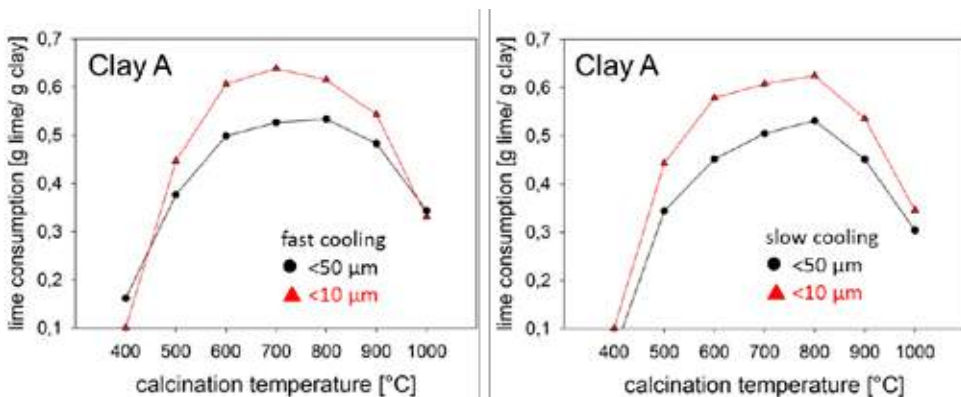
Figure 5 - Lime consumption in g lime/g clay for Clay A burned between 400 and 1000°C with fast (left) and slow cooling (right) and milled down to <50 μm and <10 μm.
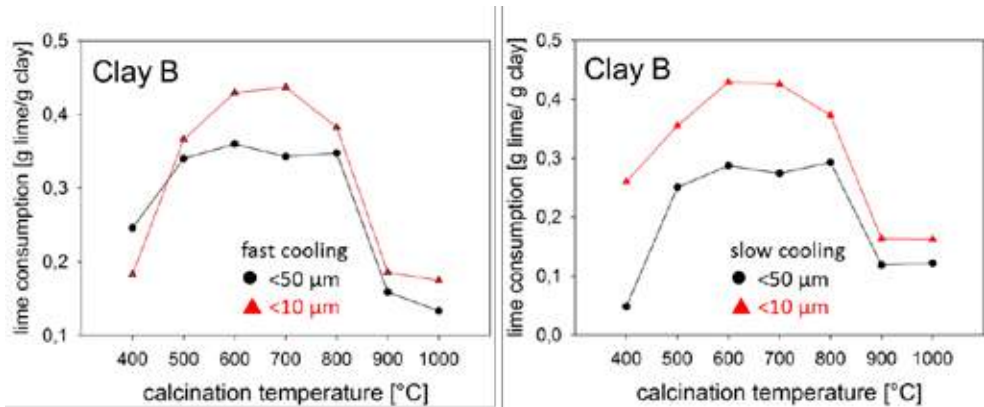
Figure 6 - Lime consumption in g lime/g clay for Clay A burned between 400 and 1000°C with fast (left) and slow cooling (right) and milled down to <50 μm and <10 μm.

4.   CONCLUSIONS

In this paper, the pozzolanic reactivity of two natural calcined clays was investigated in dependence of calcination temperature, cooling rate, residence time and particle size after milling. The obtained results give valuable contributions to an optimisation of a potential industrial scale production of calcined clays. The main results are listed below:

- Both calcined clays showed highest pozolanic reactivity between 600 and 800°C
- The kaolinite rich clay showed higher pozzolanic reactivity than the smectite rich clay.
- The cooling rate had no identified effect on the pozzolanic reactivity of the calcined clays.
- A decreased residence time from 120 to 30 minutes increased the pozzolanic reactivity.
- Particle size (<10 μm) had the strongest effect on the pozzolanic reactivity. A smaller particle size increased the pozzolanic reactivity of calcined clays.

REFERENCES

1.   Hasanbeigi A, Menke C & Price L, "The CO_2 abatement cost curve for the Thailand cement industry," *Journal of Cleaner Production*, Vol. 15, 2010, pp. 1509-1518.
2.   Benhelal E: "Global strategies and potentials to curb CO_2 emissions in cement industry," *Journal of Cleaner Production*, Vol 51, 2013, pp. 142-161.

3.   World Business Council for Sustainable Development (WBCS): "Cement Industry Energy and CO_2 Performance - Getting the numbers right," 2011, Geneva, Switzerland.
4.   Bosoaga A, Masek O &OakeyJ E: "CO_2 Capture Technologies for Cement Industry," *Energy Procedia*, Vol. 1, No. 1, 2009, pp. 133-140.
5.   Mehta P K: "Concrete Technology for Sustainable Development," *Concrete International*, Vol. 21, 19999, pp. 47-53.
6.   Schneider M et al.: "Sustainable cement production—present and future," *Cement and Concrete Research*, Vol. 41, No. 7, 2011, pp. 642-650.
7.   Justnes H: "How to Make Concrete More Sustainable," *Journal of Advanced Concrete Technology*, Vol. 13, No. 3, 2015, pp. 147-154.
8.   Damtoft J S et al.: "Sustainable development and climate change initiatives," *Cement and Concrete Research*, Vol. 38, No. 2, 2008, pp. 115-127.
9.   Gartner E: "Industrially interesting approaches to "low-CO_2" cements," *Cement and Concrete Research*, Vol. 34, No. 9, 2004, pp. 1489-1498.
10.   Danner T: "Reactivity of calcined clays," *Doctoral Thesis*, No. 218, Norwegian University of Science and Technology - NTNU, Trondheim, Norway, 2013.
11.   Fernandez R, Martirena F & Scrivener K L: "The origin of the pozzolanic activity of calcined clay minerals: A comparison between kaolinite, illite and montmorillonite," *Cement and Concrete Research*, Vol 41, No. 1, 2011, pp. 113-122.
12.   He C, Makovicky E & Osbaeck B: "Thermal stability and pozzolanic activity of calcined kaolin," *Applied Clay Science*, Vol. 9, No. 3, 1994, pp. 165-187.
13.   He C, Makovicky E & Osbaeck B: "Thermal treatment and pozzolanic activity of Na-and Ca-montmorillonite," *Applied Clay Science*, Vol. 10, No. 5, 1996, pp. 351-368.
14.   He C, Osbaeck B & Makovicky E: "Pozzolanic reactions of six principal clay minerals: activation, reactivity assessments and technological effects," *Cement and concrete research*, Vol 25, No. 8, 1995, pp. 1691-1702.
15.   Danner T, Østnor T, Justnes H:"Feasibility of Calcined Marl as an Alternative Pozzolanic Material," *Proceedings*, 1st International Conference on Calcined Clays for Sustainable Concrete. 2015. Lausanne, Switzerland.
16.   Danner T, Østnor T, and Justnes H: "Calcined Marl as a Pozzolan for Sustainable Development of the Cement and Concrete Industry," *Proceedings*, 12th International Conference on recent Advances in Concrete Technology and Sustainability Issues. 2012. Prague, Czech Republic.
17.   Danner T, Østnor T and Justnes H: "Thermally activated marl as a pozzolan for cementitious based products," *Proceedings*, Twin Covilha International Conference on Civil Engineering - Towards a better environment and The Concrete Future. 2013. Covilha, Portugal.
18.   Justnes H, Østnor T, and Danner T: "Calcined marl as effective pozzolana," *Proceedings*, International RILEM Conference on Advances in Construction Materials Through Science and Engineering. 2011, Hong Kong, China.
19.   Østnor T,Justnes H, and Danner T: "Reactivity and Microstructure of Calcined Marl as Supplementary Cementitious Material," in Calcined Clays for Sustainable Concrete. 2015, Springer. p. 237-244.
20.   Grønbech G L, Nielsen B N and Ibsen L B: "Comparison of plasticity index of Søvind marl found by use of Casagrande cup, fall cone apparatus and loss on ignition," Department of Civil Engineering, Aalborg University, *DCE Technical Reports*, Vol. 87, 2010, p. 14.
21.   Danner T, Norden G, Justnes H: "Characterisation of Calcined Raw Clays suitable as Supplementary Cementitious Materials", *Applied Clay Science*, Vol. 162, 2018, pp. 391-402.

22. Nielsen O B: "Lithostratigraphy and sedimentary petrography of the Paleocene and Eocene sediments from the Harre borehole", *Denmark Aarhus Geoscience*, Vol. 1, 1994, pp. 15-34.
23. Nielsen O B, Cremer M, Stein R, Thiebault F, Zimmermann H: "Analysis of sedimentary facies, clay mineralogy, and geochemistry of the paleogene sediments of site 647, Labrador sea, *Proceedings*, the Ocean Drilling Program, Scientific Results, Vol. 105, 1989, pp. 101-110.
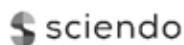
Meso Mechanical Study of Cracking Process in Concrete Subjected to Tensile Loading

Mathias Flansbjer
M.Sc., Ph.D., Adj. Prof., Researcher
RISE Research Institutes of Sweden, Mechanics Research
Box 857 SE-501 15 Borås, Sweden
E-mail: mathias.flansbjer@ri.se

Jan Erik Lindqvist
Ph.D., Senior researcher
RISE Research Institutes of Sweden, CBI
Ideon, SE-223 70 Lund, Sweden
E-mail: janerik.lindqvist@ri.se

ABSTRACT

This project focused on how the cracking process in concrete is influenced by both the micro and meso structures of concrete. The aim was to increase knowledge pertaining to the effect of critical parameters on the cracking process and how this is related to the material's macroscopic properties. A methodology based on the combination of different experimental methods and measuring techniques at different scales was developed. Crack propagation during tensile loading of small-scale specimens in a tensile stage was monitored by means of Digital Image Correlation (DIC) and Acoustic Emission (AE). After testing, crack patterns were studied using fluorescence microscopy.

Key words: Concrete, Cracking, Testing, Digital Image Correlation, Acoustic Emission, Microscopic Analysis

1.   INTRODUCTION

Many of the characteristics of concrete mechanical behaviour observed at the macro scale can be explained by the heterogeneous structure of concrete at the micro and meso scales. Conventional strength tests on the macroscopic scale are essentially intended to characterize and compare different qualities of concrete in a standardized way but give limited information at the micro and meso scales since they do not reflect the heterogeneous nature of the materials in a relevant way. Therefore, the combination of different experimental methods and measuring techniques at different scales is essential to enable deep investigation and understanding of the cracking process from micro to macro scale. Within this project, we focus on how the fracture process in concrete is influenced by the aggregate shape. The project includes the development of a methodology that enables detailed analysis at the micro and meso scales. The methodology is based on the combination of different experimental methods and measuring techniques on different scales, see Figure 1.
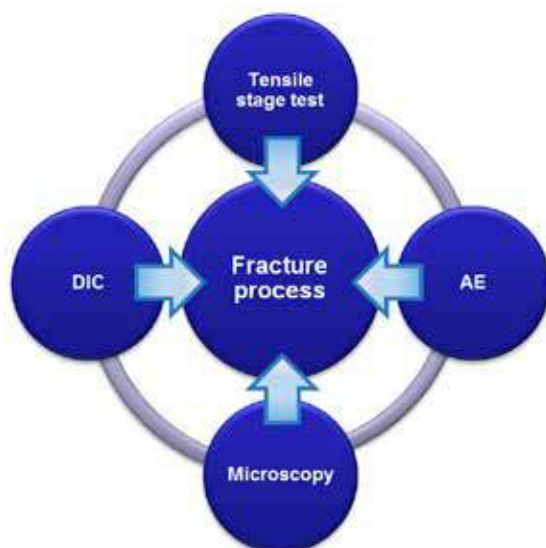
Figure 1 – Experimental methodology.

In the small-scale tests, concrete specimens were subjected to a direct tensile force in a tensile stage, while the fracture process was registered by Digital Image Correlation (DIC) and Acoustic Emission (AE). Both techniques have been used comprehensively to study the cracking process in concrete, but only a few papers have highlighted the potential to use them in combination, e.g. [1-3]. By using DIC it is possible to follow crack propagation in relation to the material structure on the surface of the specimen in a detailed way, whereas AE offers real-time measurement of the crack activity within the specimen. By combining these techniques, it is possible to relate the AE signal characteristics to different phases of the cracking process, such

as crack initiation, propagation and bridging of microcracks into macrocracks, as well as the creation and localization of the final fracture. The specimens were impregnated with epoxy containing fluorescent dye in their final state after testing. The cracks and final fractures were then microscopically examined, which allowed to link the cracking and fracturing processes to the textures and microstructures of the concrete. A similar methodology was presented in [4], based on the combination of DIC and examination of epoxy impregnated specimens in the study of fracture process of concrete in compression.

2. METHODS FOR FRACTURE CHARACTERIZATION

2.1 Digital Image Correlation

In recent years, there has been a substantial development of optical full-field deformation measurement systems based on Digital Image Correlation (DIC). Originally developed in the 1980s, this technique has been successfully applied to various mechanical and civil engineering structural problems [5]. This measurement technique is typically used to measure displacement fields and surface strain fields both in 2D and 3D. The basic idea behind DIC is to measure the displacement of the given specimen during testing by tracking the deformation of a naturally occurring or applied surface speckle pattern in a series of digital images acquired during loading. The analysis of the displacement of discrete pixel subsets of the speckle pattern within the images enables the acquisition of these data. As cracks are characterized by discontinuities in the displacement field, DIC measurements have proved suitable for the monitoring of crack formations in concrete at different scales, as previously shown by e.g. [4, 6-14]. It is possible to follow the propagation of all individual cracks at the surface long before they are visible to the naked eye, and subsequently quantify the crack width development locally for each crack with high accuracy until failure. By using the natural pattern of sawn specimen surfaces, cracking and crack growth can be monitored in detail in relation to the micro- and meso structures of the concrete.

In this study, the crack propagation was registered in a detailed way at different scales by 2D measurements at the surface of the specimens during testing by using the optical full-field deformation measurement system ARAMIS[TM] 4M by GOM.

2.2 Acoustic Emission

Acoustic Emission (AE) monitoring is a pertinent technique for monitoring fracture processes in concrete, both on material and structural levels, e.g. [3, 15-21]. The method is based on the small elastic stress waves produced by sudden movements in stressed materials caused by crack initiation and growth. A sudden movement at the source triggers the release of energy, in the form of stress waves, which radiate out into the structure and are recorded by sensors at the surface. The AE measurement system simply listens for the energy released by the object. This type of AE often has very small amplitudes and is in principle always of high frequency. Typical frequencies that are optimal for AE measurements can be within the range of 60–300 kHz. AE is therefore measured with highly sensitive piezoelectric resonant sensors in the ultrasonic range. The key element in an AE resonant sensor is the piezoelectric crystal that converts the movements into electrical voltage signals that are sent to a measuring computer for further signal processing. Various parameters are used to identify the nature of the AE source, including hits, events, counts, duration, amplitude, rise-time, energy and frequency.

AE monitoring offers real-time measurement of crack formation and is not limited to a single measuring point, as it is volumetric. AE monitoring can detect crack initiation and crack growth and provide information on when damage is accelerating. Furthermore, if an AE signal reaches several sensors and the speed of sound is known, the approximate location of the event can be determined.

In this study, a six-channel Micro-II Digital AE system by Physical Acoustics Corporation was used for measuring and analysing AE. The system basically consists of AE sensors, pre-amplifiers and a PC for data acquisition, signal processing and analysis.

2.3   Micro and meso scale analysis

The analyses of the tested samples were performed using fluorescence microscopy on thin sections impregnated with epoxy containing fluorescent dye. The analysed thin sections were cut parallel to the surface analysed using DIC. The size of the thin sections was approximately 70×50 mm^2 with their length axis oriented parallel to the main cracks. The measurements were performed using the KS400 image analysis program on images covering an area of 5.5×4.2 mm^2. Six to nine images were taken covering 33 to 50 mm of the length of the fracture zone. The fracture surfaces were classified as fractures in aggregate, paste and intertransitional zone (ITZ) adjacent to the aggregate. The classification was done manually while the quantitative measurements were made using image analysis. Each side of the fractures were analyzed separately.

The parameter used to describe aggregate particle shape was the minimum length divided by the maximum length (F_{min}/F_{max}) To reduce stereological artefacts, half of the objects with the lowest F_{max} was excluded from the measurement. This rule was used in order to be scale independent. Generally, these were objects with an F_{max} smaller than about 100 microns. Eighty percent of the remaining measured particles were in the size range 0.25 to 2 mm assessed according to [22]. In this measurement, objects with F_{min}/F_{max} larger than 0.6 as well as edge-objects were excluded. For further information the reader is referred to [23].

3.   MATERIAL DESCRIPTION

The test series presented in this work included two different concrete recipes, referred to as N038 and C038. The concretes had a w/c of about 0.38 and the coarse aggregate (8-16 mm) consisted of felsic rock material. The main difference between the mixes was related to the fine aggregate (< 8 mm), which were of Natural (N038) or Crushed (C038) felsic rock material. The compressive cube strengths at 28 days were determined to be 91.5 MPa and 80.9 MPa for N038 and C038, respectively. Furthermore, the tensile strength and fracture energy were determined by direct tensile tests on notched cube specimens according to recommendations given by RILEM [24] and [25]. A summary of the material properties is given in Table 1. The same materials, cast at the same time, were used in an earlier project concerning factors affecting the shear strength capacity based on an understanding of micro and meso scale material properties [10].

Table 1 – Material description.

Parameter	C038	N038
w/c	0.38	0.38
Fine aggregate 0-8 mm [kg/m^3]	1060	900
Coarse aggregate 8-16 mm [kg/m^3]	708	900
Water [kg/m^3]	164	162
Cement [kg/m^3]	429	426
Water reducer [kg/m^3]	1.1	0.7
Compressive cube strength [MPa]	80.9	91.5
Tensile strength [MPa]	5.0	5.2
Fracture energy [N/m]	209	176

The frequency distribution of the aggregate shapes for crushed and natural aggregate is shown in Figure 2. It can be observed from this figure that the crushed aggregate in the 0.25 to 4 mm fraction contains a significantly higher amount of elongated and flaky particles, i.e. low F_{min}/F_{max}, compared to the rounded natural aggregate particles. Quantitative microscopic analysis of the fine aggregate particles indicated a significant orientation in most of the analysed micro images. The orientation of the aggregate differs however between different micro images (2.8×2.1 mm^2) and there is no orientation that is consistent within the area of a thin section (70×50 mm^2). This pattern with orientation in the microscale but not in the mesoscale occurs in samples with both natural and crushed aggregate.
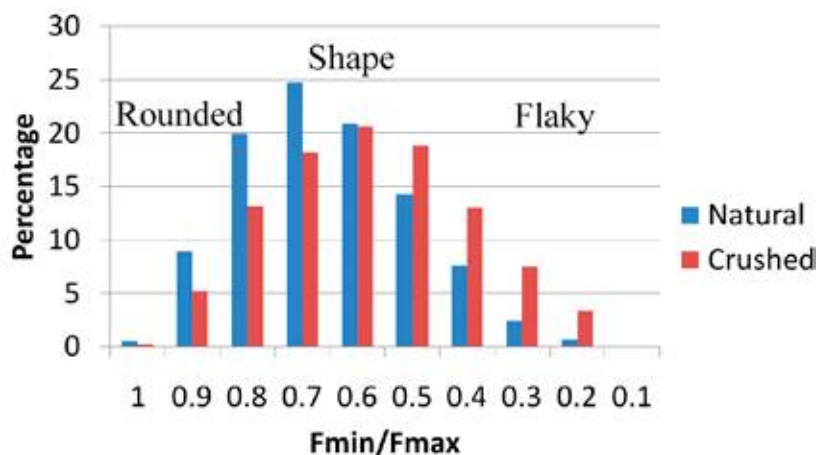

Figure 2 – Shape factor distribution for the natural and crushed fine aggregate used.

4. DIRECT TENSILE TESTS

4.1 Specimen preparation

Rectangular prisms with section dimensions of 60×60 mm^2 were cut from cast concrete blocks according to the illustration in Figure 3 (left). The top and bottom edges were face-ground to the

final length to achieve plane parallel surfaces. Along the two sides, a 10 mm deep and 5 mm wide notch was cut with a stationary diamond cutting blade. Finally, the prisms were cut into the test specimens with geometry as shown in Figure 3 (right). Specimens with two different thicknesses t were manufactured, i.e. 10 and 20 mm. The specimens with Natural and Crushed fine aggregates are referred to as N038-# and C038-#, respectively.
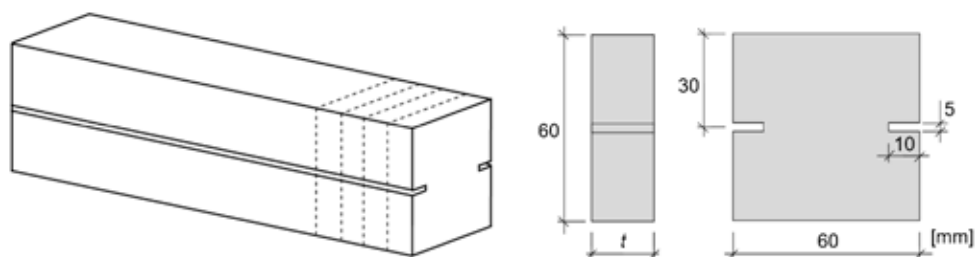
Figure 3 – Specimen preparation and geometry.

To make the meso structure of the concrete more prominent in the DIC images, the surface of the specimens was polished in several steps (Table 2) in a grinding machine before testing.

Table 2 – Surface preparation in Abramin grinding machine from Struers.

Step	SiC Paper	Lubricant	Force [N]	Speed [rpm]	Time [min]
1	220	water	200	300	3-5
2	500	water	200	300	3
3	1000	water	200	300	3
4 [1)]	4000	water	200	300	5

1)   This step was only performed when microscope objective was used during testing.

The specimen was glued to the two loading platens of the machine, see Figure 4. Thereby, any small deviations from parallelism between the specimen end surfaces and the loading platens were accommodated by the adhesive layer yielding a perfect fit between the specimen and the loading platens. The specimen was glued to the upper loading platen using a fixture to ensure that the centre lines of the platen and the specimen coincided and to ensure that the face of the loading platen and the centre axis of the specimen were positioned perpendicularly. The upper loading platen, together with the glued-on specimen, was then bolted to the machine. Finally, the lower loading plate, which was already attached to the machine, was glued to the bottom of the specimen. The maximum difference in adhesive thickness over the area was approximately 0.1 mm. The adhesive used was X60 by HBM. Before gluing, the contact surfaces of the specimen and loading platens were cleaned with abrasive paper and acetone to ensure good adhesion. The adhesive could set for at least 30 minutes before testing.
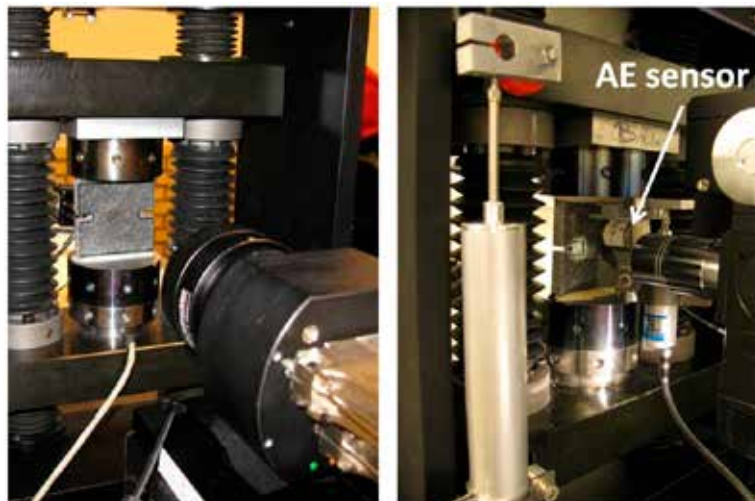
Figure 4 – Photo of tensile stage test setup with camera configuration at meso scale (left) and at micro scale (right).

4.2   Test setup and performance

The direct tensile test setup consisted of different subsystems as illustrated in Figure 5; the tensile stage with control system, data acquisition system, AE system and DIC system.
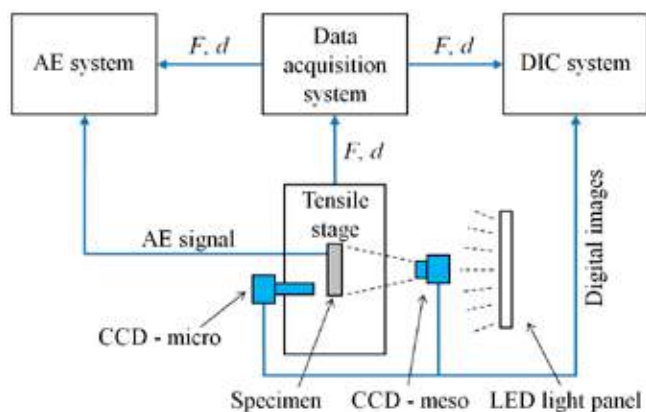
Figure 5 – Illustration of the tensile stage test system.

The tensile stage can be considered as a small mechanical testing machine. Two cross beams are connected to each other by two high-precision right- and left-handed roller screws. When the screws rotate, the two cross beams move away from/toward each other symmetrically relative to the centre line. As such, the centre of the specimen remains in the centre of the digital image during the entire test. The screws are rotated by an ABB brushless servomotor. The force F was recorded by a load cell with a maximum capacity of 10 kN and the relative displacement d between the two cross beams was measured with a LVDT with a measuring range of ±5.0 mm.

Furthermore, the displacement was measured locally over the two notches by Crack Opening Displacement (COD) transducers, COD_1 and COD_2, with a gauge point distance of approximately 5 mm. The steel brackets used to hold the two COD transducers in position were mounted on each side of the notches with a fast-curing adhesive. The COD transducers had a measuring range of 4.0 mm and a relative error of less than 1 %. In these tests, the loading was controlled at a displacement rate of 0.06 mm/min. Photos of the test set-up are shown in Figure 4.

The setup enables 2D DIC measurements on two different scales: one meso scale covering the entire specimen surface (65×65 mm^2) and one micro scale focusing on one of the notches covering an area of 8×8 mm^2, see Figure 6. At the meso scale, the sub-set size was 20×20 pixels and the overlap was three pixels, and at the micro scale, the sub-set size was 50×50 pixels and the overlap was 20 pixels. The system setup employed resulted in a spatial resolution of approximately 0.63×0.63 mm and 0.19×0.19 mm, and a coordinate measurement accuracy of approximately 1.3 µm and 0.16 µm, for the meso and the micro scales, respectively. To obtain high contrast levels, the specimen was illuminated by a white LED light panel at the meso scale. The images were captured with a frequency of 5 Hz. The AE activity was recorded by one AE sensor with a resonance frequency of 150 kHz, see Figure 5 (right). A pre-amplification of 40 dB and a threshold level of 40 dB were used. The hit detection parameters were set to: PDT = 100 µs, HDT = 200 µs and HLT = 200 µs. The force and the displacement were also recorded in the DIC and the AE systems.
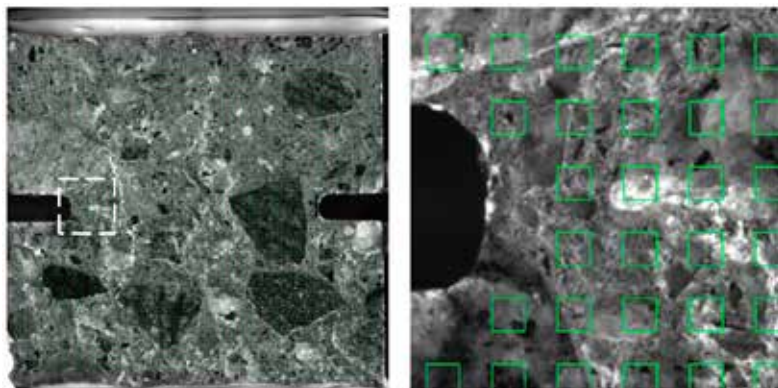
Figure 6 – DIC image with sub-sets at meso scale (left) and at micro scale (right). The image size is 65×65 mm^2 and 8×8 mm^2, respectively.

5. EXPERIMENTAL RESULTS

The tensile behaviour of the concrete was evaluated from small-scale direct tensile tests, as described in Section 4.1. For each material three specimens had a thickness of approximately 20 mm and six specimens had a thickness of approximately 10 mm. The performed tests are summarized in Table 3 and the tensile stress-displacement relationships are shown in Figure 7. The displacement is represented as the mean value of the two COD transducers. The ligament area is the measured section of the location of the notch. The maximum tensile stress along with the corresponding crack opening displacement are summarized in Table 3.

Table 3 – Summary of the small-scale direct tensile tests.

Specimen	Thickness [mm]	Ligament area [mm²]	DIC scale	Max. tensile stress [MPa]	COD at max tensile stress [μm]
N038-1	20.2	8.2	Meso	4.5	13
N038-2	20.5	7.9	Meso	4.5	11
N038-3	19.7	7.9	Meso	5.2	11
N038-4	10.2	4.3	Meso	4.8	9
N038-5	10.2	4.3	Meso	4.2	13
N038-6	9.9	4.2	Meso	5.7	11
N038-7	9.9	4.2	Micro	5.1	14
N038-8	9.9	4.1	Micro	6.3	13
N038-9	10.1	4.2	Micro	6.1	9
C038-1	20.7	8.5	Meso	5.7	-
C038-2	20.5	8.4	Meso	4.6	11
C038-3	20.6	8.5	Meso	4.9	12
C038-4	10.1	4.1	Meso	4.7	12
C038-5	10.0	4.0	Meso	4.7	11
C038-6	10.1	4.0	Meso	5.2	11
C038-7	10.1	4.0	Micro	5.3	5
C038-8	10.0	4.0	Micro	4.2	8
C038-9	10.2	4.1	Micro	5.6	10

In general, no major differences were found in stress-displacement relationships or crack formation during testing between the specimens with a thickness of 20 mm and those with a thickness of 10 mm. The more detailed analyses by DIC, AE and microscopy were therefore limited to the thinner specimens, N038-4 to N038-9 and C038-4 to C038-9.

Figure 7 – Tensile stress vs. displacement from direct tensile tests on notched small-scale concrete specimens.

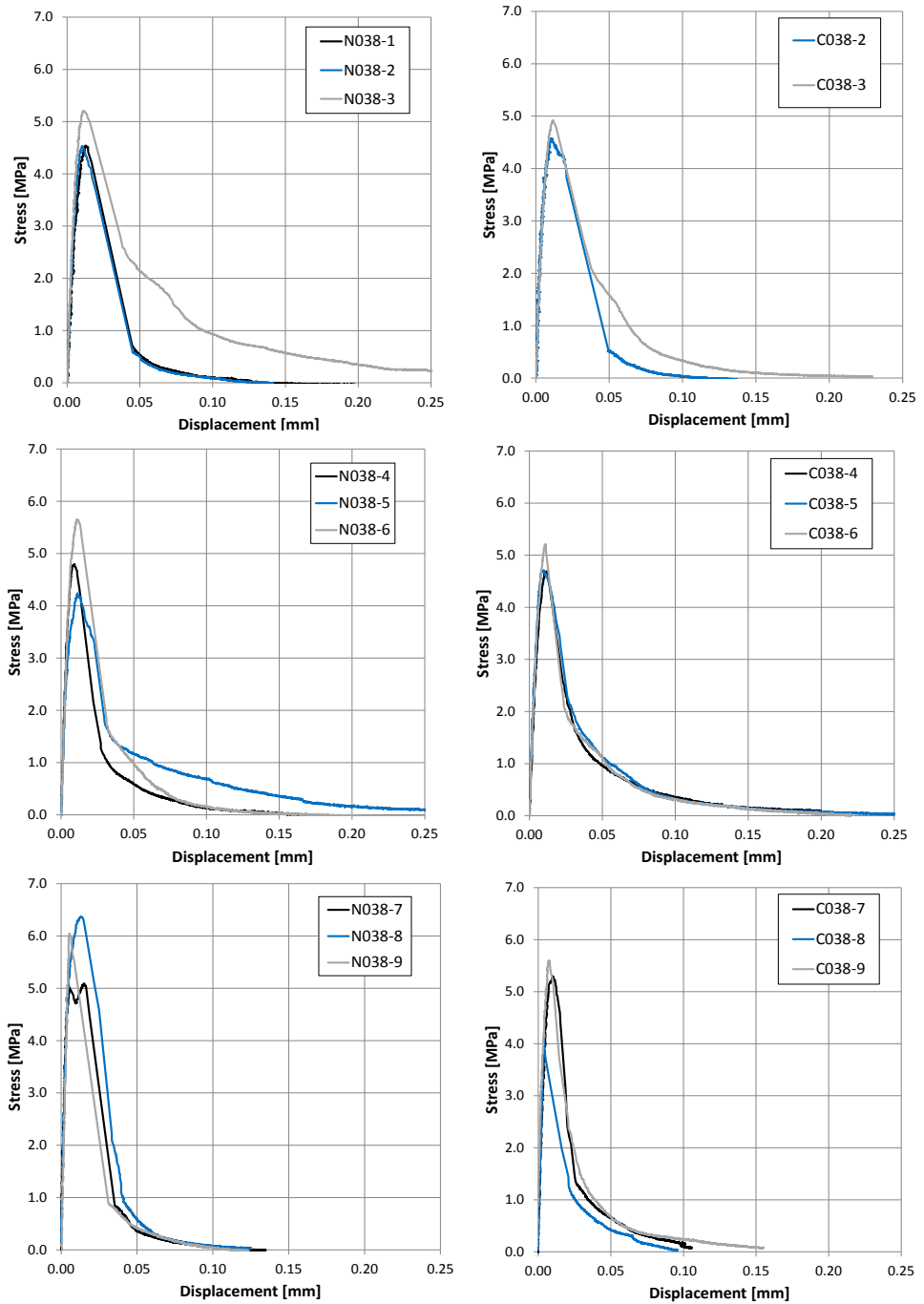Instead of using the COD transducers to measure the deformation over the notched area, it is also possible to use "virtual" extensometers in the DIC measurements. For C038-5 a comparison between the results obtained by the transducers and the "virtual" extensometers (C038-5 DIC) is shown in Figure 8. The displacement determined by DIC was calculated as the mean value of two virtual extensometers (COD1 and COD2), see Figure 9. Initially, the correspondence between the displacements evaluated from the COD transducers and from DIC measurements is reasonable. Results start to differ close to peak stress and during the descending branch; displacements evaluated from the DIC give smaller values compared to the COD transducers. This applies to all compared specimens and is related to the fact that the displacement is measured closer to the bottom of the notch by DIC. Hence, the deformation over the notched area can be evaluated from the DIC measurements, which would considerably simplify the test method as the COD transducers can be excluded.
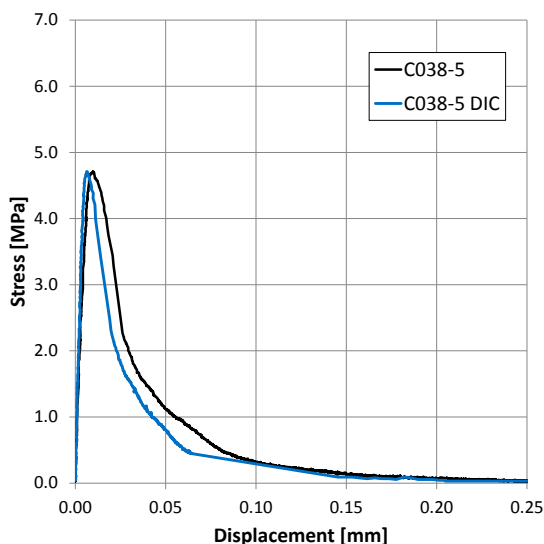
Figure 8 – Comparison of tensile stress vs. displacement measured by COD transducers and by virtual extensometers in DIC.

The methodology allows the cracking process to be monitored by DIC in relation to the texture of the concrete, both on the meso and micro scales. The small discontinuities related to crack formations can be clearly visualized by overlaying major strain fields at the surface of the specimen. Figure 9 (right) presents the crack formation obtained by DIC at different phases of the loading for specimen C038-5. In general, the quality of DIC measurements is strongly influenced by the speckle pattern used; hence, the use of natural speckle pattern may cause some limitations. The texture of the polished concrete in this study was relatively suitable but included some larger areas with minor differences in greyscale; thus, leading to deteriorated results in these areas. To some extent this could be amended by using larger subsets, although it would also reduce the spatial resolution. Hence, the size and step size of the subsets were chosen based on the material texture used as pattern and the desired resolution and accuracy.

In this study, the analysis of the AE signals was limited to hits, which gives an indication of crack initiation and crack intensity. In the hits-displacement relationship presented for specimen

C038-5 in Figure 9 (left) one can see that the AE activity, represented as cumulative number of hits, was relatively small during the pre-peak part compared to during the post-peak part. Also, the amplitude of the hits differs between the two parts, with an average value of approximately 45 dB in the pre-peak part and approximately 50 dB in the post-peak part. These observations were general for all specimens. It should be kept in mind that the obtained AE results depend on various parameters, such as AE sensor, pre-amplification and hit detection, type of AE source, test set-up, specimen size, etc. Consequently, these conditions should be kept as similar as possible in order to make quantitative comparisons of the crack activity between different tests. Otherwise, the AE results can simply be used for qualitative comparisons of the activity.
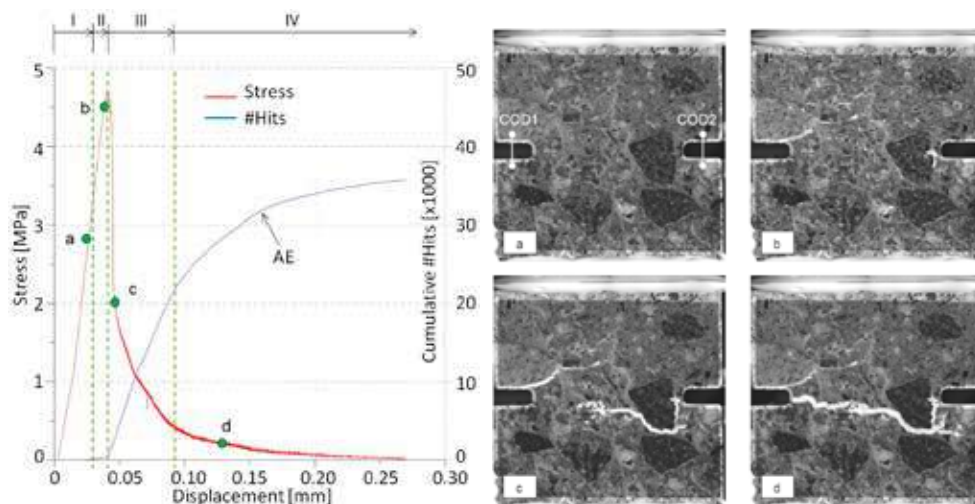
Figure 9 – Stress and cumulative AE Hits versus displacement (left) and example of crack formations in the different phases of the cracking process (right) for specimen C038-5. The image size is $65{\times}65\ mm^2$.

The cracking process observed by DIC and AE during the tests may to some extent be related to different phases in the stress-displacement relationship. These findings correspond well with the four stages in the tensile fracture process defined in [26]; (I) elastic stage, (II) micro cracking, (III) macro cracking and (IV) bridging.

The cracking process is exemplified for one specimen (C038-5) in Figure 9 (right). Within the initial elastic pre-peak part (I) of the stress-displacement curve, the number of AE hits is small which is thought to be related to the opening of existing micro-cracks in both the cement matrix and the aggregate particles. These cracks are, however, difficult to identify by DIC but can be observed as successively appearing scattered deformations. When new cracks start to develop in phase II, mainly in the ITZ of the larger aggregate particles, the number of hits also starts to increase. The number of hits further increases when cracks start to propagate into the cement paste matrix from the ITZ or from the two notches. In the proximity of the peak stress, the crack intensity and resulting AE activity increase. These observations correspond well with the initiation of the non-linear behaviour, represented by an increasing curvature in the stress-displacement curve, which occurs just before peak stress is reached upon the merging of different micro-cracks. According to [26] this energy release in the pre-peak regime can be interpreted as the deviation from the "ideal" linear-elastic behaviour. During the post-peak

24

regime, the AE activity can be related to the energy needed to create the final fracture. The hit-rate reaches the highest value during the initial part of the post-peak behaviour related to the creation of one localized macro-crack in phase III. During the last phase (IV) of the post-peak behaviour related to gradual opening of the macro-crack, the AE activity is mainly caused by the bridging effect of the aggregate particles. While the crack opens, the hit rate decreases, and eventually becomes zero as the crack is completely open. The transitions between the different phases are, however, generally ambiguous and the phases are found to overlap.

Due to the scalable nature of DIC measurements, the cracks can be studied both with higher spatial resolution and higher displacement accuracy at the micro scale compared to the meso scale. Figure 10 presents the crack formations close to one of the notches at around maximum stress for C038-7 and N038-7, respectively. As can be observed, the cracks are mostly located in the ITZ and the cement matrix, but in some cases propagate through aggregate particles. A further development of surface preparation and lighting techniques would allow an improved spatial resolution of the cracks. Since the specimens had two notches, it was not possible to predict at which notch the main crack would be initiated and accordingly where to place the microscope.
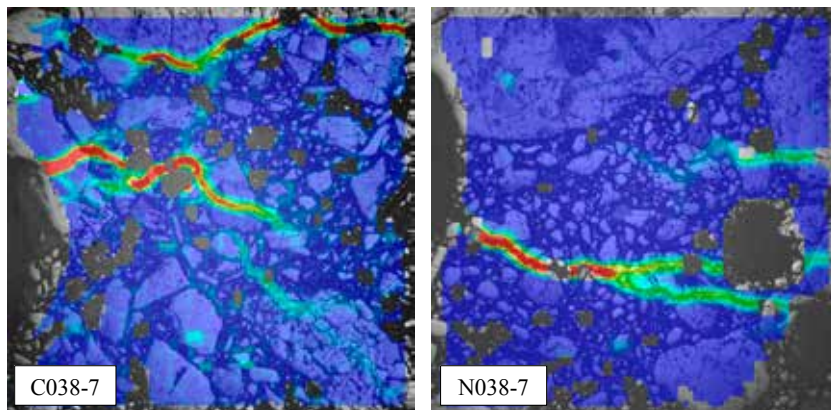
C038-7

N038-7

Figure 10 – Example of crack formations in C038-7 and N038-7, obtained by a microscopic lens. The notch can be seen to the left in both figures. The image size is 8×8 mm^2.

6.   MICROSCOPIC ANALYSIS

After testing, the specimens were analysed using a thin section technique in fluorescence microscopy combined with image analysis. The thin sections covered the entire fracture area from notch to notch, see Figure 11. The combination of DIC measurements during testing and fluorescence microscopy after testing makes it possible to characterize and quantify the fracture down to a micrometre scale and relate it to the cracking process during loading.
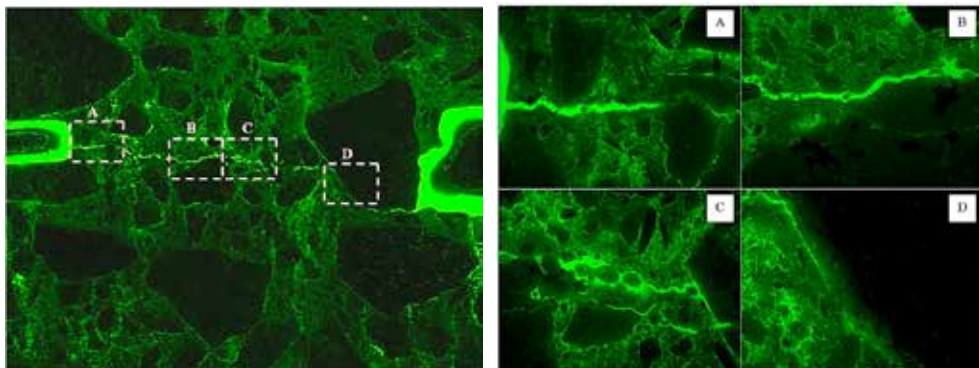
Figure 11 – Fluorescence image of C038-5 after testing, at meso (left) and micro scale (right).
The meso scale image covers 50x40 mm^2 and the micro scale images cover 5.5x4.2 mm^2.

The fluorescence image shown in Figure 11 covers the area seen in the DIC images presented in Figure 9 (right). The approximate positions of the individual sub-images are indicated in Figure 11 (left). Sub-image (A) shows the area adjacent to the left notch. Sub-image (C) shows an area where the main fracture temporarily stopped during the test as can be seen in the DIC image (c) in Figure 9 (right). It can be observed that the microstructure is considerably damaged by the fracturing process in this region. Sub-image (D) shows the main fracture that was forced to go around the larger aggregate close to the right notch. It can be noted that the crack running diagonally from the left notch along the ITZ in Figure 9 (b) to (d) has to a large extent closed after the test, as can be seen in Figure 11 (left).

As described earlier, the fracture surfaces were classified as fractures in aggregate, in paste and in the ITZ. Figure 12 shows an example of this fracture classification for samples C038-8 and N038-6. The results from the measurements of total fracture length are given as percentages in Table 4, showing that the aggregate shape has no significant influence on the fracture propagation in tensile stage test. The fracture length distributions in paste, aggregate and ITZ are given in Table 5 and Figure 12.

Figure 12 – Interpretation of fracture classification for sample a) C038-8 and b) N038-6. White
line fracture in paste, red line adhesion and blue fracture in aggregate. The notch is
seen to the right. The image covers 5.5x4.2 mm^2.

Table 4 – Quantitative results in % on crack propagation in the tensile stage tests.

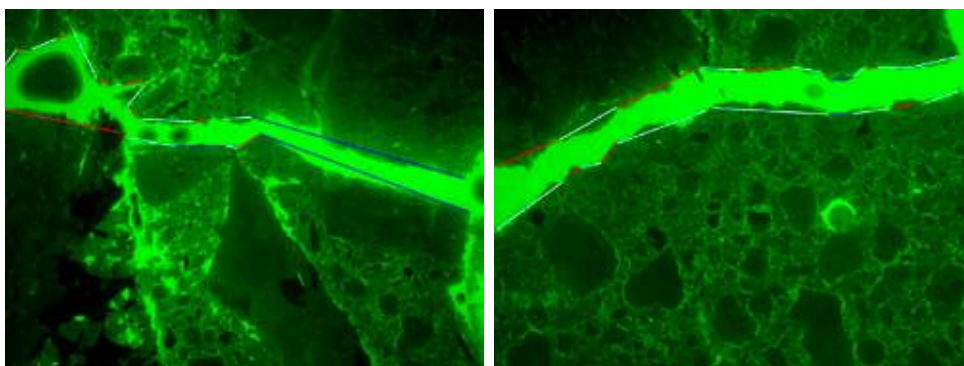|	C038-5	C038-6	C038-8	N038-5	N038-6	N038-7	C038	N038
Aggregate	10	18	36	8	24	33	21	22
Paste	55	45	40	52	50	49	47	50
ITZ	35	37	24	40	26	18	32	28
Total	100	100	100	100	100	100	100	100

Table 5 – Fracture length distribution in aggregate (A), paste (P) and ITZ (T) as seen in Figure 12. Values given as percentages based on number of cracks in each size class.

Size [mm]	C038A	C038P	C038T	N038A	N038P	N038T
0.125	5	13	35	5	13	39
0.25	12	16	33	10	22	36
0.5	36	30	15	36	22	16
1	25	24	6	11	26	6
2	7	13	8	24	11	2
5	15	4	3	14	6	1
Total	100	100	100	100	100	100

A comparison with results obtained from tests in shear in a previous study using the same concrete [9] shows that the fracture process in shear is dependent on the shape of the aggregate particles which is not the case in tension as shown in this investigation. There are, however, differences in detail of the fracture pattern between samples with rounded natural aggregate and those with elongated crushed aggregate, also in tension. The analysis of fractures in tension shows that there are more secondary fractures branching out from the primary fracture in samples with crushed aggregate. Branching may form when a propagating crack reaches a void in the structure and several cracks are initiated on the opposite side of the void. Branching may also occur when a secondary crack propagates along the ITZ of an aggregate particle oriented oblique to the direction of propagation. The main crack continues in the cement paste along the main direction of propagation. If the propagating crack passes through or around an aggregate particle depends partly on its size and orientation as well as the presence of internal weaknesses in the particle. The influence of size can be seen in Table 5 where the cracks in the ITZ are mainly short while cracks through the aggregate particles are longer. Propagating secondary cracks often stop or are deflected at aggregate particles. It is suggested that this is more frequent in the samples with crushed aggregate. As the secondary fractures have partly grown in shear, flaky particles may act through interlocking. Aggregates deform in a more brittle manner compared to the cement paste and, as such, a more brittle fracture behaviour is expected if more of the crack propagation occurs in aggregates. This can be observed in the post peak behaviour of the samples N38-5 and C38-5 compared to N38-7 and C38-8, see Figure 7 and Table 4. The differences in meso and micro scales provide potential explanations for the observed differences in the mechanical behaviour. Accordingly, this research area is suitable for continued research.

7.   CONCLUDING REMARKS

The development of a methodology, based on the combination of different experimental methods and measuring techniques on different levels of scales is presented. During direct tensile tests on small scale concrete specimens, the cracking process was registered by means of

DIC and AE. By combining DIC and AE, it was possible to visualize crack propagation and identify different phases of the cracking process both in the pre-peak and post-peak regimes, from micro-crack initiation to completion of the final fracture. Furthermore, the DIC measurements allow to locate cracks and also to quantify the crack opening displacement and the crack length by analysing discontinuities in the displacement field. Furthermore, this study indicates a strong correlation between the AE activity and the level of mechanical damage in the material, related to the crack formation.

After the direct tensile test, the cracks and final fractures were studied in detail using fluorescence microscopy, linking the cracking and fracturing process to the material structure of the concrete. The applied combination of methods provides detailed information of the cracking process. Hence, the present project shows that the applied combination of methods has a potential for increasing the understanding of cracking process on micro and meso scale and how it relates to the loading. This makes it a useful approach for the study of new cement based materials.

According to the analysis, there are no major differences in the fracture behaviour in tension between concrete with crushed compared to natural sand in the aggregate finer than 8 mm. This observation differs from the behaviour in shear wherein the shape of the aggregate had a distinct influence.

REFERENCES

1. Rouchier S, Foray G, Godin N, Woloszyn M and Roux J-J: Damage monitoring in fibre reinforced mortar by combined digital image correlation and acoustic emission. *Construction and Building Materials*, Vol. 38, 2013, pp. 371-380.
2. Alam S Y, Saliba J and Loukili A: Fracture examination in concrete through combined digital image correlation and acoustic emission techniques. *Construction and Building Materials*, Vol. 69, 2014, pp. 232-242.
3. Guo M, Alam S Y, Bendimerad A Z, Grondin F, Rozière E and Loukili A: Fracture process zone characteristics and identification of the micro-fracture phases in recycled concrete. *Engineering Fracture Mechanics*, Vol. 181, 2017, pp. 101-115.
4. Caduff D and van Mier J G M: Analysis of compressive fracture of three different concretes by means of 3D-digital image correlation and vacuum impregnation. *Cement and Concrete Composites*, Vol. 34, No. 4, 2010, pp. 281-290.
5. Sutton M A, Orteu J J and Schreier H W: *Image correlation for shape, motion and deformation measurements*. 2009, Springer, New York.
6. Destrebecq J F, Toussaint E and Ferrier E: Analysis of cracks and deformations in a full scale reinforced concrete beam using a digital image correlation technique. *Experimental Mechanics*, Vol. 51, No. 6, 2010, pp. 879–890.
7. Skoček J and Stang H: Application of optical deformation analysis system on wedge splitting test and its inverse analysis. *Materials and Structures*, Vol. 43, 2010, pp. 63–72.
8. Shah S P and Chandra Kishen J M: Fracture properties of concrete-concrete interfaces using digital image correlation. *Experimental Mechanics,* Vol. 51, No. 3, pp. 303–313.
9. Flansbjer M, Lindqvist J E and Silfwerbrand J: Quantitative fracture characteristics in shear load. *Proceedings*, *fib* Symposium, Prague, Czech Republic, 8-10 June 2011, pp. 567-570.
10. Jacobsen J S, Poulsen P N and Olesen J F: Characterization of mixed mode crack opening in concrete. *Materials and Structures*, Vol. 45, 2012, pp. 107-122.

11. Skarżyński L, Kozicki J and Tejchman J: Application of DIC technique to concrete – Study on objectivity of measured surface displacements. *Experimental Mechanics,* Vil. 53, 2013, pp. 1545–1559.
12. Gencturk B, Hossain K, Kapadia A, Labib E and Mo Y-L: Use of digital image correlation technique in full-scale testing of prestressed concrete structures. *Measurement*, Vol. 47, 2014, pp. 505–515.
13. De Wilder K, Lava P, Debruyne D, Wang Y, De Roeck G and Vandewalle J: Experimental investigation on the shear capacity of pre-stressed concrete beams using digital image correlation. *Engineering Structures*, Vol. 82, 2015, pp. 82–92.
14. Hamrat M, Boulekbache B, Chemrouk M and Amziane S: Flexural cracking behavior of normal strength, high strength and high strength fiber concrete beams, using Digital Image Correlation technique. *Construction and Building Materials*, Vol. 106, 2016, pp. 678–692.
15. Grosse C U and Ohtsu M: *Acoustic Emission Testing*, Springer-Verlag, Berlin, Heidelberg, 2008.
16. Ohno K and Ohtsu M: Crack classification in concrete based on acoustic emission. *Construction and Building Materials*, Vol. 34, 2010, pp. 2339-2346.
17. Fricker S and Vogel T: Site installation and testing of continuous acoustic monitoring. *Construction and Building Materials*, Vol. 21, 2007, pp. 501-510.
18. Kencanawati N N, Iizasa S and Shigeishi M: Fracture process and reliability of concrete made from high grade recycled aggregate using acoustic emission technique under compression. *Materials and Structures*, Vol. 46, 2013, pp. 1441-1448.
19. Soulioti D, Barkoula N M, Paipetis A, Matikas T E, Shiotani T and Aggelis D G: Acoustic emission behavior of steel fibre reinforced concrete under bending. *Construction and Building Materials*, Vol. 23, 2009, pp. 3532-3536.
20. Muralidhara S, Raghu Prasad B K, Hamid Eskandari and Karihaloo B L: Fracture process zone size and true fracture energy of concrete using acoustic emission. *Construction and Building Materials*, Vol. 24, 2010, pp. 479-486.
21. Saliba J, Loukili A, Grondin F and Regoin J P: Identification of damage mechanisms in concrete under high level creep by the acoustic emission technique. *Materials and Structures*, Vol. 47, 2014, pp. 1041-1053.
22. NT BUILD 486: *Aggregates: Size distribution*. Approved 1998-11, NT BUILD.
23. Lindqvist J E and Johansson S: Aggregate shape and orientation in historic mortars. *Proceedings,* 11th Euroseminar Applied to Building Materials, Ed I Fernandes, 2007.
24. RILEM TC 187-SOC: *Experimental determination of the stress-crack opening curve for concrete in tension: Final report*, May 2007.
25. RILEM TC 162-TDF: Test and design methods for steel fibre reinforced concrete: Uni-axial tension test for steel fibre reinforced concrete. *Materials and Structures*, Vol. 34, 2001, pp. 3-6.
26. van Mier J G M: *Concrete Fracture, a Multiscale Approach*, CRC Press, 2012.
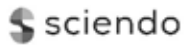
sciendo

Alkali-silica Reaction in Finnish Concrete Structures

Jukka Lahdensivu, DSc.
Managing Consultant at Ramboll Finland Oy
Pakkahuoneenaukio 2, 33100 Tampere, Finland
jukka.lahdensivu@ramboll.fi

Pirkko Kekäläinen, MSc.
PhD Student at Tampere University of Technology
Korkeakoulunkatu 5, 33720 Tampere, Finland
pirkko.kekalainen@student.tut.fi

Alina Lahdensivu
Student at Tampereen Klassillinen Lukio
Tuomiokirkonkatu 5, 33100 Tampere, Finland
alina.lahdensivu@gmail.com

ABSTRACT

Even though natural phenomena do not abide to borders, Finland has traditionally been considered an alkali-silica reaction (ASR) free country. This is due to exceptional quality of the mostly course crystalline igneous rocks. However, during the last few years dozens of cases of ASR have been reported. The scope of this study was to study the occurrence of ASR, and to find out the initiation time of the reaction in resent investigations of Finnish concrete structures. ASR is found occurring all over Finland. The reacting aggregates consist of rock types, which are considered relatively stable or low reacting in literature.

1.   INTRODUCTION

In Central Europe and Scandinavia, alkali-aggregate reaction typically occurs in massive concrete structures such as bridges and dams, as well as in concrete roads and parking buildings. Despite the similarities between the bedrock of Sweden and Finland, unlike Sweden, Finland has been considered an alkali-silica reaction (ASR) free country, due to the exceptional quality of its rock [1]. More than half of the bedrock in Finland consist of granitoids, usually considered non-reactive or low reactive. However, the first published case of ASR was reported already in 1994 [2] and dozens of cases have been reported during the last few years [3, 4, 5]. VTT Research Centre made an initial survey of the occurrence of alkali-aggregate reaction in Finland. They gathered 56 cases reported during the years 1996-2011, these were mostly bridges and houses [3]. After the initial survey, 27 new cases out of 97 bridges have been reported [5].

The reacting rocks in Finland are not unlike the Swedish reacting rocks, reported for example by Appelquist et al in 2013 in their article Alkali-silica-reactivity of Swedish aggregates used for concrete [6]. Among others, some of the rocks from the Schist Belts of Southern Finland and Tampere region, which have caused ASR problems in Finland, are very much alike gneissic or fine grained, schistose rocks mentioned by Appelquist et al as being alkali-silica reactive. From what Appelquist has later presented, for example in the 2017 Euroseminar for Mineralogy of Building Materials [7], it looks like some of these rocks derive from the Svecocarelian (or Svecofennian, as it is often called in Finland) orogeny, just like many of the rocks in Finland associated with ASR. Hence the differences between the the neighbouring countries may be more in the nomenclature than in actual composition or petrogenesis of the reacting rocks. Therefore, it should be just to compare the two countries.

The scope of this study was to survey the occurrence and find out the initiation time and the progress of alkali-silica reaction in resent cases in Finnish concrete structures.

2.   **ABOUT ALKALI-SILICA REACTION**

In alkali-aggregate reaction (AAR) the alkalinity of hydrated cement causes expansion of the aggregate in the concrete [8, 9, 10]. AAR has been traditionally divided into three different groups based on the reaction mechanism [11], but the division and even existence of some of the mechanisms has since been much debated and only alkali-silica reaction (ASR) has been deemed causing concrete expansion [12, 13, 14]. The ASR is the most common form of AAR [15]. In order for the ASR to take place, the reaction requires reactive silica-containing aggregate, a sufficient amount of alkali ions, calcium hydroxide and a minimum of 80% of relative humidity of concrete [10, 16]. Relative humidity of the concrete and expansion of ASR gel over time has been studied by Poole [17]. According to his studies, expansion of ASR gel starts to grow slowly as early as RH 50%. After RH 80% expansion will start to grow rapidly, see fig. 1. The environmental factors influencing ASR in Finland have been explained by Holt and Ferreira [18].
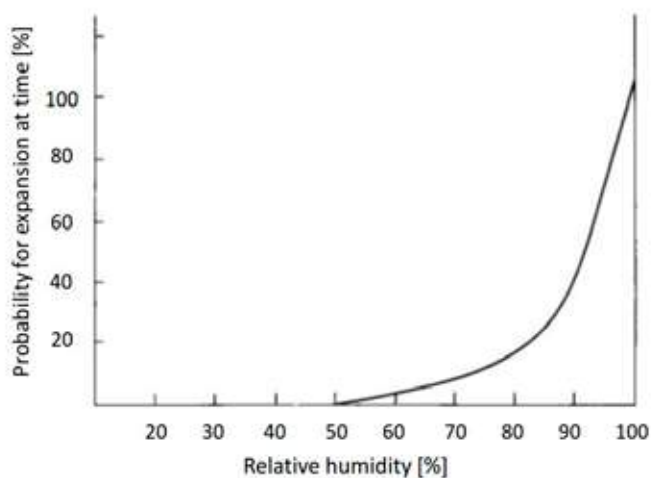
Figure 1 – The effect of relative humidity of concrete to the expansion rate of ASR [17].

ASR is a heterogeneous chemical reaction, which takes place in the aggregate particles between the alkaline pore solution of the cement paste and reactive silica in the aggregate [10]. The pore water must contain sodium ($NaOH$) and potassium (KOH) hydroxides and the aggregate must contain minerals with low resistance to alkalinity [15]. The reaction forms alkali-silica gel, which has the property of absorbing lots of water from the surroundings, causing the volume of the gel to grow, which leads to internal pressure of aggregate and finally also in the pore system of concrete. When the internal pressure exceeds the tensile strength of concrete, cracks appear in the concrete structure allowing the relatively soft gel to extrude through them [15, 19], see fig. 2. Far advanced ASR can be detected by naked eye from cross section of concrete sample, see fig. 3.
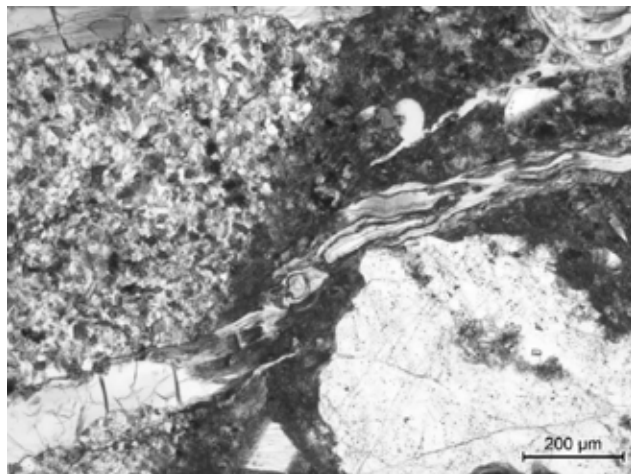
Figure 2 – Alkali-silica gel filling a crack propagating from the reacting aggregate the crack in concrete.
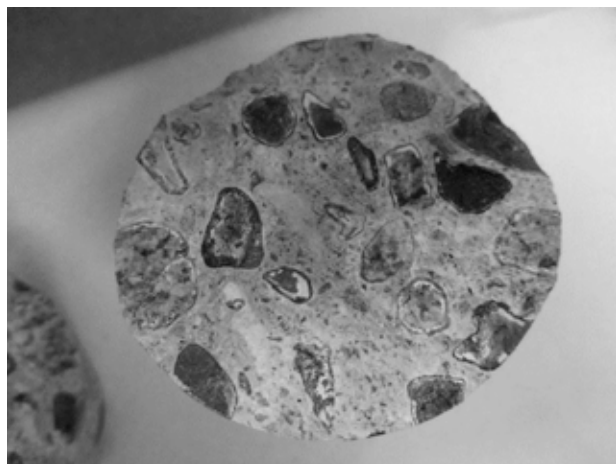
Figure 3 – Far advanced ASR can be seen as a dark reaction rim on the margin of the aggregate particles.

ASR generally results in slow degradation of concrete. The deterioration rate is influenced by prevailing conditions (i.e. temperature and humidity) as well as the type of aggregate and cement. In the case of silica bearing rocks, ASR may develop as soon as in 2-5 years. All aggregate containing silica, may potentially be reactive. However, differences in the crystal structure, density and grain size affect the reactivity. Different classifications for the reactivity of minerals and aggregates have been suggested by various authors over the years. Reactive aggregate types from all over the Europe have been listed among other by the RILEM technical committee [20]. AAR has been reported to occur also with highly stable rocks such as granite,

quartzite and sandstone [19]. The most commonly suggested reacting aggregates, when it has been identified, in the previously reported cases in Finland, are schists, quartzites, gneisses, and granites [6, 7, 8]. With blended cements containing substitute cementitious materials like blast furnace slag (BFS) and pulverized fly ash (PFA), AAR is less common since fewer reacting alkalis are generally involved than with Portland cement (OPC) [22, 23, 24, 25, 26, 27, 28]. With small amounts of reactive silica, the expansion caused by the ASR is high. After 20% of silica content the expansion is lower, see fig. 4. This means, that varying the silica content in concrete, it is possible to lower the risk of ASR in new concrete construction [15]. Obviously, in existing concrete structures studied in this paper, content of concrete is what it is.
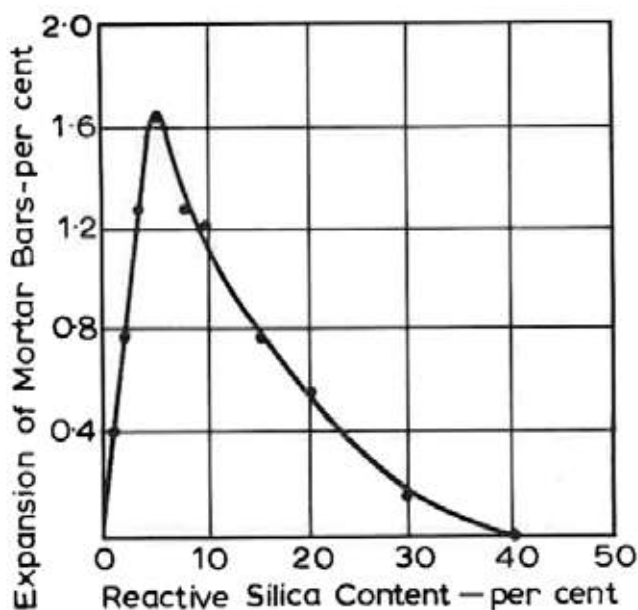
Figure 4 – Dependence of the expansion reaction in function of the silica content [15].

A concrete structure suffering from ASR typically shows discolouration due to surface moisture, irregular pattern cracking, swelling and oozing of a gel-like reaction product from the cracks [15]. The visible damage from ASR resembles the cracking caused by frost attack and often coincides with it [29]. The most significant difference between ASR and freeze-thaw damage is the pattern of cracking, which in the case of freeze-thaw damage is most intensive close to the outer surface and loses intensiveness with depth. ASR cracking begins deeper inside the concrete and produces a more regular cracking pattern across the entire concrete structure [30].

The state of the art method in, identifying ASR in a laboratory, is optical microscopy [31, 32, 33]. In some of the cases, recognizing mineral phases or reaction products with a SEM-EDX may be needed. The standard practice, most commonly followed in Finland, for the optical microscopy of hardened concrete is the ASTM C856 [34]. However, the standard does not cover

fluorescence microscopy, which is a commonly used aid for recognizing porosity and cracking in concrete and aggregate.

3.　　　RESEARCH DATA AND METHODOLOGY

The research data consists of 15 condition investigation reports and 84 thin section analysis reports, made during the years 2005-2017, in which ASR had been identified. The basic aim of a condition investigation is to produce information about the factors affecting the condition and the performance of the structure, and to consequently produce information about the need and the options for repair of the building or the structure for the owner. Damage to structures, as well as the degree and extent of damage, due to various degradation phenomena, can be determined by a comprehensive systematic condition investigation [35, 36]. The thin section analysis facilitates recognizing the degradation phenomena, causing the damage found in the condition investigation. However, the lack of common reporting practises complicates comparing the data, even if the analysis done following the same standard practice.

In this study the most important information surveyed from the condition investigation reports and thin section analysis reports was:

- Geographical location of the concrete structure
- Age of the concrete structure when ASR was detected
- The findings of the thin section analyses (reacting particles and cement type), number of reports was 84
- Tensile strength of concrete, number of samples was 71
- Compressive strength of concrete, number of samples was 29.

The factors affecting the development of ASR were studied in a literature review. The research material combined from condition investigation reports is quantitative by nature. This data has been studied with statistical analysis.

4.　　　RESULTS AND DISCUSSION

4.1　　　Occurrence of ASR

Of the 84 cases, in which ASR had been found, 16 were facades and balconies, 23 bridges, 6 swimming pools and 7 other concrete structures. Most of the cases were in Oulu (16), the capital area (15) and Tampere (5), see fig. 5. ASR cases are not concentrated in one geographical area, but spread across Finland. ASR is mostly detected in the areas where there is built environment. Therefore, in Lapland where there is less built environment and renovation activities, there has been no reported data on ASR.

Figure 5 – The locations of detected ASR cases.

4.2   Initiation time for ASR

Average age and standard deviations of different concrete structures are presented in table 1. The age of the structure has been calculated from the year the condition investigation, in which the ASR was reported, has been conducted. Condition investigations of the structures were carried out in order to assess the repair needs of the structure, not specifically in order to find ASR. Some of the investigations were initiated because of visible deterioration, e.g. corrosion damage of reinforcement, but other structures were surveyed within a fixed-term monitoring. Therefore, the real initiation time for ASR is shorter than shown in table 1 and the age does not fully correlate to the emergence of visible deterioration.

Table 1 – The number of ASR cases and the average initiation age of structures.

Structure	Building years	Average age [years]	Standard deviation [years]	Number of cases
Facades and balconies	1919-1990	37	17	16
Bridges	1925-2002	44	15	23
Swimming pools	1960-1980	42	8	6
Others	1901-1995	47	31	7

As seen on the table, the structures have been built during a very long period of time. The first structure was built in 1901 and the newest one in 2002. Therefore, it is obvious that the standard deviation of ASR detection year is very large.

4.3 Cement type

There's variation in the reporting practices and accuracy in respect of cement type, and it is probable the substitute cementitious substances have not been mentioned in all reports, even if they have been used. Cement type was reported in 75 thin section analyses. The cement type was Portland cement (OPC) in 57 cases, OPC blended with blast furnace slag (BFS) in 15 cases and OPC blended with pulverized fly ash (PFA) in 3 cases, see fig. 6. Similar results on cement type have been found in [7]. It must be noticed, that all blended cements in Finland consists mostly of OPC. Fly ash or slag content in those cements is always mostly 20 %.
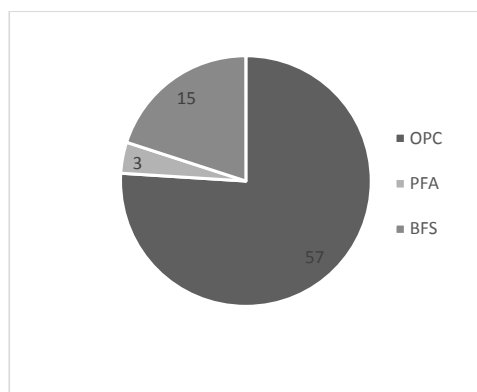

Figure 6 – Cement types detected in thin section analysis in ASR cases (n=75).

Alkali content of cement should be determined for estimating ASR possibility. Alkalinity of Portland clinker consists of sodium and potassium. Alkali content of cement can be determined as a Na_2O equivalent:

$$Na_2O_{EQ} = (Na_2O \% + 0.658 \ K_2O \%) \tag{1}$$

According to some standards [37, 38, 39] Na_2O_{EQ} should be less than 0.60%. Na_2O equivalent in mostly used Finnish cement types varies between 0.80% (CEM I 42.5 N-SR) and 1.35% (CEM II/A-LL 42.5 R). Nowadays the most used cement type is CEM II/A-M 42.5 N with 1.10% Na_2O_{EQ}. The most typical concrete grade is C30/37 with 300 kg/m^3 minimum amount of cement. Thus, it is obvious that Finland has a high possibility for ASR.

4.4 Reactive aggregate

Reactive aggregate is only occasionally reported in thin section reports in Finland. This could be due to different reasons: the reacting particles may not be present in the studied thin section, the reacting particle may be too small to be reliably identified to a specific rock type, or there may be differences in the reporting practises between the laboratories or petrographers. Whenever the aggregate is identified it is usually a granite or a metamorphic rock such as a gneiss, a quartzite or a schist. The unexpected dominance of granites may be due to granitic gneisses or migmatites being mistaken for granites, or the typical, micro-cracking, unrelated to ASR, of granites. These are similar to the aggregates reported in [7]. These are also the most common rock types found in the Finnish bedrock. As can be seen in fig. 7, Finnish bedrock is relatively metamorphosed thoroughly. Most of the aggregate used at the time the surveyed structures were built is natural or crushed rock from glacofluvial deposits. However, since the mean glacial transport distances are mostly less than 5 km [40], a correlation to the local country rocks can be expected.
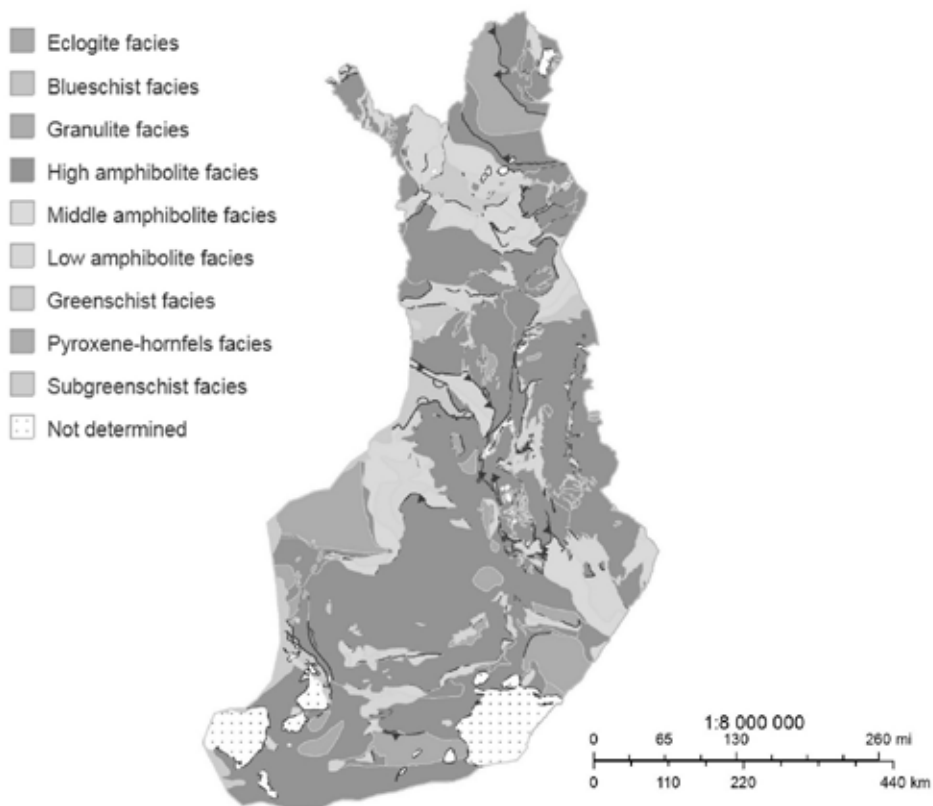
Figure 7 – Metamorphism of Finland from [41, 42].

4.5 Tensile strength of concrete

ASR causes cracking in concrete. Therefore, it affects the tensile strength of concrete rather than the compressive strength. Tensile strength test results were available from three swimming pools, see table 2. All tests cores were drilled towards to the smallest dimension of the structure.

Table 2 – Tensile strength results from three swimming pools.

Swimming pool	Tensile strength Min [MPa]	Max [MPa]	Number of samples	Results ≤ 0.5 MPa [No.]	Results ≤ 0.7 MPa [No.]
A	0.7	3.6	36	0	1
B	0.4	3.0	17	4	3
C	0.4	3.1	18	2	1

ASR can be reliably detected from thin section analysis, but the degree of ASR can be found out with tensile strength test. Observation of ASR gel does not indicate how the aggregate or concrete will crack [24]. Therefore, parallel test methods, thin section analyses and tensile strength tests are needed to ensure ASR in concrete structure. As seen on table 2, those swimming pools have also serious problems with ASR in spite of the number of relatively good tensile strengths.

4.6 Compressive strength of concrete

A total of 29 compressive strength tests were carried out according to the SFS-EN 12390-3 standard. Seven samples were cut in more than one part to determine the variation in compressive strength of concrete at different depths. The compressive strength of concrete was, on average, 61.5 MPa and standard deviation 11.4 MPa. Thus, unlike the tensile strength tests, the compressive strength tests of concrete did not indicate disintegration of concrete. Disintegration of concrete weakens the bond between the aggregate and the cement paste which affects the tensile strength of concrete before its compressive strength. This might be because compressive strength of concrete is not as good an indicator of disintegration as tensile strength.

5. CONCLUSIONS

According to research data, ASR is occurring all over Finland because of the relatively metamorphosed bedrock and the high alkali content of the cement. Reactive aggregates are classified to be relatively stable aggregates in literature, which explains why the occurrence of ASR has been taken round 40 years. However, the swimming pool environment is the most favourable for ASR, because of the constant high temperature and humidity. That is why ASR has been detected in swimming pools already around 30 years of age. Based on the research it is only a matter of time when ASR takes place in concrete structures, with potentially reactive aggregate, exposed to constant high humidity.

Optical microscopy of concrete thin sections is a reliable test method for detecting ASR in concrete. However, thin section analysis alone is not enough to ensure the progress of ASR in concrete. Thin section analyses should be supplemented with tensile strength tests. Tensile strength tests of concrete are found to be more representative for the state of disintegration of concrete than compressive strength tests.
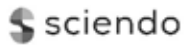
REFERENCES

1. Richardson, M. G., "Fundamentals of durable reinforced concrete," London, Spon Press, 2002, 260 p.
2. Shayan, A. & Quick, G.W., "Alkali-aggregate reaction in concrete railway sleepers from Finland," *Proceedings*, 16th International Conference on Cement Microscopy, Richmond, Va., USA, 1994, pp. 69–79.
3. Pyy, H., Holt, E., Ferreira, M., "Prestudy on alkali aggregate reaction and its existing in Finland," VTT, Helsinki, *Report* VTT-CR-00554-12/FI, 2012, 27 p. (in Finnish)
4. Lahdensivu, J., Aromaa, J., "Repair of alkali aggregate reaction damaged swimming pool," *Case Studies in Construction Materials*, Vol. 3, 2015, pp. 1-8.
5. Lahdensivu, J., Köliö, A., Husaini, D., "ASR possibilities in Finnish concrete bridges", In Grantham, M. G, Papayianni, I., Sideris, K. (editors) Concrete Solutions, Taylor & Francis Group, 6000 Broken Sound Parkway NW, Suite 300, Boca Raton, FL 33487-2742 CRC Press, 2016, pp. 61-64.
6. Appelquist, K., Trägårdh, J., Döse, M. & Göransson, M. "Alkali silica-reactivity of Swedish aggregates used for concrete," *Proceedings*, Nordic-Baltic workshop on Alkali aggregate reactions (AAR) in concrete, Riga, Latvia, 2013, pp. 41-54.
7. Appelquist, K., Mueller, U. & Trädgårdh, J., "Detection of Potential Alkali-Silica Reactivity of Aggregate from Sweden," *Proceedings*, 16th Euroseminar on Microscopy Applied to Building Materials EMABM, Book of abstracts, Les Diablerets, Switzerland, May 14-17, 2017, pp. 23-26.
8. McConnell, D., Mielenz, R. C., Holland, W. Y., and Greene, K. T., "Cement-Aggregate Reaction in Concrete," *Journal of the American Concrete Institute*, JACIA, Proceedings, Vol 44, October 1947, pp.93–128.
9. Mather, B., "Cracking of Concrete in the Tuscaloosa Lock," High-way Research Board *Proceedings*, HIRPA, Vol 51, 1951, pp. 218–233.
10. Thaulow, N., Andersen, K.T., "Ny viden om alkali-kisel reaktioner," *Dansk Beton*, No. 1, 1988, pp. 14-19. (In Danish).
11. Gilliot, J. E. "Practical implications of the mechanisms of alkali-aggregate reactions," In *Proceedings*, Third international conference on alkali-aggregate reaction, Reykjavik, 1975.
12. Jensen V. 2009. "Alkali Carbonate Reaction (ACR) and RILEM AAR-0 annex A: Assessment of potentially reactivity of carbonate rocks," *Proceedings*, 12th Euroseminar on Microscopy Applied to Building Materials, 15.-19. September 2009, Dortmund, Germany.
13. Jensen V. 2012a. "The controversy of alkali carbonate reaction: state of art on the reaction mechanism," *Proceedings*, 14th Int. Conference on AAR, Texas, USA.
14. Jensen V. 2012b. "Reclassification of Alkali Aggregate Reaction," *Proceedings*, 14th Int. Conference on AAR, Texas, USA.
15. Neville, A., "Properties of concrete," Essex, Longman Group, 1995, 844 p.
16. Nilsson, L-O. & Peterson, O., "Alkali-silica reactions in Scania, Sweden: a moisture problem causing pop-outs in concrete floors," *Repor*t TVBM; Vol. 3014, Division of Building Materials, LTH, Lund University, Lund, Sweden, 1983.

17. Poole, A. B., "Introduction to alkali-aggregate reaction in concrete," In Swamy, R. N. (editor): The Alkali-Silica Reaction in Concrete, Taylor & Francis Group, 1991, pp. 1-29.

18. Holt, E. and Ferreira, M., "Addressing ASR in concrete construction in Finland," In Wigum, B.J. and Bager, D. H.(Eds.) Alkali Aggregate Reactions (AAR) in Concrete, *Proceedings*, Nordic – Baltic Workshop, 2013, pp. 1-16.

19. West, G., "Alkali-aggregate reaction in concrete roads and bridges," London, Thomas Telford Publications, 1996, 163 p.

20. Fernandes, I., dos Anjos Ribeiro, M., Broekmans, M.A.T.M. & Sims, I., "Petrographic Atlas: Characterisation of Aggregates Regarding Potential Reactivity to Alkalis," RILEM TC 219-ACS Recommended Guidance AAR-1.2, for Use with the RILEM AAR-1.1 Petrographic Examination Method, 2016, 193 p.

21. Gjørv, O. E., "Durability design of concrete structures in severe environments," Taylor & Francis, 2009, 220 p.

22. Stanton, T.E., "Expansion of Concrete through Reaction between Cement and Aggregate," *Proceedings*, American Society of Civil Engineers, Vol. 66, No. IO, 1940, pp. 178

23. Stanton, T. E., "Studies of Use of Pozzolans for Counteracting Excessive Concrete Expansion Resulting from Reaction between Aggregates and the Alkalies in Cement," Pozzolanic Materials in Mortars and Concretes, ASTM STP 99, American Society for Testing and Materials, Philadelphia, 1950, pp. 178-203.

24. Cox, H. P., Coleman, R. B. and White, L., "Effect of Blast Furnace Slag Cement on Alkali-Aggregate Reaction in Concrete," *Pit and Quarry*, Vol. 45, No. 5, 1950, pp. 95-96.

25. Barona de la, 0. F., "Alkali-Aggregate Expansion Corrected with Portland-Slag Cement," *Journal of the American Concrete Institute*, Vol. 22, No. 7, 1951, pp. 545-552.

26. Pepper, L., and Mather, B., "Effectiveness of Mineral Admixtures in Preventing Excessive Expansion of Concrete Due to Alkali-Aggregate Reaction," *Proceedings*, ASTM, Vol. 59, 1959, pp. 178-1202, with discussion pp. 1202-1203, based on Buck, A. D., Houston, B. J. and Pepper, L., WESTechnical Report 6-48 1, July 1958, 31 pp.

27. Dunstan, E., "The Effect of Fly Ash on Concrete Alkali-Aggregate Reaction," *Cement, Concrete and Aggregates*, Vol. 3, No. 2, 1981, pp. 101-104

28. Thomas, M. D. A., "Review of the Effect of Fly Ash and Slag on Alkali-Aggregate Reaction in Concrete", Building Research Establishment Report BR 314, Construction Research Communications, Ltd., Watford, UK, 1996, 117 pp.

29. Punkki, J., Suominen, V., "Alkali aggregate reaction in Norway – and in Finland?, " *Betoni* No. 2, 1994, (Helsinki, Suomen Betonitieto Oy), pp. 30-32. (In Finnish).

30. Rønning, T., "Freeze-thaw resistance of concrete. Effect of curing conditions, moisture exchange and materials," *Doctoral thesis*, NTNU, Trondheim, Norway, 2001, 416 p.

31. Thaulow, N. and Jakobsen, U.H., "Deterioration of Concrete Diagnosed by Optical Microscopy," *Proceedings*, 6th Euroseminar of Microscopy Applied to Building Materials, June 25.-27., Reykjavik, Iceland, 1997a, pp. 282-296.

32. Thaulow, N. and Jakobsen, U.H., "The Diagnosis of Chemical Deterioration of Concrete by Optical Microscopy," In Scrivener, Y. (editor), Mechanism of Chemical Degradation of Cement-based Systems, E&FN Spon, 1997b, pp. 3-13.

33. Jakobsen, U.H., Johansen, V. and Thaulow, N., "Optical Microscopy - A Primary Tool in Concrete Examination," *Proceedings*. 19th ICMA Conference on Cement Microscopy, Illinois, USA, 1997, pp. 275-294.
34. ASTM C856-17, Standard Practice for Petrographic Examination of Hardened Concrete, ASTM International, West Conshohocken, PA, 2017.
35. Finnish Transport Agency, "Condition assessment manual for bridges," Guidelines of the Finnish Transport Agency 26/2013, 142 p. (In Finnish).
36. Lahdensivu, J., Varjonen, S., Pakkala, T., Köliö, A., "Systematic condition assessment of concrete facades and balconies exposed to outdoor climate," *Journal of sustainable building technology & urban development,* Vol. 4:3, 2013, pp. 199-209.
37. BS 4027, "Sulphate-resisting Portland Cement," British Standards Institution, 1996.
38. DIN 1164-10, "Zement mit besonderen Eigenschaften," German Standards, 2008.
39. NBN B 12-109, "Cement - Low alkali limited cement," Netherland Standards, 1993.
40. Salonen, V.-P. "Glacial transport distance distribution of surface boulders in Finland," Geological Survey of Finland, Bulletin 338, 1986, 57 p.
41. Hölttä, P. & Heilimo, E., "Metamorphic map of Finland," Geological Survey of Finland, *Special Paper* 60, 2017, pp 77-128
42. Geological survey of Finland, http://gtkdata.gtk.fi/Kalliopera/index.html, Referred Nov. 10th 2018.

Rice Husk Resource for Energy and Cementitious Products with Low CO$_2$ Contributions

Otto During, M.Sc.
RISE Built Environment
Stockholm, Sweden
otto.during@ri.se

Silu Bhochhibhoya, Ph.D.
Department of Construction Management and Engineering
Univeristy of Twente
Enschede, The Netherlands
s.bhochhibhoya@utwente.nl

Ramesh Kumar Maskey, Ph.D., Professor
Kathmandu University
Dhulikhel, Nepal
maskey@ku.edu.np

Rajendra Joshi, Ph.D., Associat Professor
Department of Chemical Science and Engineering
Kathmandu University
Dhulikhel, Nepal
rajendra.joshi@ku.edu.np

ABSTRACT

Rice Husk Ash (RHA) is a well-known supplementary cementitious materials (SCMs) that can be used for concrete with reduced CO_2 contributions. In 2016, only Nepal produced 5.2 million tonnes rice that gave about 1.14 million tonnes rice husk. The rice husk can also be used directly in a cement kiln as a fuel. This study analysis the potential CO_2 reductions from three scenarios and emphasis strengths, weaknesses, opportunities and treats in the production systems for initiate a decision process with possibilities to get an industry project financed from the green climate found. The highest CO_2 benefits were from rice husk used in a cement kiln were half of the yearly rice husk production in Nepal could reduce the climate impact with 808000 tonnes CO_2.

Key words: Carbon emission reduction, rice husk ash supplementary cementitious material, concrete, sustainable.

1.   INTRODUCTION

The global market for cement and concrete is increasing with the increasing population. It is the second biggest traded commodity in the world. There are two aspects of CO_2 emission from the cement production: (*i*) the chemical reaction involved in the production of the main component of cement, clinker, as carbonates are decomposed into oxides and (*ii*) CO_2 emission from the combustion of fossil fuels [1]. The demand for cement, especially in the developing countries, is expected to double within the next 20 years [2]. Hence, the need to reduce the carbon dioxide emissions associated with the production of cement is one of the major concerns of the cement and concrete industry. The use of supplementary cementitious materials (SCMs) is one of the effective solutions to counteract this effect [3-5]. Agricultural-based SCMs such as rice husk ash (RHA) can be a solution for many developing countries such as Nepal, whereby a large percentage of the economic workforce is focused on agriculture rather than industry.

Rice husks are agricultural by-products of paddy farming, which are not suitable for use as livestock feeding due to their lack of protein content. Hence, they are categorized as waste material and disposed in landfills. Worldwide production of rice husks amounts to approximately 100 million tonnes per year [6]. The combustion of the husks yields approximately 25% of ash [8- 9]. Research has shown that incineration of the husks under controlled conditions in temperatures not exceeding 700°C generates silica with the high amorphous content of approximately 90% or more [7], [8].

- RHA is a cheap waste material with no higher value for alternative use.
- RHA requires less energy than cement for its production
- The use of RHA as cement replacing materials reduces the carbon footprint.
- Optimizing RHA as a SCM also benefits the environment from eliminating the disposal of wastes onto land.

Rice husk is not new when it comes to transferring of low carbon technique to developing countries. The Clean Development Mechanisms, (CDM) in the Kyoto protocol have been used for many projects in India where rice husk is used for production of electricity and Certified Emission Reductions (CER). The amount of the CERs has been calculated according to the baseline for CO_2 emissions from electricity production in India. In CDM projects the CO_2 reductions have been focused on energy and not cement replacement.

This study aims to increase the use of Rice Husk Ash (RHA) in developing countries (with Nepal as a research example) for minimizing CO_2 emissions and increasing the use of local waste and other local materials. This study also aims to investigate a paradigm shift to produce concrete without Portland cement by looking at the antique way of producing concrete. The scenarios are followed below:

1. Rice husk for production of slaked lime and pozzolans as RHA and metakaolin for total substitution of Ordinary Portland Cement as binder.
2. Rice husk for production of heat and electricity and the pozzolan RHA for partly substitution of Ordinary Portland Cement as binder.
3. Rice husk for substituting fossil fuel in a cement kiln.

2. METHOD

Projects in developing countries, leading to reduction of CO_2, can get financing from the green climate fund coupled to the international climate convention. To be able to achieve money from the climate found the receiving country must have a plan how it will reduce the climate impact describing in the *Intended Nationally Determined Contributions* and the project shall be a way to implement some parts of the plan. Then the developing country contacts a member country of the climate convention to ask for financing from the fund. For starting a broad discussion in an early stage and not get locked to specific solutions too early, this paper provides a screening climate assessment and point out strength, weakness, opportunities and threat in the product systems lifecycles for three scenarios, SWOT analysis. The SWOT analysis is a starting point for a discussion for selecting of one of the scenarios, the questions are lifted by the writers for be discussed before a decision. The main focus shall be on strength and weakness in the selection process, but opportunities and threats could be lifted up to the level of strength and weakness if a deeper analysis will be done in these fields.

In the first scenario climate reductions are calculated by comparing a concrete produced from rice husk without any Portland cement with a compressive strength at 20 MPa with a standard concrete produced with Portland cement with the same strength. In the second scenario RHA are used as a supplementary material in concrete and the exchange factor are approximately the same as for silica fume, 1 part of RHA can replace 2 parts of cement. In scenario three the climate benefit is calculated by rice husk replacing fossil coal for production of cement. The upstream activities from Rice cultivation to Central Rice Husk storage are the same in al scenarios but the aspects of local or central activities are taken in account in the SWOT analysis, see appendix C.

3. SCENARIO 1: ROMAN CONCRETE AND POWER AND HEAT PRODUCTION

The rice husk is incinerated in a Fluidized Bed Combustion (FBC). Low temperature and good mixing in presence with air are preferred for getting a reactive ash with low rest carbon. RHA are added to the concrete as a pozzolan and even another pozzolan are added, metakaolin. There is tree reason why we add metakaolin: *i)* metakaolin is an aluminosilicate and the Roman concrete are known to include alumina and *ii)* metakaolin increase the reaction velocity and also *iii)* for not put in too much RHA and avoid low workability. The process produces both heat and electricity that can be used in the process for milling rice, grinding limestone, calcinate

limestone, dehydrate kaolin to metakaolin, and curing concrete if a concrete element production is integrated at the site. The Roman concrete has the compressive strength 20 MPa [9].

Table 1 – Mix design for 1 m³ modified Roman concrete

Material	Mass [kg]
Rice Husk Ash (m_{RHA}]	110
Slaked lime ($m_{Ca(OH)2}$)	200
Superplasticizer	2
Metakaolin	110
Water	230
Aggregates	1808

The chemical composition of RHA are described by Habeeb G A and Mahmud H B, 2010 [10]. High silica and low alkali and rest carbon (LOI) make RHA to a good pozzolan. Roman concrete from the antique were made of slaked lime and volcanic ash as binders. In this study we use the same recipe but instead of volcanic ash we use metakaolin (for increase heat development) and RHA for strong pozzolanic reaction. As RHA have a very big surface there is superplasticizer added to the recipe for increase in workability without increasing the water/cement ratio.

Table 2 – Chemical and physical properties of RHA.

Oxid composition	RHA [% by mass]
SiO_2	88.32
Al_2O_3	0.46
Fe_2O_3	0.67
CaO	0.67
MgO	0.44
Na_2O_3	0.12
K_2O	2.91
LOI	5.81
Specific gravity	2.11

The reference concrete recipe is chosen for giving the same compressive strength 20 MPa with Ordinary Portland Cement (OPC).

Table 3 – Mix design for the reference standard concrete.

Material	Mass [kg]
Cement	240
Water	170
Aggregates	1910

3.1   Energy production

Low heating value of rice husk: LHV_{husk}=13 GJ/tonne.
The energy (E) in the half of the production is

$$E = RH_{50} \times LHV_{husk}$$ (1)

E = 570 000 x 13 = 7400 TJ

The energy production in a 100 MW FBC is
7400 x 0.30/3600 = 0.61 TWh electricity and
7400 x 0.6/3600 = 1.23 TWh heat energy used for the process.

3.2   Product system

The system includes activities from raw materials to the product, a low to medium strength concrete. A concrete industry is integrated in the system for increasing the quality of the products and use energy from the process. Blue arrows are symbols for material flows and read arrows are symbols for energy flows were dotted arrows are for heat, see Figure 1.

Figure 1 – Scenario 1 Product system of producing modified Roman concrete.

3.3   Climate calculation

Production of electricity and heat from the FBC will not be significant under baseline for Nepal as common energy sources are hydropower and biofuels. But in certain amount, new energy in urban areas could replace ineffective stoves and heating systems that will lower the climate impact but most significantly make the contribution to the local air conditions by low NOx-

technique. The basic information and climate calculation scenario are mentioned in Appendices A and B.

More significant reductions on climate impact comes from cement replacement. If 50% of rice husk in Nepal were used, the half of the husk production (RH_{50}) can be calculated as:

$$RH_{50} = 0.5 \times R_{\mathrm{prod}} \times RH_{\mathrm{content}} \tag{2}$$

where R_{prod} is the total production of paddy rice in Nepal and RH_{content} is the rice husk content in paddy rice. RH_{50} = 0.5 x 5.2 x 0.22 = 0.57 million tonnes RH.

The rice husk ash from half of rice production (RHA$_{50}$) can be calculated as:

$$RHA_{50} = RH_{50} \times DM \times RHA_{\mathrm{content}} \tag{3}$$

where RHA_{content} is the ash amount in dry rice husk and DM is dry matter in rice husk. RHA_{50} = 570 000 x 0.88 x 0.25 = 125 000 tonnes RHA.

The CO_2 reductions of 1 tonne RHA ($CO_{2,\mathrm{red}}$) is 1.29 tonnes CO_2, see appendix A.
The CO_2 reduction capacity ($CO_{2,\mathrm{R}}$) for scenario 1 of using 50 % of annual rice husk in Nepal is:

$$CO_{2,\mathrm{R}} = RHA_{50} \times CO_{2,\mathrm{red}} \tag{4}$$

$CO_{2,\mathrm{R}}$ = 125 000 x 1.29 = <u>161 000 tonnes CO_2/ year</u>

4. SCENARIO 2: SUPPLEMENTARY CEMENTITIOUS MATERIAL (SCM) AND POWER AND HEAT PRODUCTION

The rice husk is incinerated in a Fluidized Bed Combustion (FBC). Low temperature and good mixing with air are preferred for getting a reactive ash with low rest carbon. The process produces both heat and electricity and the pozzolan RHA for partly substitution of cement.

4.1 Climate calculation

If 50% of rice husk were used for the production of RHA, the RHA_{50} = 125 000 tonnes. As RHA have very similar properties as Silica Fume. We assume that the replacement factor is 2. 1 kg RHA substitutes 2 kg cement. 125 000 tonnes RHA substitute 250 000 tonnes cement. The CO_2 reduction capacity for scenario 2 of using 50 % of annual rice husk in Nepal is the amount of replaced cement x emission factor for cement in Nepal (see appendix B) is 2 x 125 000 x 1.09 = <u>272 000 tonnes CO_2/ year.</u> The silica production is in the range of what could be used as 10 % SCM in 2.5 million tonnes concrete/year in Nepal. But export or other products could be good alternatives.
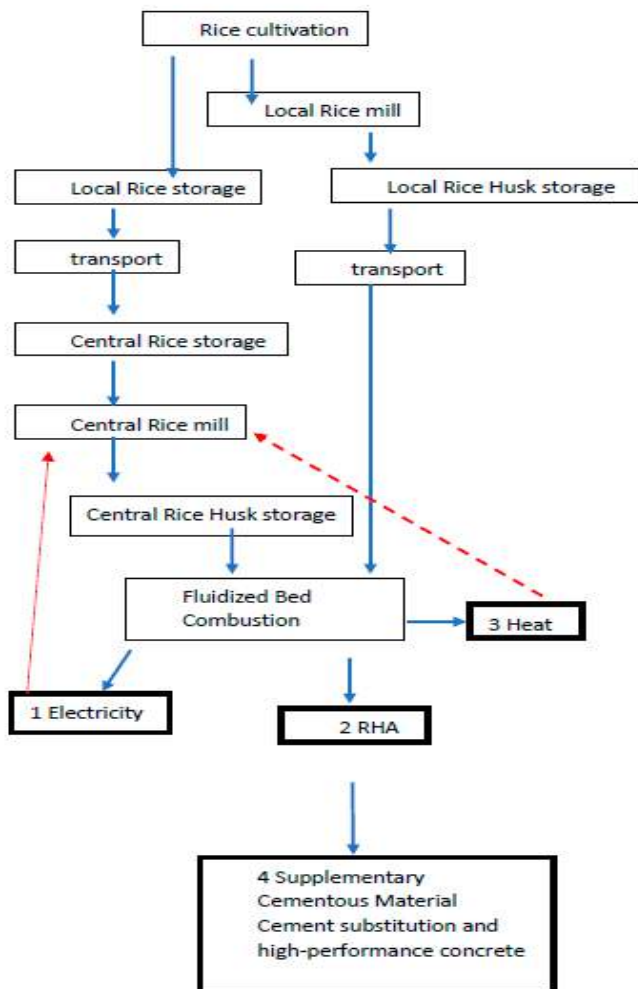
Figure 2 – Scenario 2 Product system for production of Energy and RHA and as a SCM.

4.2 Product system

The system includes activities from raw materials to the product, RHA. Blue arrows are symbols for material flows and read arrows are symbols for energy flows were dotted arrows are for heat, see Figure 2.
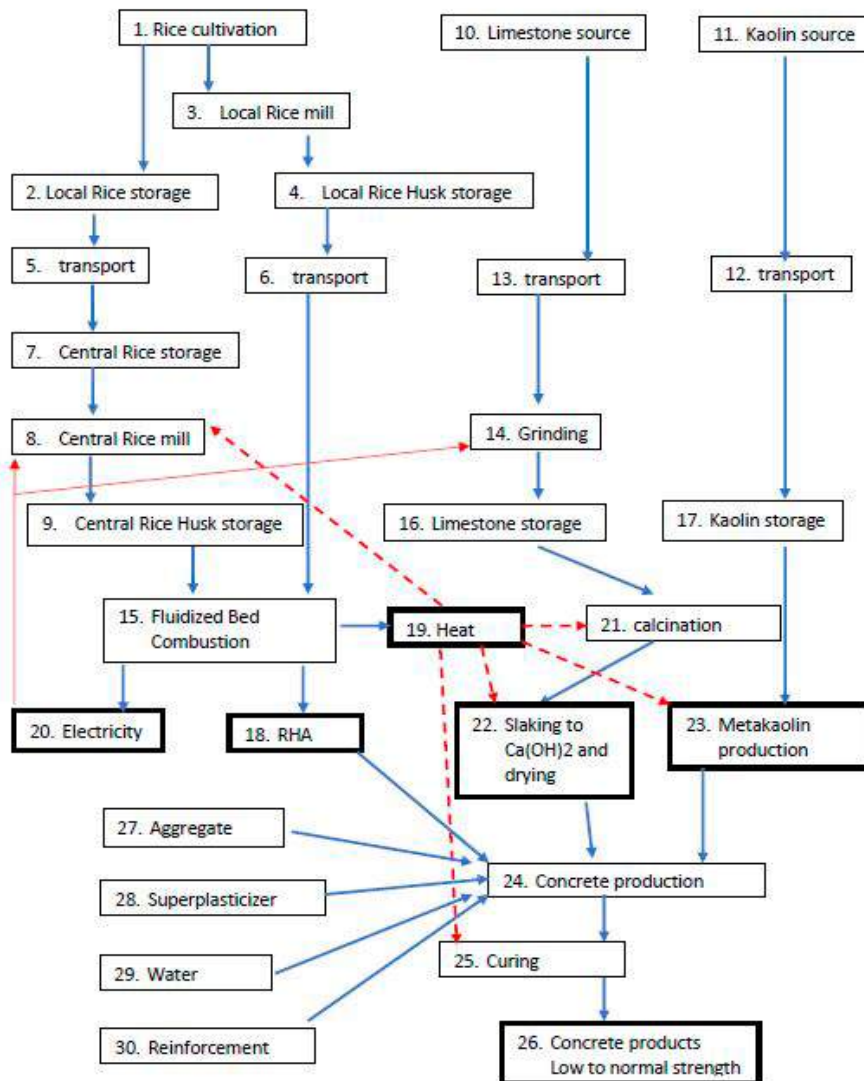
4.3 Energy production

The energy production in a 100 MW FBC if half of the rice production reused is 0.61 TWh electricity and 1.23 TWh Heat, see calculation Scenario 1.

5   SCENARIO 3: CEMENT PRODUCTION WITH RH AS FUEL AND SILICA SOURCE

The rice husk is used in a cement kiln for substituting fossil coal. To some content the RHA also substitute other silica sources for the production but no benefits are calculated for this.

5.1   Product system

The system includes activities from raw materials to the product, OPC Blue arrows are symbols for material flows, see Figure 3.

Figure 3 – Scenario 3, Rice husk as fuel in a rotary kiln for cement production.

5.2   Climate calculation

We assume that 50% of rice husk were used for the production of rice husk ash. RH_{50} = 570 000 tonnes, see scenario 1. The energy content is the amount multiplied with low heating value. The energy is 570 000 x 13 = 7 410 000 GJ.

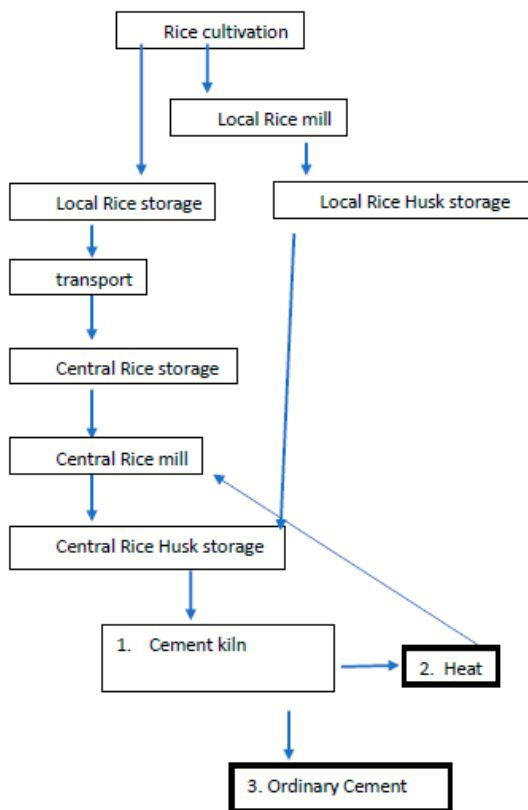In Nepal the average energy use for cement production is 5.4 GJ/tonne a cement. The cement production (C_3) of 7 410 000 GJ is 7 410 000 / 5.4 = 1.37 million tonnes. The CO_2 reduction capacity for scenario 3 of using 50 % of annual rice husk in Nepal is:

$CO_{2\ red} = m_{CO2,c}$ x C_3 = 0.59 x 1370 000 = 808 000 tonnes CO_2/ year.

The silica content in RH is 90 %. The amount of silica is 125 000 x 0.9 = 112 000 tonnes silica. In the cement production there is an input of 180 kg silica/tonne cement. The silica corresponds to 112 000 / 0.18 = 625 000 tonnes cement. If half of production of RH in Nepal were used in the national cement production, the RH stays for 625 / (0.7 x 2500) x 100 = 35% of the silica content in the cement.

6.   CONCLUSIONS

In scenario 1 the CO_2 reduction capacity for the Roman concrete and power and heat production of using 50% of annual rice husk in Nepal is 161 000 tonnes CO_2/year whereas, in scenario 2 the CO_2 reduction from Supplementary Cementitious Material (SCM) and power and heat production, of using 50% of annual rice husk in Nepal is 272000 tonnes CO_2/year. The potential energy production of using 50% of RH in a 100 MW FBC is estimated to be 0.61 TWh electricity and 1.23 TWh heat per year. For the cement production with RH as fuel and silicon source in scenario 3, the CO_2 reduction capacity using 50% of annual rice husk in Nepal is 808 000 tonnes CO_2/ year. The climate assessments show that scenario 3 have most climate benefits, see Figure 4.
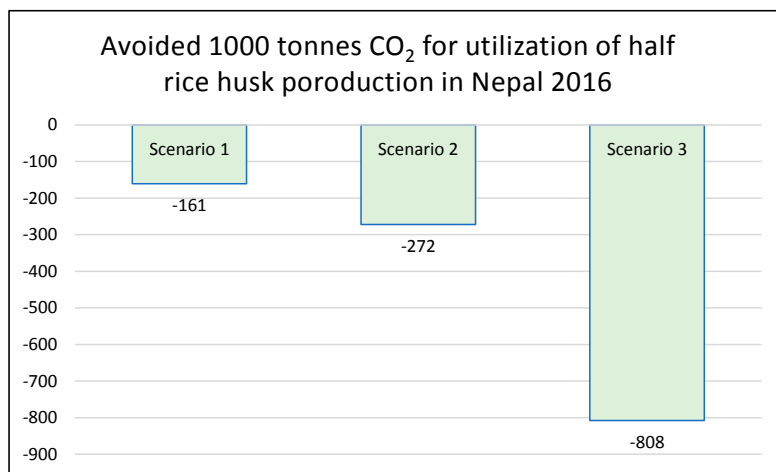

Figure 4 – Avoided CO_2 emissions.

The SWOT analysis, see appendix C, point out many benefits with scenario 2. There the most important strength is the electricity production from biofuel that is goal in Nepal's plan for reducing climate impact.

7.   DISCUSSION

The demand for cement, especially in the developing countries, is expected to double within the next 20 years. Hence, the need to reduce the carbon emissions associated with the production of cement is one of the major concerns of the cement and concrete industry. This paper focuses on different scenario for utilizing rice husk resource in Nepal for carbon neutral mineral products.

If the result will be applied for another country it is important to take in account that the result is calculated for a baseline with an energy use for cement production at 5.4 MJ/ton cement which is quite high and with electricity production from hydro power and biofuel. Therefor the scenario 2 and to some extent even scenario 1 will have more avoided CO_2 in a country that use fossil fuels for electricity production. The baseline for electricity production for Nepal is calculated for big scale energy production, if we instead look at small stoves in homes in the capital of Nepal, they often are fired with coal. It is possible that a new large-scale production of heat and power to some extent will replace the stoves in the hoses. This will both increase the avoided emissions for scenario 2 and give a significant positive contribution to the air quality in the city. The use of RHA as pozzolan and substituting cement give a high strength concrete and are quite easy to do [10]. In future research a cost analysis and identification of opportunities and threats could be studied.

REFERENCES

1.   Andrew R M: "Global CO_2 Emissions from Cement Production," *Earth Syst. Sci. Data*, Oslo, Norway, No. 10, 2017, 195-217, 2017.
2.   Herzog T and Billings B: "Navigating the Numbers," World Resource Institute, 2005.
3.   Schneider M, Romer M, Tschudin M, and Bolio H, "Sustainable Cement Production - Present and Future," *Cem. Concr. Res.*, Vol. 41, No. 7, 2011, pp. 642–650.
4.   Wray P, "Straight Talk with Karen Scrivener on Cements, CO_2 and Sustainable Development," *Am. Ceram. Soc. Bull.*, Vol. 91, June-July 2012, pp. 47-50.
5.   Baumert K A, Herzog T, Pershing J, and Billings H, "Navigating the Numbers Greenhouse Gas Data and International Climate Policy," Libr. Congr. Control Number, 2005.
6.   Food and Agriculture Organization of the United Nations, "FAO Rice Market Monitor Food," Rome, Italy, 2015.
7.   Rao K and Anusha P P R T, "Stabilization of Expansive Soil with Rice Husk, Lime and Gypsum – An Experimental Study," *Int. J. Eng. Sci. Technol.*, 2011, pp. 8076–808.
8.   Malhotra V.M. and Mehta P.K., Pozzolanic and Cementitious Materials. Gordon and Breach, Amsterdam, The Netherlands, 1996.
9.   Pages L: "Low Carbon Emission Cement Using Bio Origin Pozzolan," *Degree Project* FEI , RISE Swedish Cement & Concrete Research Institute, Stockholm, Sweden, 2018.
10.   Habeeb G A and Mahmud H B, "Study on Properties of Rice Husk Ash and Its Use as Cement Replacement Material", *Materials Research*, Vol. 13, No. 2, 2010, pp. 185-190.

APPENDIX A

Input data to the analysis:

Production of milled rice in world: 500 million tonnes/year

Production of paddy rice (husk+ rice) in Nepal (R_{prod}): 5.2 million tonnes (2016)

% RH of rice ($RH_{content}$): 22%

Moist content in rice husk: 12%

RHA of rice husk: 25%

Silicon dioxide of rice husk ash: 90%

Carbon of rice husk: part organic of RH: 0.71and part C of organic: 0.4 gives 0.284

Density of rice husk: 86-114 kg/m^3

Low heating value of rice husk: 13 MJ/kg, dry content 88%

Thermal efficiency of large 100 MW fluidized bed combustion: 60%

Electricity efficiency of large 100 MW fluidized bed combustion: 30%

Thermal efficiency of local 10 MW combustion: 40%

Electricity efficiency of local 10 MW combustion: 20%

Heat used for production of 1 tonne cement: 5.4 GJ, most wet kilns

Power used for production of 1 tonne cement: 148 kWh

Silica used for production of 1 tonne cement: 180 kg

Part of CaO by weight in cement: $x_{CaO} = 0.64$

CO_2 emission from 1 MJ coal: 110 g CO_2

CO_2 emission from 1 kWh electricity in Nepal: 5 g CO_2, hydropower

CO2 emission from 40 tonnes full packed lorry: 60 g CO_2/tonnes, km

CO_2 emission from 40 tonnes 30% packed lorry: 180 g CO_2/tonnes, km

Cement consumption in Nepal: 2.5 million tonnes/year. In 2010, 30% import from India.

APPENDIX B

Climate calculation Scenario 1

Molar weight (OH)$_2$, $M_{(OH)2}$ = 34
Molar weight Ca, M_{Ca} = 40
Molar weight CO$_2$, M_{CO2} = 44
Molar weight CaO, M_{CaO} = 56
Energy (coal) used for cement production in Nepal: E_{cement} = 5.4 GJ/tonne
CO$_2$ emissions from coal combustion: e_{coal} = 0.11 kg CO$_2$/MJ
CaO content in cement: x_{CaO} = 0.64 kg/kg

Production of 1 m^3 Roman concrete
Lime production: 200 kg
RHA use: m_{RHA} =110 kg
Calcination of limestone when heated: CaCO$_3$ = CaO + CO$_2$
Slaking quick lime: CaO + H$_2$O = Ca(OH)$_2$ (slaked lime)
For one part slaked lime there is production of one part CO$_2$ due to calcination.

CO$_2$ emission (m$_{CO2}$) from production of lime for 1 m^3 Roman concrete:
m_{CO2} = $m_{Ca(OH)2}$ x M_{CO2}/$M_{(CaOH)2}$
(1)m_{CO2} = 200 x 44 / 74 = 119 kg CO$_2$/m^3 concrete

Production Standard concrete
The most significant climate impact is the 240 kg cement use with Nepal conditions
CO$_2$ from cement production comes from fossil fuel used (5.4 MJ/kg) and calcination
CO$_2$ from fuel: $m_{CO2,c}$ = E_{cement} x e_{coal} = 5.4 x 0.11 = 0.59 kg CO$_2$/kg cement

CO$_2$ release from calcination. CaCO$_3$ = CaO+CO$_2$
CO_2calcination = x_{CaO} x (M_{CO2}/ M_{CaO})
CO_2calcination = 0.64 x (44/56) = 0.5 kg CO$_2$/kg cement
The CO$_2$ emissions from a typical cement in Nepal
$CO_{2,cem,Nepal}$ = 0.5 +0.59 = 1.09 kg CO$_2$/kg cement
Total CO$_2$ emissions for 1 m3 concrete with 240 kg cement
(2) m_{CO2} = m_{cem} * $CO_{2,cem,Nepal}$ = 240 x 1.09 = 261 kg CO$_2$/m^3 concrete.

Climate impact reduction: $CO_{2\ red}$ = $m_{CO2\ (2)}$ - $m_{CO2\ (1)}$ = 261-119 = 142 kg CO$_2$/m^3 concrete
Climate reduction for 1 kg RHA: $CO_{2,red/kg}$ = $CO_{2,red}/m_{RHA}$ = 142/110 = 1.29 kg CO$_2$/kg RHA

APPENDIX C

Activity	SWOT Analysis	Scenario		
	Strengths	**1**	**2**	**3**
Rice cultivation	1140 000 tonnes of RH in Nepal make it to a big national resource.	1	2	3
Rice cultivation	Over 100 million tonnes of RH in the world. The world potential for CO_2 reductions are big.	1	2	3
Local rice storage	Local storage secure food near the population.	1	2	3
Local rice husk storage	Local storage relieves the central production site.	1	2	3
Fluidized Bed Combustion, FBC	Temperature could be below 700°C to produce amorphous silicon dioxide - Low temperature give low NOx emissions.	1	2	
Lime Stone Resources	Resources available in Nepal.	1		
Kaolin Resources	Some resources available in Nepal if we will use metakaolin in the concrete mix.	1		
RHA	RHA could be used in many applications as a silicon source	1	2	
RHA	Very high content of amorphous silica in RHA make it good as a pozzolan.	1	2	
Electricity / Heat	The potential energy production of using 50% of RH in a 100 MW FBC are estimated to be 0.61 TWh electricity and 1.23 TWh heat per year.		2	
Electricity	Included in Nepal Goal in Intended Nationally Determined Contributions. Help to industrialize the country and provide low CO_2 energy.		2	
Electricity	Could be used for grinding and milling.	1	2	
Heat	Could be used for production of metakaolin, lime, rice processing, curing concrete etc.	1		
Heat	Could be used for rice processing and with district heating households and industry etc.		2	
Heat	Could be used for district heating etc.		2	3
Cement kiln	Known technique, Product standards, Building Standard, Silica comes with the fuel.			3
Ordinary cement	Standard product.			3
	Weaknesses			
Rice cultivation	Methane emission under anaerobe conditions contribute to global warming.	1	2	3
Local rice mill	Effective use of energy from rice husk is not so easy.	1	2	3
Local rice husk storage	Low density on RH demands large buildings for dry storage.	1	2	3
Transports	Long transports could lead to high climate impact and higher cost - Load capacity for rice husk in a big lorry is just 30% of max weight capacity. It is restricted by the low density. This gives about 180 g CO_2/ (tonne, km).	1	2	3
RHA	Workability of concrete decrease. Superplasticizer could be needed.	1	2	
	Opportunities			
Rice cultivation	Avoid anaerobic conditions in cultivation. Use rice with high silica content in husk.	1	2	3
Transports	If possible use train and non-fossil transport systems.	1	2	3
RHA	Pure silica could be produced for a lot of applications. Recycling of silica minimizes waste.		2	
Cement kiln	Potentially lower temperature is needed to produce clinker when rice husk is used as silica source.			3
	Threats			
Transports	A hilly country could make transports difficult and increase the energy and cost.	1	2	3
RHA	Rest carbon from insufficient incineration could inhibit superplasticizer and contribute to a dark concrete. The low albedo increases global warming. Lack of standard for RHA in concrete.	1	2	
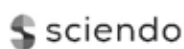
sciendo

Early Age Autogenous Shrinkage of Fibre Reinforced Concrete

Farid Ullah
M.Sc., Structural Engineer
Insinööritoimisto Mäkeläinen Ltd
(Engineering Office Mäkeläinen Ltd);
Äyritie 12 C, 01510 Vantaa, Finland

Fahim Al-Neshawy
D.Sc. (Tech.), Staff Scientist
Aalto University School of Engineering
Department of Civil Engineering
P.O.Box 12100, FIN-00076, Espoo, Finland
fahim.al-neshawy@aalto.fi

Jouni Punkki
D.Sc. (Tech.), Professor of Practice, Concrete Technology
Aalto University School of Engineering
Department of Civil Engineering
P.O.Box 12100, FIN-00076, Espoo, Finland
jouni.punkki@aalto.fi

ABSTRACT
Concrete is often sensitive to cracking during the hardening process, and these cracks could be the result of early-age shrinkage. One method to reduce shrinkage is to add different types of fibres to concrete. The aim of this study was to study the effects of different types of fibres on the early-age autogenous shrinkage of concrete. Three different types of fibre materials were used in the research. A "Schleibinger Bending-drain" test setup was used to record early-age autogenous shrinkage of fresh concrete immediately after mixing. The results show that, a fibre dosage of 0.38% by volume was found to be effective in reducing the effects of early-age autogenous shrinkage of concrete.

Key words: Autogenous shrinkage, cracking, steel fibre, thermal deformation, hydration.

1.   INTRODUCTION

1.1   Volumetric deformation of concrete

Volumetric deformation of concrete results from many contributing factors. Excessive shrinkage deformation may result in cracking of concrete members, which is detrimental to the durability of concrete structures. Loss of water over long duration due to drying is a common cause of shrinkage. However, shrinkage may also occur when the loss of water is prevented. This type of shrinkage is called autogenous shrinkage. Concretes with low water-to-binder ratio are more susceptible to shrinkage than concrete with high water-to-binder ratio. Shrinkage cracking or high probability of cracking in fresh concrete, presented in Figure 1, is a great concern and has been the focus of recent research in this field (name few references).

Figure 1. Plastic shrinkage cracking of concrete [1].

Shrinkage can be divided into many types based on the factors affecting the volume stability of concrete. However, overall shrinkage of concrete occurs in two phases, early-age and long-term shrinkage. Figure 2 shows the stages and types of shrinkage in concrete composites [2]. This paper is focusing on the early-age deformations occurring when concrete is setting and starts hardening in the first 24 hours.

Figure 2. Division of shrinkage stages and types [1].

1.2   Autogenous shrinkage

Autogenous shrinkage is a result of the internal chemical reactions of concrete raw materials without moisture loss to the surroundings. The various stages of hydration manifest themselves

in different stages of volumetric deformations of concrete. The deformation rate keeps on changing from the time of mixing water and cement, during setting and then hardening. The driving forces for the early-age deformation could be summed up as: (i) internal reactions of the mixture components and (ii) temperature and relative humidity (ambient conditions).

Loss of water, either due to evaporation or due to consumption in the hydration, gives rise to change of pore water configuration in the capillary pores. This type of deformation, with moisture loss due to evaporation, at an early-age is known as plastic shrinkage. During the very first hours of mixing, concrete is liquid and acts as a plastic. In high-performance concretes, which has less free water, autogenous shrinkage (when water is drawn from pores for hydration) is an important part of the total concrete shrinkage [3] [4] and [7]. Due to less amount of free water in high-strength concrete, water is drawn from the pores that develops a pore pressure, which becomes a driving force for shrinkage, as shown in Figure 3. Interplay of contracting forces such as capillary pressure and swelling forces such as thermal heating during early hydration, control the overall nature of the early age autogenous shrinkage.
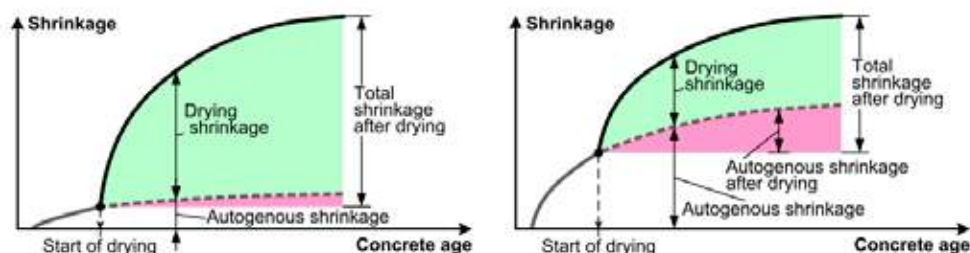
Figure 3. Shrinkage strain components in normal (left) and high-strength (right) concrete [8].

2.   EXPERIMENTAL PROCEDURE AND METHOD

2.1   Raw materials and concrete mix design

Measurements of the shrinkage on specimens were carried out according to the European standard EN13892–9:2017 [5]. The effect of fibres on the shrinkage of fibre reinforced concrete involved studying ten concrete mixtures using three cement types and three fibre types. All cement types were produced by Finnsementti Oy, Finland [9]. The types and specifications of fibres used in the research are presented in Table 1 and Figure 4.

Table 1. Types and specifications of the used fibers.

Type of fibers	Length (mm)	Diameter (mm)	Tensile strength (MPa)	Density (kg/m³)	No. of fibres /kg
Hooked–End steel fibre (ArcelorMittal, HE 1/50) [12]	50	1.00	1150	7850	3100
Plastic fibre (BASF, MasterFiber 246) [13].	40	0.75	448	910	~65000
Glass fibres (Owens Corning, Anti-Crack HP24) [14]	24	0.016	1000 – 1700	2680	

| Steel Fibres (HE 1/50) - ArcelorMittal | Plastic Fibres (Master Fibre 246) - BASF | Glass Fibres (Anti - Crack HP24) - Owens Corning |

Figure 4. Types of the used fibres.

Granitic aggregates were used in concrete mixtures with Plus and SR-cement, while limestone aggregates were used with white cement mixtures. Aggregates were washed, dried and graded by sieving. Concrete mixes were made by using the same aggregate grading. The water used was tap water from the water distribution system of Espoo city, Finland. The water's temperature was approximately + 20°C. Summary of composition of the test mixtures is given in Table 2.

Table 2. Mix proportions of concrete.

Mixture Code	PL-REF	PL-SF	PL-PF	PL-SF-SRA	WH-REF	WH-PF	WH-GF	SR-REF	SR-SF	SR-PF
Cement and water										
Plus Cement	✓	✓	✓	✓	-	-	-	-	-	-
White Cement	-	-	-	-	✓	✓	✓	-	-	-
SR Cement	-	-	-	-	-	-	-	✓	✓	✓
Cement (kg/m^3)	385	385	385	385	350	350	350	385	385	385
Water (kg/m^3)	194	194	194	194	194	194	194	194	194	194
w/c	0.50	0.50	0.50	0.50	0.55	0.55	0.55	0.50	0.50	0.50
Aggregate (kg/m^3)										
Filler TY 63	-	-	-	-	353	353	353	-	-	-
Limestone 22R 0/2	-	-	-	-	705	705	705	-	-	-
Limestone 22R 2/5	-	-	-	-	353	353	353	-	-	-
Limestone 22R 4/12	-	-	-	-	353	353	353	-	-	-
Filler 96	143	143	143	143	-	-	-	143	143	143
0.1/0.6 mm	161	161	161	161	-	-	-	161	161	161
0.5/1.2 mm	161	161	161	161	-	-	-	161	161	161
1 /2 mm	268	268	268	268	-	-	-	268	268	268
2/5 mm	268	268	268	268	-	-	-	268	268	268
5/10 mm	214	214	214	214	-	-	-	214	214	214
8/16 mm	572	572	572	572	-	-	-	572	572	572
Admixtures										
SP (kg/m³)	1.425	1.425	1.425	1.425	3.85	3.85	3.85	1.425	1.425	1.425
AEA (kg/m³)	-	-	-	-	0.15	0.15	0.15	-	-	-
SRA (kg/m³)	-	-	-	3.85	-	-	-	-	-	-
Steel fibres	-	✓	-	✓	-	-	-	-	✓	-
Plastic fibres	-	-	✓	-	-	✓	-	-	-	✓
Glass fibres	-	-	-	-	-	-	✓	-	-	-
Volume of fibres %	-	0.38	0.38	0.38	-	0.38	0.38	-	0.38	0.38
Air (dm^3/m^3)	20	20	20	20	50	50	50	20	20	20

The coding of the concrete mixes based on the cement type, fibre type and used admixture are presented below:

1) Plus cement (CEM II/B-M (SLL) 42.5N) concrete mixtures:
    1) **PL-REF** - Reference (plain) concrete
    2) **PL-SF** - Concrete with steel fibres
    3) **PL-PF** - Concrete with plastic fibres.
    4) **PL-SF-SRA** - Concrete with steel fibres and Shrinkage Reducing Admixture - SRA.
2) White cement (CEM I 52.5R) concrete mixtures:
    5) **WH-REF** - Reference (plain) concrete
    6) **WH-PF** - Concrete with plastic fibres
    7) **WH-GF** - Concrete with glass fibres.
3) SR cement (CEM I 42.5N SR) concrete mixtures:
    8) **SR-REF** - Reference (plain) concrete
    9) **SR-SF** - Concrete with steel fibres
    10) **SR-PF** - Concrete with plastic fibres

2.2   Preparation of the test specimens and measuring procedure

The effects of internal hydration reactions on the dimensional stability of fresh fibre concrete were investigated on a one-meter long shrinkage - rig called Bending-drain - curling profile apparatus from Schleibinger Testing Systems [15], presented in Figure 5.

Figure 5. Early-age deformation test with the Schleibinger Bending-Drain – rig.

The ten concrete mixtures (one sample / concrete) were tested in the shrinkage rig in which the samples were sealed to stop evaporation. The specimen temperature and linear deformation history for 48-hours in a control room of 20°C were recorded for each mixture type. These tests were started approximately 40 minutes after water and cement were mixed together. The testing was carried out according to European standard EN13892–9:2017 [5]. The method determines the unrestrained linear movement, shrinkage and swelling, of cementitious screed materials in a 1000 mm bending-drain apparatus. The deformation results were used to study the physical processes controlling different stages of the early-age deformation in fresh concrete. The results were presented as deformation–time graphs, which were plotted for each mixture after separating the thermal deformations from the raw data. Thermal deformations were calculated based on maturity (age and strength development) of concrete samples from the specimen temperature history.

In order to compare the different fibre materials in different cement mixtures, they were used in the same dosage (0.38% by volume). Due to different material densities, 0.38% by volume represents 30 kg/m^3 of hooked end steel, 3.82 kg/m^3 of plastic and 10.24 kg/m^3 of glass fibres respectively. The strength of concrete was C30/37, the consistency class was S3-class and the water-to-cement ratio was 0.50 for Plus and Sulfate Resisting (SR) cement concrete and 0.55 for White cement concrete mixtures.

3.   RESULTS AND DISCUSSION

3.1   Early-age deformation measurement

The early-age horizontal deformation (autogenous shrinkage + thermal deformation) measurement can be divided into three distinct stages. These stages are marked in the Figure 6 and described as follows:

- **Stage A: ~ (0 – 2½ hours)**
  At the start of the test, large horizontal shrinkage is recorded. The concrete at this stage is still fluid enough not to induce any harmful stresses due to this shrinkage. As the sample is placed in the U-shaped steel mould, the vertical placement exerts a force on the movable plate, which is partly cast into the sample for detecting horizontal deformation. This excessive early deformation does not exist for stiff or dry (little or no bleeding) mixtures.

- **Stage B: ~ (3 – 14 hours)**
  Thermal effects and bleed water reabsorption cause expansion of the sample from 3 - 14 hours into the test. Extra bleed water rises to the surface of the concrete sample as aggregates and cement particles settle. At a time when bleed water is completely absorbed into the concrete sample, the on-going hydration develops capillary pressure rise that is understood to be a main cause of early-age autogenous shrinkage deformation. Hydration reaction-controlled thermal expansion exceeds the capillary suction and causes large expansion.

- **Stage C: ~ (14 + hours)**
  At the end of hydration heat generation, the sample starts cooling which results in contraction of the concrete sample. The shrinkage during this continuing stage is somewhat exaggerated due to the cooling effect. With the progression of hydration, water availability becomes lesser within the microstructure of concrete sample, and capillary suction contributes to the autogenous shrinkage.
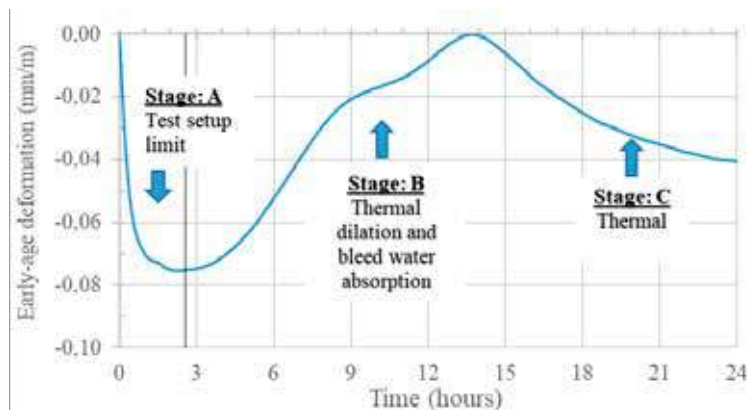
Figure 6. Stages of first 24 hours of the early-age deformation result for Plus cement concrete at w/c =0.50.

For evaluating the early-age autogenous shrinkage results for the aim of comparison, an engineering data interpretation approach was used [2]. The measured deformation of the test specimens over time consisted of (i) variations due to the shrinkage of the concrete, and (ii) variations due to changes in the temperature of the specimen.

The temperatures in the middle of the test specimens, and the corresponding changes in specimen length, were measured simultaneously. The variations over time of specimen shrinkage were determined from the differences between the development over time of the measured deformations, and the temperature expansion of the test specimens due to variations in temperature. Because the concrete temperature varied only during the period of rapid hydration of the cement (24 hours after mixing) and later approximately it was equal to the ambient temperature, the influence of temperature variations on the actual variations of specimen length has to be considered within the first 24 hours only. The variations over time of the test specimen deformation due to temperature variations in the period of rapid setting of the cement, i.e. in the first 24 hours, were determined analytically from the coefficient of thermal expansion of the concrete, and the measured variations over time of the temperature [4]. For estimating the thermal expansion coefficient (α_T) of concrete during the early-ages for time between 3-24 hours, Equation (1) was used.

$$\alpha_T = 193.9 \times t^{-0.86} \tag{1}$$

where: α_T = thermal expansion coefficient, (μ/°C), and
               t   = time between 3-24 hours, hours.

Constant values the thermal expansion coefficient are considered outside these time limits (for t < 3h, the $\alpha_T \approx 73 * 10^{-6}/°C$ and for t > 24h, $\alpha_T \approx 12 * 10^{-6}/°C$) [2]. The thermal expansion coefficient (α_T) is adjusted for each mixture based on the maturity concept. This helps to correct and take into account the temperature and strength development. The concrete age was adjusted according to Equation (2). This equation is valid for concretes made of Portland cements or cements containing only low amounts of components other than Portland cement clinker [6].

$$t_T = \sum_{i=1}^{n} \Delta t_i \times \exp\left[13.65 - \frac{4000}{273 + \frac{T_i}{T_0}}\right] \tag{2}$$

where: t_T = temperature adjusted concrete age.
         Δt_i = number of hours where a temperature T prevails.
         T_i = temperature during the time period Δt_i.
         T_0 = 1°C.

The thermal expansions is calculated by multiplying the maturity adjusted thermal expansion coefficient (α_T) with temperature differences from temperature history of concrete specimen using equation (3). An example of the calculated thermal expansions is presented in Figure 7.

$$\varepsilon_{\Delta T} = \alpha_T \times \Delta T \tag{3}$$

where: $\varepsilon_{\Delta T}$ = the thermal expansion, (mm/m).
         α_T = thermal expansion coefficient, (μ/°C).
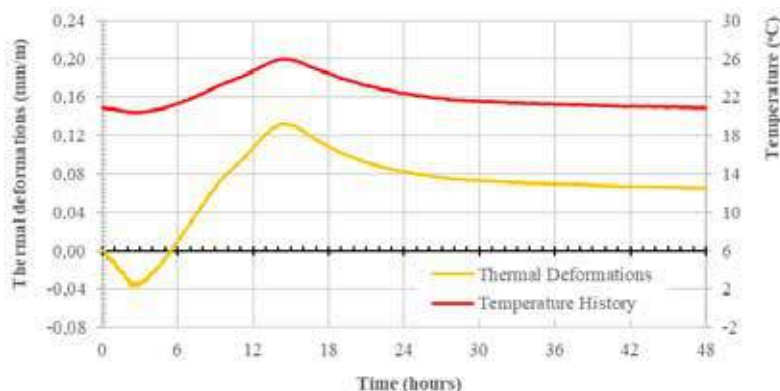 ΔT = the temperature differences, (°C)

Figure 7. Temperature development and consequent thermal deformations calculated from maturity-adjusted thermal expansion coefficient.

The early-age horizontal deformation is corrected following the development of thermal deformation calculation.

$$AD_{corr} = Measured\ deformation - thermal\ deformation$$
$$AD_{corr,zeroed} = AD_{corr} - Measured\ deformation\ value\ at\ the\ beginning\ of\ stage - B$$

Figure 8 shows the measured values of horizontal deformation from the Bending-drain test, thermal deformations calculated from maturity-adjusted thermal expansion coefficient, the corrected shrinkage following the thermal expansion (AD_{corr}) corrections and zeroed-corrected autogenous shrinkage ($AD_{corr,zeroed}$), which zeroed at the beginning of stage-B, see Figure 6.
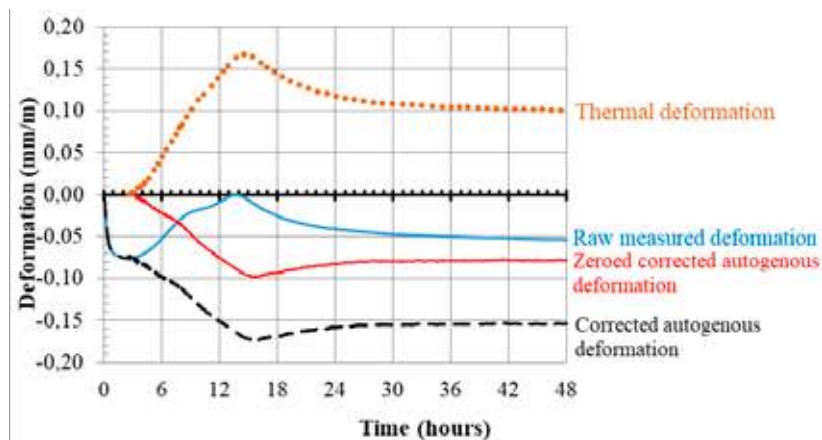
Figure 8. Measured autogenous deformation and corrected autogenous shrinkage.

3.2   Effect of different type of fibres

There is a general agreement among researchers that the addition of fibres to concrete have reducing effect on both the interior strain (due to autogenous effects) and the thermal expansion coefficient [16] and [17]. The fibres disrupt the interconnection of pores, reducing the overall water content in the capillary pore [18]. Increasing dosage of fibres in the concrete will reduce the overall thermal expansion coefficient of FRC.

The zeroed-corrected 48 hours autogenous shrinkage (along length) and temperature history (at the middle of specimen height) of Plus, White and SR cement concrete mixtures are shown in Figure 9, Figure 10 and Figure 11, respectively.
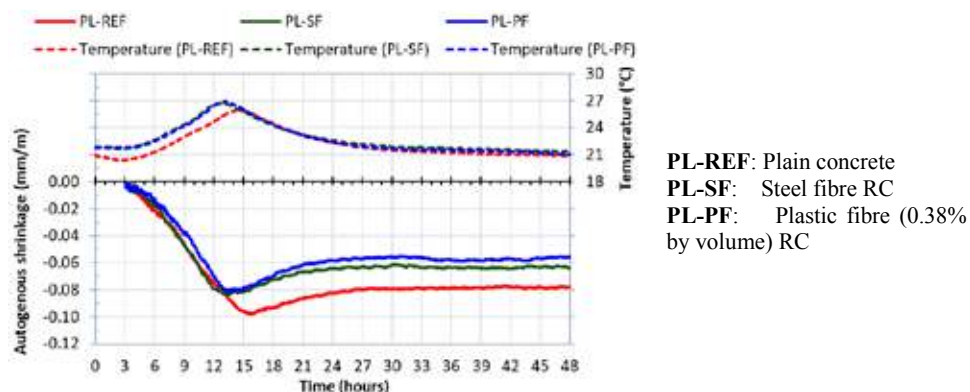

PL-REF: Plain concrete
PL-SF: Steel fibre RC
PL-PF: Plastic fibre (0.38% by volume) RC

Figure 9. Autogenous shrinkage and temperature history of Plus cement concrete mixtures.

For Plus cement concrete mixtures, it can be seen that early-age autogenous shrinkage of plain concrete was greater than with the fibres. The maximum autogenous shrinkage of steel fibre concrete was approximately 14% less than autogenous shrinkage of the plain concrete. Moreover, the maximum autogenous shrinkage of plastic fibre concrete was approximately

16.5% lesser than the maximum autogenous shrinkage of the plain concrete. At the end of test at 48 hours, the autogenous shrinkage of steel fibre concrete was approximately 18% less and the autogenous shrinkage of plastic fibre concrete was approximately 28% lesser than the autogenous shrinkage of the plain concrete mixture. It could be concluded that, with same dosage of fibre volume, plastic (polypropylene) fibres reduce the early-age autogenous shrinkage more than steel fibres do.
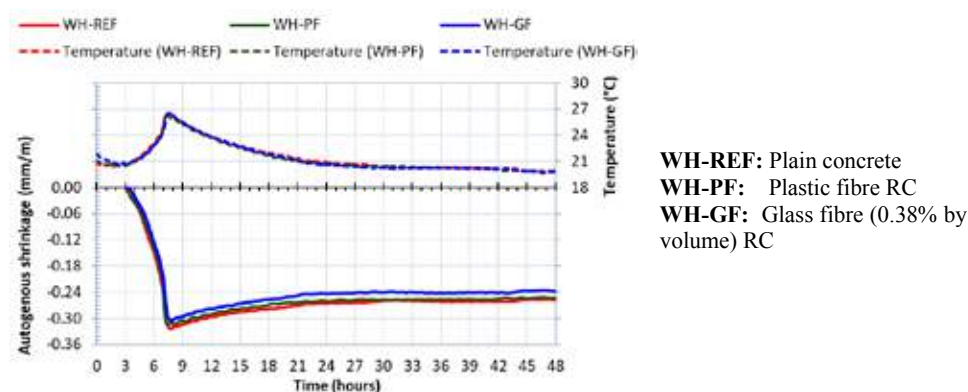

Figure 10. Autogenous shrinkage and temperature history of White cement concrete mixtures.

For White cement concrete mixtures, the fibrillated glass fibres performed almost twice as good in reducing shrinkage as the plastic fibres in case of White cement concrete. However, there was not much difference in total autogenous shrinkage of plain or fibre concrete for White cement. It could be concluded that, for the range of fibre content used in this work for White cement concrete, the fibres did not have a considerable effect on autogenous shrinkage like the case of Plus and SR fibre reinforced concrete mixtures.
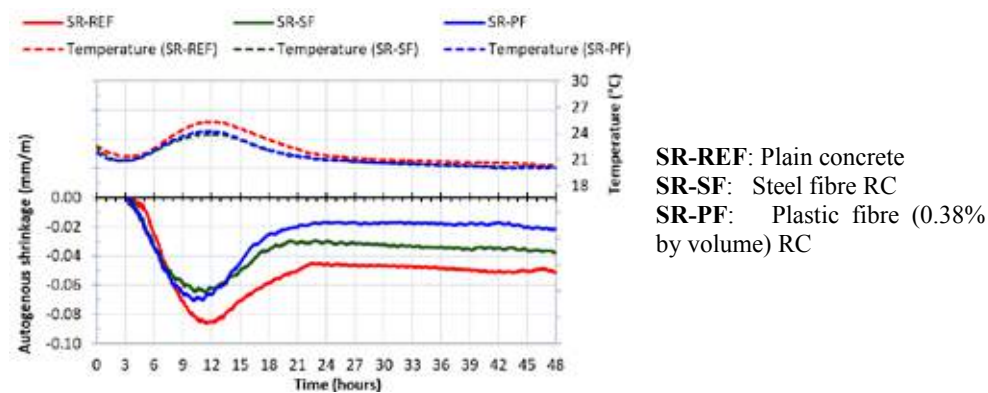

Figure 11. Autogenous shrinkage and temperature history of Sulfate Resisting (SR) cement concrete mixtures.

For Sulfate Resisting (SR) cement concrete mixtures, the early-age autogenous shrinkage of SR plain concrete was greater than with the addition of fibres. The maximum autogenous deformation of steel fibre concrete mix was approximately 24% less than that of maximum

autogenous shrinkage of plain concrete mix. The maximum autogenous shrinkage for plastic fibre concrete was found to be approximately 18% less than the maximum autogenous shrinkage of the plain concrete mix of SR cement. At 48 hours, the autogenous deformation of steel fibre concrete was approximately 27% less, and that of plastic fibre concrete was approximately 57% lesser than that of the plain SR cement concrete. The plastic fibres reduce the early-age autogenous shrinkage more than the steel fibers in the case of SR cement concrete too.

It was observed that the fibre reinforced concretes behaved similarly to plain concrete in the first few hours of the test. However, there were noticeable difference in the maximum and 48 hour autogenous shrinkage values. The autogenous shrinkage of fibre reinforced concrete was found to be lesser than that of plain concrete mixtures for all three types of cement mixtures. It might be because fibres reduce the autogenous shrinkage when they are subjected to the shrinkage-induced tensile stresses, by shear along the fibre-matrix interface [19].

3.3   Effect of Shrinkage Reducing Admixture (SRA)

To demonstrate the effect of Shrinkage Reducing Admixture (SRA), 1% (by weight of binder) dosage of BASF MasterLife 815 SRA was added to steel fibre reinforced concrete (SFRC) using Plus cement, see Figure 12.

PL-SF: Steel fibre RC
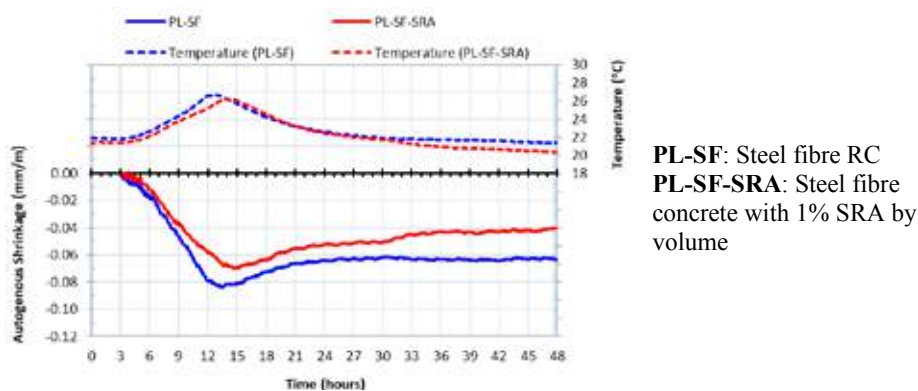**PL-SF-SRA**: Steel fibre concrete with 1% SRA by volume

Figure 12. Shrinkage Reducing Admixture effect on autogenous shrinkage and temperature history of steel fibre reinforced concrete mixtures.

A noticeable feature in Figure 12 is the delayed peak temperature rise and delayed maximum early-age autogenous deformation with the use of SRA. This side effect has been reported in previous studies and mentioned in the manufacturer's product documents. However, the perceived delay is within 1-hour period. The use of SRA reduced the maximum early-age autogenous deformation of SFRC by approximately 16.5%. Whereas, the reduction of early-age autogenous deformation at 48-hours was greater than 37%. However, the mixture containing 1% SRA showed greater workability (slump) and apparently more free water. This is a direct effect of reduced surface tension of the mixing water in the liquid stage.

3.4   Effect of cement type

Figure 13 shows the changes in autogenous shrinkage for plain concrete samples of the Plus, White and SR cement types. Same mixture design was used for Plus and SR cement types, with w/c ratio of 0.50. Mixture design for White cement concrete had a w/c ratio of 0.55 with four limestone 22R aggregate factions, more than twice amount of filler and maximum aggregate size of 12 mm.

The different clinker compositions and initial setting times of the cement types also reflected in the thermal changes as seen in the temperature history. In Figure 13, the shrinkage data was referenced at the start of thermally controlled deformations. The mixture with White cement (WH-REF) showed less bleed-water. After the peak temperature during hydration, rapid shrinkage was observed with white concrete mixtures. Other mixtures with Plus and SR cement exhibited thermal expansions exceeding the amount of early-age shrinkage.

Apart from the maximum magnitudes of the mixture temperatures and autogenous shrinkage, it can be seen that these temperature histories and autogenous shrinkage measurements are characteristic in nature. Qualitatively, they represent the material properties of the corresponding cement type mixture and the test arrangement. The temperature histories (PL-REF for Plus, WH-REF for White & SR-REF for SR) of plain concrete mixtures suggest that hydration reactions occur in a different way in these cement types. The high early heat of hydration causes thermal swelling in Plus and SR cement type mixtures. Whereas, it only resists the autogenous shrinkage deformations in the White cement mixtures. The thermal effects were removed from the raw autogenous deformation data using maturity adjusted thermal expansion coefficient. The corrected results confirm the same logic as White cement mixture type showed large amounts of corrected autogenous shrinkage, followed by Plus and SR type mixtures.
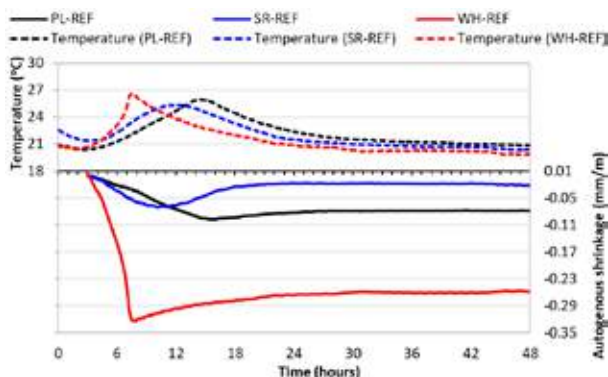
Figure 13. Comparison of autogenous shrinkage and temperature history of plain concretes with Plus, Sulfate Resisting and White cement.

4.   CONCLUSION

The autogenous shrinkage is of great concern since concretes with lower w/c ratios are more commonly used in applications such as high-performance concrete. With material optimization for structural concrete, autogenous shrinkage is of increasing concern as it can dictate the quality of concrete throughout the lifecycle of a structure. Fibre reinforced cement composites are

increasingly being used to address the problems of volumetric deformation-induced cracking. This experiment work was aimed to identify the beneficial effects of fibres in controlling the forces that drive both the early-age autogenous and long-term drying shrinkage deformations in concrete composites. A new experimental setup was used to study the effects of different types of fibers in concrete mixtures with different cement types.

Following trends are concluded from the tests of early-age autogenous shrinkage in this study:

- The early-age autogenous shrinkage of plain concrete samples was more than that of fibre-reinforced samples for all cement types. The fibre dosage of 0.38% by volume was found to be effective in reducing the effects of early-age autogenous shrinkage deformations.
- For the same dosage of fibres (0.38% by volume), the plastic (polypropylene) fibres were more effective than hooked-end steel fibres in reducing the early-age autogenous shrinkage.
- The effect of fibres in reducing early-age autogenous shrinkage in White cement concrete was less than the effect of fibres addition in Plus and SR cement concrete mixtures.
- Regarding the effect of cement type, the SR cement concrete exhibited both lesser early-age autogenous shrinkage and long-term drying shrinkage as compared to the Plus cement concrete. This effect is attributed to the difference in clinker composition of the respective cement types. Plus type cement, with a higher C3A, showed greater early-age autogenous and long-term drying shrinkage.
- The use of 1% by weight of cement of the Shrinkage Reducing Admixture (SRA) proved to be effective in reducing the early-age autogenous and long-term drying shrinkage deformation.

The general opinion that fibres allow more moisture escape by bridging the pores could not be established as similar average water loss (kg/m^3) was recorded for both the plain and fibre reinforced concrete mixtures.

REFERENCES

1. Orosz K: "Early Age Autogenous Deformation and Cracking of Cementitious Materials – Implications on Strengthening of Concrete Structures," *Doctoral thesis*, Luleå University of Technology Department of Civil, Environmental and Natural Resources Engineering. ISBN 978-91-7583-909-7 (pdf). Luleå, Sweden, 2017.
2. Holt E: "Early Age Autogenous Shrinkage of Concrete," *VTT Publication* No. 446, Technical Research Centre of Finland -VTT Publication 446, Espoo, Finland, 2001. [Online] http://www.vtt.fi/inf/pdf/publications/2001/P446.pdf. [Accessed 3.10.2018]
3. Barr B & El-Baden A: "Shrinkage Properties of Normal and High Strength Fibre Reinforced Concrete," *Proceedings*, Institution of Civil Engineers - Structures and Buildings, 2003, Volume 156:1, pp. 15-25. doi: 10.1680/stbu.2003.156.1.15.
4. Saje D, Bandelj B, Šušteršič J, Lopatič J & Saje F: "Autogenous and Drying Shrinkage of Fibre Reinforced High-Performance Concrete," *Journal of Advanced Concrete Technology*, Volume 10, No. 2, 2012, pp. 59-73
5. EN 13892-9 "Methods of Test for Screed Materials - Part 9: Determination of Shrinkage and Swelling," German and English version prEN 13892-9:2017.

6.   CEB-FIP Model Code (1990): Design Code. Comité Euro-International du Beton, Bulletin d'Information no. 213/214, Ed. Thomas Telford, 1993.
7.   Zhao S, Li C, Zhao M & Zhang X: "Experimental Study on Autogenous and Drying Shrinkage of Steel Fiber Reinforced Lightweight-Aggregate Concrete," *Advances in Materials Science and Engineering*, Vol. 2016, Article ID 2589383, 9 pp, 2016. doi:10.1155/2016/2589383
8.   Gribniak V, Kaklauskas G, Kliukas R & Jakubovskis R: "Shrinkage Effect on Short-Term Deformation Behavior of Reinforced Concrete – When It Should Not Be Neglected", *Materials and Design*, Vol. 51, 2013, pp. 1060-1070, ISSN 0261-3069. [Online] https://doi.org/10.1016/j.matdes.2013.05.028 [Accessed 3.10.2018].
9.   Finnsementti Oy, Cements. [Online] http://www.finnsementti.fi/en/products/cements [Accessed 3.10.2018].
10.   SFS-EN 12617-4:2002. "Products and Systems for the Protection and Repair of Concrete Structures. Test Methods. Determination of Shrinkage and Expansion." The Finnish Standards Association SFS.
11.   ISO 1920-8:2009 "Testing of Concrete - Part 8: Determination of Drying Shrinkage of Concrete for Samples Prepared in the Field or in the Laboratory".
12.   ArcelorMittal steel fibers [Online] http://ds.arcelormittal.com/wiresolutions/steelfibres/products/ [Accessed 3.10.2018]
13.   BASF. Master Builders Solutions. [Online] https://www.master-builders-solutions.basf.fi/fi-fi/products/masterfiber/354 [Accessed 3.10.2018].
14.   Owens Corning. "Owens Corning - Innovations for Living". [Online] http://www.cem-fil.com/ [Accessed 3.10.2018].
15.   Schleibinger Testing Systems [Online] http://www.schleibinger.com/cmsimple/en/?Shrinkage:Bending_Drain [Accessed 3.10.2018].
16.   Bazant Z P: "Delayed Thermal Dilatations of Cement Paste and Concrete due to Mass Transport," *Nuclear Eng. & Design*, 1970, pp. 308–318.
17.   Sellevold E J & Bjøntegaard Ø: "Coefficient of Thermal Expansion of Cement Paste and Concrete: Mechanisms of Moisture Interaction," *Mater. Struct.*, Vol. 39, No. 9, 2006, pp. 809–815.
18.   Lei Y & Cao, X: "Study on Thermal Dilation Coefficient of Fibre Concrete at Early Stage," *Applied Mechanics and Materials*, Vol. 99-100, 2011, pp. 777-781.
19.   Mangat P & Azari M: "A Theory for the Free Shrinkage of Steel Fibre Reinforced Cement Matrices," *Journal of Material Sciences*, Vol. 19, No. 7, 1984, pp. 2183-2194.
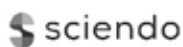
Prediction of Restraint Moments in Precast, Prestressed Structures Made Continuous

Ulla Kytölä, M.Sc
Ph.D. student
Dept. of Civil Engineering, Tampere University of Technology
Korkeakoulunkatu 5,
FI-33720 Tampere
E-mail: ulla.kytola@tut.fi

Anssi Laaksonen, D.Sc
Professor
Dept. of Civil Engineering, Tampere University of Technology
Korkeakoulunkatu 5,
FI-33720 Tampere
E-mail: anssi.laaksonen@tut.fi

ABSTRACT

This paper studies restraint moments developing in simple-span precast, prestressed beams made continuous. Methods of evaluating restraint moments produced by creep and differential shrinkage are presented. Shrinkage and creep properties of composite structures, beam and deck parts were tested and compared to values defined according to Eurocode models. Finally, the restraint moments were calculated with both material models for the two-span parking deck structure. The study confirmed the findings of previous studies: that the methods that are used overestimate the negative restraint moment produced by differential shrinkage.

Key words: Restraint moment, creep, differential shrinkage, continuity, prestressed concrete.

1.   INTRODUCTION

Heavily loaded building structures and congested building sites are growing more common in Finland due to urbanisation. In many projects, single-span, simply supported precast prestressed beams are insufficient to carry the imposed loads, making cast-in-place (CIP) concrete the only alternative. There is a need in the construction field to determine ways to increase the application of precast prestressed concrete girders, which facilitates working phases on site.

It is common in many parts of the world to construct multi-span bridges composed of simple-span precast prestressed girders and CIP decks. Simple-span girders are made continuous with a CIP connection over the supports and by post-tensioning. In this method, the girders act as simple spans for dead loads before the connection is completed. After continuity is achieved, the composite section of the prestressed beam and CIP deck slab carry the superimposed dead and live loads as a continuous structure. Compared to simple-span girders, the advantages of girder continuity are reduced bending moments, improved accident and seismic performance, and a reduction in the amount of needed expansion joints, which require lots of maintenance.

There has been a considerable amount of research concerning bridges constructed in this way. Continuity of precast, prestressed girders is also used to some extent in building structures, but there is only little information available about the experience gained from those structures. At Tampere University of Technology (TUT), a research project founded by the Finnish Concrete Industry has begun to study the potentials of simple-span precast, prestressed concrete girders made continuous in building structures with heavy loads.

Prestressed girders have a tendency to exhibit camber after prestress transfer due to the effect of creep. If the element is simply supported, the ends of it will rotate because of creep and no external loads are developed. When simply supported beams are connected together, their ends are restrained from any rotation; because of that, a positive restraint moment develops at the intermediate support. In this type of element girder – in-situ-slab composite structure the slab is cast after the girders. When the slab is cast, the girders have already had time to shrink and there is less shrinkage left, whereas the slab's shrinkage has only started. This strain difference between the slab and the girder is called differential shrinkage, and it is presumed to cause downward deflection to the composite structure. This movement is restrained in the structure's continuous supports, which causes negative restraint moment to the structure. The final restraint moment is the sum of the effect of creep and differential shrinkage, and it can be positive or negative. Temperature difference also produces restraint moments in statically indeterminate structures. Usually heavily loaded building structures have sufficient thermal insulation to prevent strong temperature variation caused by outdoor conditions. Hydration heat of the in-situ-deck concrete might still produce variations in the temperature distribution of the structure during the first few days after the casting [1]. Restraint moments caused by these temperature changes are not included in this paper.

EN1992-1-1 provides methods to evaluate creep and shrinkage. The amount and developing rate of creep and shrinkage can vary widely, and the value calculated with Eurocode methods may differ considerably from real strains. Because of this, many references recommend material testing of the concrete in question beforehand in order to obtain a more accurate analysis about restraint moments in the design phase [2, 3]. Evaluating restraint moments in the structure is important because they affect the continuity of the structure. If the positive restraint moment exceeds the cracking moment of the connection continuity may be lost. The positive restraint moment increases the tensile stresses of soffits in the span, whereas the negative moment adds

compression stresses to the soffits at the intermediate support. These effects should be taken into consideration in stress limitation checks and other SLS design, which normally controls the design of prestressed building structures in heavy exposure classes [3, 4, 5, 6].

2.   RESEARCH OBJECTIVE

This paper is a part of doctoral research, which focuses on extending the application of precast, prestressed concrete beams with continuity. The objective of this paper and the first phase of the study is to concentrate on time-dependent restraint moments of these kinds of structures. Following phases will concentrate on the properties and function of continuity connection between precast girders in different states. Furthermore, complete ½-scale continuous two-span composite girders will be constructed, tested and analysed.

The majority of the earlier research studies the problem from the standpoint of bridge girders made continuous. Dimensions and cross-sections differ from each other in building and bridge structures. The aim is to study the matter from the building structure point of view and estimate the magnitude of restraint moments.

The time-dependent properties of concrete have significant influence on restraint moments. It is recommended that tests should be conducted beforehand to evaluate true time-dependent strains [2,7]. In an experimental study, the properties of creep, shrinkage and elastic modulus were measured in typical types of Finnish concrete used in precast, prestressed elements and CIP slabs. An analytical tool was developed to evaluate restraint moments in simple-span girders made continuous. A representative composite two-span parking deck structure was selected for use as an example structure and studied. The calculation is made with two different material properties which are measured and defined according to EN 1992-1-1.

3.   BACKGROUND

3.1   Shrinkage and creep

Shrinkage consists of drying and autogenous shrinkage. Drying shrinkage denotes the reduction in volume resulting from a loss of water. Contrary to drying shrinkage, autogenous shrinkage doesn't involve moisture transition. It is the result of chemical shrinkage affiliated with the hydration of cement particles. The magnitude of shrinkage depends on the mix design, size and shape of the structure, relative humidity and concrete curing. EN1992-1-1 provides analytical formulas for predicting mean values for autogenous and drying shrinkage strain. The variance of shrinkage is assumed to be ±30%. The shrinkage strain is assumed to be constant within the cross section.

When concrete is loaded, it undergoes both elastic and viscous deformation. Elastic deformation happens quickly and the concrete returns to its original state once the load is removed. On the other hand, viscous deformation increases slowly with time as the concrete experiences a sustained load. This viscous property of concrete is called creep. The amount and developing rate of creep are influenced by aggregate, cement type, used additives, water-cement ratio, aggregate-cement ratio, the age of the concrete when first load is applied, duration and magnitude of load, temperature, relative humidity, size and shape of the structure, and concrete

curing [8]. Creep is usually described by means of a creep coefficient which is defined as the ratio of the given creep strain to the initial elastic strain. EN 1992-1-1 provides analytical formulas for predicting the development of the creep coefficient. The variance of creep is assumed to be ±20% [9].

Most of the things mentioned above can be taken into account in Eurocode equations when predicting creep and shrinkage, but there are also things that are disregarded. In Finland, the majority of prestressed concrete elements are manufactured from self-consolidating concrete (SCC), which has a high paste content. Because of this, SCC creeps and shrinks about 10-20% more compared to ordinary concrete according to studies. This is left out in the Eurocode equations on the basis that the strains are still within the variance mentioned earlier [2,9].

3.2 Strain under constant stress [2]

In the Effective Modulus Method (EMM), long-term deformations are calculated based on the effective modulus of elasticity of concrete, which can be calculated with Eq. (1).

$$E_{\text{c,eff}}(t, t_0) = \frac{E_{\text{cm}}(t_0)}{1 + \frac{E_{\text{cm}}(t_0)}{E_{\text{cm}}} \varphi(t, t_0)} \qquad (1)$$

where
$E_{\text{cm}}(t_0)$ is the modulus of elasticity at the time of loading t_0
E_{cm} is the modulus of elasticity at the age of 28 days
$\varphi(t, t_0)$ is the creep coefficient

Creep compliance function is the inverse of effective modulus of elasticity (Eq. (2)). Time-varying strains in concrete can be calculated by multiplication of the known stress and compliance function $\emptyset(t, t_0)$.

$$\emptyset(t, t_0) = \frac{1}{E_c(t_0)} + \frac{\varphi(t, t_0)}{E_c(28)} \qquad (2)$$

Strain $\varepsilon_c(t, t_0)$ of concrete at time t for constant compressive stress σ_0 applied to the concrete at the concrete age t_0 including shrinkage $\varepsilon_s(t)$ is

$$\varepsilon_c(t, t_0) = \sigma_0 \emptyset(t, t_0) + \varepsilon_s(t) = \sigma_0 \left(\frac{1}{E_c(t_0)} + \frac{\varphi(t, t_0)}{E_c(28)} \right) + \varepsilon_s(t) \qquad (3)$$

3.3 Strain under time-dependent stress

Concrete exhibits ageing. As time passes, concrete stiffness increases and creep rate decreases. If strains caused by time-dependent stress are predicted with EMM, the results are incorrect. EMM doesn't take into account that (because of the ageing of concrete) later strains are less than those that would be generated if the same stress change happened right after first loading [10,11]. The theory of linear creep is based upon the principle that time-dependent stress can be taken into account in creep calculations with the principle of superposition. In this step-by-step method, change in the constantly varying stress is divided into small increments. These increments can be superimposed considering their time of duration and the maturity of the

concrete. Using the principle of superposition, the strain of concrete at time t for small increments of stress can be computed with Equations (4) and (5) [9, 12, 13, 14, 15].

$$\varepsilon_c(t,t_0) = \sigma_0 \left(\frac{1}{E_c(t_0)} + \frac{\varphi(t,t_0)}{E_c(28)}\right) + \int_{\tau=t_0}^{t} \frac{\partial\sigma(\tau)}{\partial\tau} \cdot \left[\frac{1}{E_c(\tau)} + \frac{\varphi(t,\tau)}{E_c(28)}\right] d\tau + \varepsilon_s(t) \qquad (4)$$

$$\varepsilon_c(t,t_0) = \sigma_0 \left(\frac{1}{E_c(t_0)} + \frac{\varphi(t,t_0)}{E_c(28)}\right) + \sum_{i=1}^{n} \left(\frac{1}{E_c(t_i)} + \frac{[\varphi(t,t_i)]}{E_c(28)}\right) \Delta\sigma(t_i) + \varepsilon_s(t) \qquad (5)$$

It is difficult to find a solution to these equations because of the complicated mathematical form of the creep function. In 1967, Trost separated an ageing function from the creep function and developed a simpler equation to predict time-dependent stress-strain relation (Eq. (6)) [10, 16, 22].

$$\varepsilon_c(t,t_0) = \frac{\sigma_0}{E_c(t_0)} + \varphi(t,t_0)\frac{\sigma_0}{E_c(28)} + \frac{\sigma(t)-\sigma_0}{E_c(28)}\left(\frac{E_c(28)}{E_c(t_0)} + X\varphi(t,t_0)\right) + \varepsilon_s(t) \qquad (6)$$

This method, called the Age-Adjusted Effective Modulus Method (AAEMM), is based on superposition and the observation made by Trost that the variation of the ageing function is only minor after first loading [12, 17]. Because of that, the ageing function can be taken in simplified calculations as a time constant. This constant value is called ageing coefficient X, and it depends on creep coefficient, time of first loading and the load duration. Values and graphs of the ageing coefficient are presented in many references [11, 15, 18]. The ageing coefficient value varies between 0.5 and 1. When the time of loading is early, X is near 0.5, whereas the coefficient tends to be near 1 at later loading. Extensive investigations concerning the ageing coefficient value have been conducted, and according to a statement by Trost one can determine an ageing coefficient of $X = 0.8$ when the usual load carrying age t_0 is between 3 and 90 days and typical values of final creep coefficient are between 1 and 4 [15].

According to many researchers, this is the most accurate simplified method for analysing the time-dependent effects of concrete structures. There are errors in creep prediction models and in the linear model itself. Because of that, the gain in accuracy achieved by the more refined linear methods is often fictitious [11, 19, 20]. Similar to EMM, Trost's method is also based on elastic analysis with a modified elastic modulus called the age-adjusted modulus of elasticity (Eq. (7)).

$$E_{c,adj}(t,t_0) = \frac{E_{cm}(t_0)}{1+\frac{E_{cm}(t_0)}{E_{cm}}X\varphi(t,t_0)} \qquad (7)$$

Now Eq. (6) may be written in the following simple form [18]

$$\varepsilon_c(t,t_0) = \frac{\sigma_0}{E_{c,eff}(t,t_0)} + \frac{\sigma(t)-\sigma_0}{E_{c,adj}(t,t_0)} + \varepsilon_s(t) \qquad (8)$$

3.4 Restraint moment due to change in the static system

Creep and applied loads cause no time-dependent restraint moments in statically indeterminate structures that are homogenous and monolithically built. Structures deform but their internal forces do not change as long as the support conditions remain unchanged [11, 21].

When a simple-span structure is made continuous, the structure's restraint conditions are modified after the application of prestress force and self-weight of the structure. A modification of restraint conditions produces time-dependent variation of the initial elastic stresses and restraint reactions. Creep will tend to cause support reactions built up from staged construction to redistribute towards the support reactions that would have been produced if the structure had been constructed monolithically [22]. The effect of creep redistribution is illustrated in Fig. 1. Variance of the total moment is presented on the left hand side of the figure, while pure restraint moment is displayed on the right. In the upper part of Fig. 1, the effect of creep is illustrated for the dead load moments of two simple-span beams made continuous at time $t = t_0$.

1) At time $t = t_0$, the moment is distributed span-by-span and the moment is M_0 (continuous line)
2) If the structure was constructed monolithically the moment would be M_1 (dashed line)
3) When the structure is made continuous afterwards, the moment at time $t = \infty$ is something between moments M_0 and M_1 (dotted line)
4) In the time period $t_0 \dots \infty$ the moment varies in the hatched area
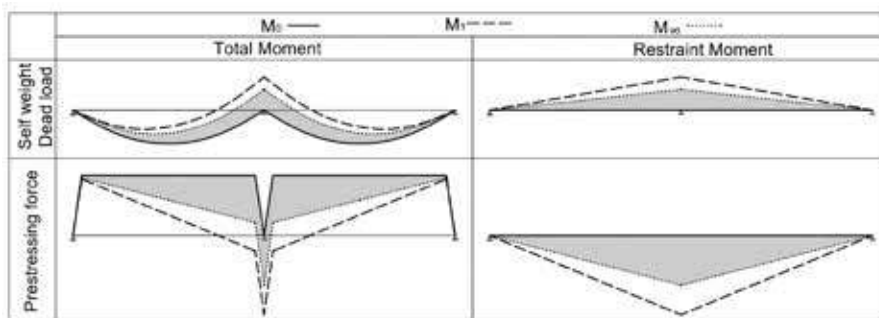

Figure 1 – Typical redistribution of self weight, dead load and prestressing force due to creep in a simple-span structure made continuous.

At the lower half of Fig 1, the same process is presented for the same structure's prestressing force. Prestressing force with constant eccentricity is applied to both beams separately at prefabrication factory. At time $t = t_0$, the simple-span prestressing moment is constant apart from the transmission lengths of the prestress force near the ends of the beam. If the prestressing force caused by a straight tendon layout would be adjusted to a two-span structure, the secondary moment of the prestress force would change the total moment M_0 to M_1. Again, when the static system is changed after the application of the prestress force, the final moment is somewhere between moments M_0 and M_1. How strongly the moment approaches the monolithically calculated value depends on the concrete's properties and the time when the girders are connected.

The equations presented in this paper are only theoretically exact for a linear creep law if the creep properties are the same in all cross-sections. In general, the error inherent in this assumption is small. In order for the linear creep law to be valid, concrete stress under quasi-permanent loads should not exceed $0.45 f_{ck}(t)$ [13].

Creep distribution effects at time t may be calculated for structures that undergo changes in a static system using Trost's AAEMM. The basic procedure is to calculate the distribution

moments before the support conditions are changed, and then recalculate the distribution of moments with all dead loads and prestressing force, assuming that the structure was constructed monolithically. The actual long-term redistribution moment for creep can then be found between these two moments, according to Eq. (9) [13, 14, 22].

$$S_t = S_0 + (S_c - S_0)\frac{E_c(t_c)}{E_c(t_0)}\frac{\varphi(t,t_0)-\varphi(t_c,t_0)}{1+X\varphi(t,t_c)} \qquad (9)$$

where
S_0 is the internal forces at the end of the construction process before support conditions are changed
S_c is the internal forces that are obtained if the structure is constructed monolithically
t_0 is the age of the application of the load
t_c is the age of the concrete when the support conditions are changed
$\varphi(t,t_0)$ is creep coefficient at time t for concrete age t_0 at time of first loading
$\varphi(t_c,t_0)$ is creep coefficient at time t_c for concrete age t_0 at time of first loading
$\varphi(t,t_c)$ is creep coefficient at time t for concrete age t_c at time of first loading

3.5   Restraint moment due to differential shrinkage

If bond between composite structures deck and beam part is sufficient, differential shrinkage causes deflection to the composite deck-girder system. For a continuous structure, deflection is prevented at the intermediate support, and this causes a negative restraint moment as indicated in Fig 2. EN 1992 does not include this phenomenon [6, 8].
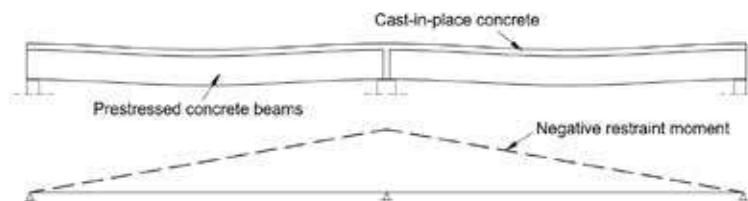

Figure 2 – Deformation and the resulting restraint moment due to differential shrinkage in a composite continuous structure.

In most of the methods used, the compressive internal force produced by the shrinkage difference between the slab and the girder is defined as

$$N_c = \Delta\varepsilon_{cs}A_d E_{cm} \qquad (10)$$

where,
$\Delta\varepsilon_{cs}$ is $\varepsilon_{csslab}(t) - (\varepsilon_{csbeam}(t) - \varepsilon_{csbeam}(t_0))$
$\varepsilon_{csslab}(t)$ is shrinkage strain in CIP slab at time t
$\varepsilon_{csbeam}(t)$ is shrinkage strain in prestressed member at time t
$\varepsilon_{csbeam}(t_0)$ is the shrinkage in prestressed member that has developed before casting the slab
A_d is cross-sectional area of CIP slab

E_{cm} is modulus of elasticity of CIP concrete

This compressive force causes constant moment M_{cs} to the cross-section

$$M_{cs} = N_c z_{cp} \tag{11}$$

where
z_{cp} is distance between mid-depth of CIP slab and centroid of the composite section

The restraint moment due to differential shrinkage depends strongly on the cross-sectional area of the deck slab A_d in Eq. (10). In bridge structures the girders are located near each other, and it is reasonable to presume that the effective width of the slab includes the entire distance between girders. In building structures, on the other hand, the beams are further away from each other, which might affect the cross-sectional area of the deck in Eq. (10). This matter is discussed in Sections 4.3 and 5.3. The amount of differential shrinkage also depends on girder age at continuity. If the girders are rather old, the strain difference between the slab and the girders is supposedly larger and negative restraint moment increases. On the other hand, if the girders are young when they are connected, the moment caused by differential shrinkage is smaller if the slab and the beam are assumed to shrink at the same rate.

Statically indeterminate internal moment S_{sh} caused by differential shrinkage in a perfectly elastic structure can be determined with the Force Method, for example. Secondary moments caused by differential shrinkage develop gradually with time. Because of that, they are reduced by creep. The actual statically indeterminate internal moment S_{sht}, at time t, including the relaxation due to creep, is then given by Eq. (12) [11].

$$S_{sht} = \frac{S_{sh}}{1 + X\varphi(t, t_0)} \tag{12}$$

where
t_0 is the time when the curing of the deck ended
X is the ageing coefficient which may be considered equal to 0.8 for long-term calculations

Data from various field tests indicate that the effects of differential shrinkage do not materialise. Therefore it is questionable if the methods used to analyse it are correct. It has even been proposed that differential shrinkage can be ignored in the design phase [3, 23].

3.6 Restraint moments in design

Restraint moments are generally taken into account in serviceability conditions. In some cases restraint moments may reduce the total moment of the structure. According to Ref. [3], restraint moments shall not be included in combinations in these situations. Consideration of the restraint moments can often be ignored at the ultimate limit state if there is sufficient rotation capacity available to shed the restraint moments [3, 22].

4. RESEARCH METHODS

4.1 Literature review

A literature review on the continuity of precast, prestressed concrete beams with CIP decks and time-dependent deformations of concrete was conducted. Literature published between 1961 and 2018 was collected and reviewed. The literature review was conducted for the purpose of finding methods of evaluating restraint moments in simple-span girders made continuous with CIP decks. The study also focused on exploring design specifications and standards of different areas concerning this topic. The overview of the literature review is presented in Chapter 3 of this article.

4.2 Experimental study

The goal of the experimental study was to explore the shrinkage and creep properties of conventional Finnish types of concrete used in precast, prestressed beams and CIP slabs. According to RILEM recommendations, creep and shrinkage strain measuring should be performed on cylinder specimens. In this study, it was decided that tests on beam samples would be carried out so that the results would be as analogous as possible to the studied structure. For the experimental programme, six rectangular ($300 \times 300 mm^2$) beams were tested for time-dependent strains. Two of the test beams, B1-sh and B1-cr, represent the composite structures beam part, and the remaining four test specimens, B2-sh, B2-cr, B3-sh and B3-cr, represent the slab part. Half of the test specimens are for creep measuring (cr) and the other half are for the shrinkage test (sh). For creep specimens, the sustained load was applied with concentrated prestressing force. Table 1 displays general data of the beams. Test specimens were stored in the laboratory for 3 to 6 months. Average temperature and relative humidity (standard deviation of observed data) at the laboratory during test was T = 22.5°C (s = 3.3°C) and RH = 34% (s = 12.4%).

Table 1 – General information of the shrinkage and creep test beams.

Beam Mark	Concrete Type	Prestressed or not	Length of specimen [mm]	Date of Casting
B1-sh	SCC (Mix-1)	NO	2,000	22/02/18
B1-cr	SCC (Mix-1)	YES	3,000	22/02/18
B2-sh	OC (Mix-2)	NO	2,000	15/05/18
B2-cr	OC (Mix-2)	YES	4,000	15/05/18
B3-sh	OC (Mix-3)	NO	2,000	12/06/18
B3-cr	OC (Mix-3)	YES	4,000	12/06/18

Concrete mixtures
Three mixtures were selected for the test in an attempt to simulate the type of Finnish concrete that is usually used in precast, prestressed element fabrication (Mix-1) and CIP deck-structures (Mixes 2 and 3). The mix proportions for the three mixtures tested are presented in Table 2. As mentioned in Section 3.1, SCC is the concrete type that is used most in Finnish precast, prestressed beams. For that reason, Mix 1 representing the composite structures beam part was selected to be SCC. The strength class of Mix 1 was C50/60. Mixes 2 and 3 were ordinary concrete, and the strength class for them was C35/45. Beams B2 and B3 were cast on different

days, and the concrete for them was ordered from a batching plant. Because of that the mixtures differ for test specimens B2 and B3.

Table 2 – Concrete mixture proportions

No. of Mix	W/C	W/B	Max Aggr. Size	Fine Aggr. < 6mm	Coarse Aggr. > 6mm	Water [kg/m³]	Cement [kg/m³]	Fly Ash [kg/m³]	Aggr. [kg/m³]	Air-Pro V5
Mix-1 (SCC)	0.418	0.366	12mm	63%	37%	177	423.5	59.6	1732.5	0%
Mix-2 (OC)	0.450	0.450	16mm	56%	44%	184.5	410	0	1692	0.03%
Mix-3 (OC)	0.393	0.393	16mm	55%	45%	171	436	0	1704	0.03%

In its plastic state, self-consolidating concrete has high flowability and good segregation resistance, and it doesn't require vibration. These special properties are attained by using admixtures and increasing the total quantity of fines in concrete. Greater fines content can be achieved by increasing the content of cementitious materials or integrating mineral fines. From Table 2, it can be seen that Mix-1 has higher paste volume, less coarse aggregate and a higher fine-coarse aggregate ratio than OC Mixes 2 and 3 [24].

Manufacturing and prestressing
Test beams B1-sh and B1-cr were produced in a prefabrication factory's prestressing bed. The strand pattern used for the B1 beams is shown in Fig. 3. The tensile stress in strands was 1400 MPa, and it caused uniform compression stress ($\sigma_c = 5.9$ MPa) to the cross-section after release. The tendon force was launched to the beams 12 hours after casting. The curing of the girders with a plastic foil shield was discontinued at the same time. For beam B1-sh all the strands were debonded along their length so that they stayed non-prestressed. Deponding was successfully verified with strain gauge measurements during prestress launching. The beams were transported to the laboratory of TUT on the same day they were prestressed.

Test beams B2-sh, B2-cr, B3-sh and B3-cr were cast in the laboratory. Prestressing was launched into the creep test beams by post-tensioning with the Dywidag strand technique. The tensile stress in strands was about 1250 MPa, hence it caused the same uniform compression stress to the cross-section after the slip at the anchorages as the prestress in test beam B1-cr. Reinforcement of the beams is shown in Fig 3. The beams were covered with plastic foil right after casting. The foil was removed after a week, which was assumed to be the conventional curing time for CIP slabs in site conditions. After the removal of the foils the creep test specimens were prestressed.
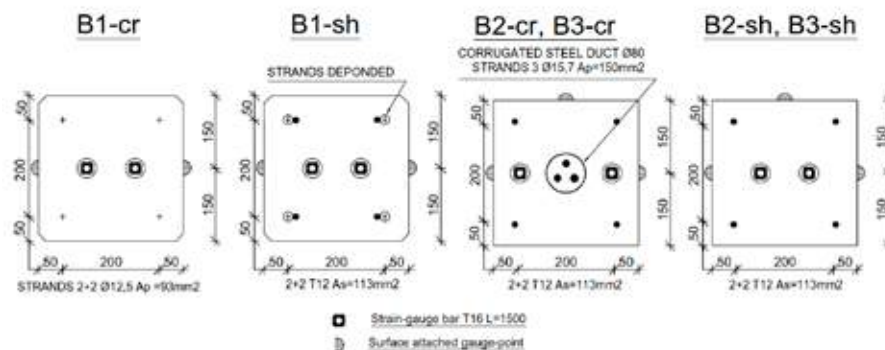
Figure 3 – Test beams' cross-section details and strain gauge locations.

Strain gauge and gauge-point measurements
The strain in test beams was measured with strain gauge bars. Each beam contained two strain gauge bars so that each specimen gave two independent sets of data. A strain gauge bar consists of a reinforcing bar (Ø16mm, $f_{yk} = 500$ MPa, L=1,500 mm), strain gauges, shielding materials and wires. In this arrangement the strain gauge exhibits the same deformation as the surrounding concrete. The deformation data were saved every second during prestressing and once an hour during the long-term tests that lasted from two to four months. In addition to strain gauge measurements, surface-attached gauge-point measurements were made in order to secure the validity of the strain gauge measurements.

Modulus of elasticity test
Cylinder specimens (d=150 mm, h=300 mm) were fabricated for each batch of concrete. The specimens were stored and cured next to the B1, B2 and B3 beams in order for their condition to be as similar as possible. The testing procedure of the SFS EN 12390-13 standard was applied to determine the stabilised elastic modulus of the specimens. The elastic moduli of concrete were measured at ages 7, 28, 90 and 180 days. In addition, the elastic deformation of beams B1-cr, B2-cr and B3-cr was measured in the prestressing phase with strain gauge bars. The modulus of elasticity at loading was then defined according to the measured elastic strain and known prestressing force [25].

4.3 Analytical study

An analytical tool has been developed to predict restraint moments according to equations presented in Chapter 3. The tool takes into account the creep and shrinkage effects, prestress losses, age at loading and the construction sequence. Prestress losses are calculated according to Eurocode equations. In the tool it is possible to use two different deformation properties. Elastic modulus, shrinkage and creep coefficient are assumed as being according to EN 1992-1-1 or experimental tests made in this study. In Chapter 5, the results are presented in an example structure with both deformation properties, and the results are compared.
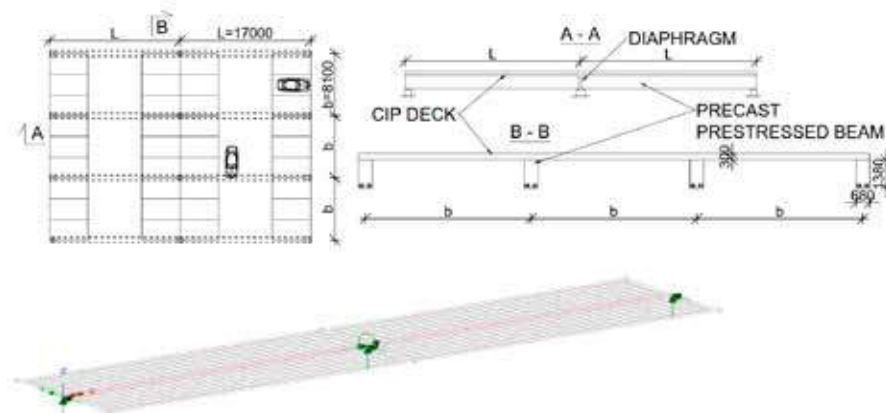
Figure 4 – Example parking deck structure and structural model from LUSAS.

In the analytical study, the example structure (Fig. 4) was a composite beam composed of rectangular beams (b×h = 0.68×1.38 m^2) and a CIP slab (h = 0.3 m). The distance between the beams was 8.1 m. Two simple-span beams (span length 17 m) were made continuous with the CIP slab. The prestressing force in the beam was 6 MN and eccentricity from the cross-section's soffit was 0.12 m. The ages of the girder when continuity was established were 7, 14, 28 and 90 days. Dimensions and other variables of the example structure were in accordance with a typical parking deck structure.

Shrinkage and creep experimental data ended at 90…130 days depending on the test sample. Future deformations are predicted, therefore restraint moments could have been determined for a more distant time. The principles used in the extrapolation are explained in Sections 5.1 and 5.2. The size difference between the studied structure and the test samples is taken into account with EN 1992-1-1 formulas (3.10), (B.3) and (B.7). In the experimental study, the beam concrete's creep coefficient is determined only for the case where the time of loading is 12 hours. In the analytical study, the beam's measured creep coefficients are also needed for loading ages of 7, 14, 28 and 90 days. These coefficient values are determined with the help of measured data from 12-hour loading and EN 1992-1-1 expression (B.5) [9].

Equations (9) and (12) are based on the assumption that there is only a single value for the structures' creep coefficient. In reality, the CIP deck and the beam have their own material properties. In the analytical tool, the beam's creep values are used for Equation (9) and the deck's creep coefficient for Equation (12) according to reference [21].

Effective width for differential shrinkage
Every reference document found about this theme used the slab's whole width to determine axial force produced by differential shrinkage. In building structures the beams are located relatively far from each other compared to bridges, and this should be taken into account in the cross-sectional area of the deck in Eq. (9). Computational check was made with the finite element analysis software LUSAS to determine composite structures' effective width for loads produced by differential shrinkage. The results of this study were implemented in the analytical tool [21,26].

5.   RESULTS AND DISCUSSION

5.1   Shrinkage and creep test results

Beam and deck shrinkage and creep strains were tested in the experimental phase of this study. The procedures and methods of measuring the strains have been presented in Section 4.2. The strain gauge and gauge-point measurements yielded congruent results for the B1 samples. A minor change in the preparation of strain gauge bars used in samples B2 and B3 caused inaccuracy to strain gauge measurements. This inaccuracy was improved by calibrating the strain gauge measurement values with parallel gauge-point measurements. For the sake of clarity, only strain gauge measurements are presented in this paper.

Figures 5 and 6 show the progress of shrinkage strains for the beam and deck concrete with the passage of time. The progress of both strains has been drawn according to EN 1992-1-1 and experimental data. The experimental data ends at three to four months. The logarithmic trend line is fitted to the experimental data to illustrate the mathematical form of measured shrinkage. The trend line formula and R-squared value, which describe the exactness of the model, are displayed in the chart. The shrinkage prediction beyond the test period is made according to test data and EN 1992-1-1 formulas (3.9) and (3.13).

The autogenous shrinkage can be distinguished from the total shrinkage for the measurements taken of the deck samples B2-sh and B3-sh, which were cured for a week. The shrinkage that happened during curing was assumed to be autogenous shrinkage. In beam sample B1-sh the curing duration was so short (12 hours) that autogenous shrinkage could not be discerned. When predicting beam shrinkage, the autogenous part of measured shrinkage has to be assumed to be in accordance with Eurocode.

From Fig. 5 it can be seen that the shrinkage strains measured from the sample made from Mix 1 (SCC) follow quite accurately the strains calculated according to Eurocode. On the other hand, the difference between measured strains and shrinkage, according to Eurocode for Mixes 2 and 3 (OC) presented in Fig. 6, is considerable. According to experimental data, shrinkage for conventional C35/45 deck concrete is about 40% less than Eurocode predicts. It can also be seen that two different deck shrinkage test samples yield very similar results, although the concrete mixtures were not exactly the same. This measured data exceeds the shrinkage variation ±30% defined in EN 1992-1-1 [2, 9].
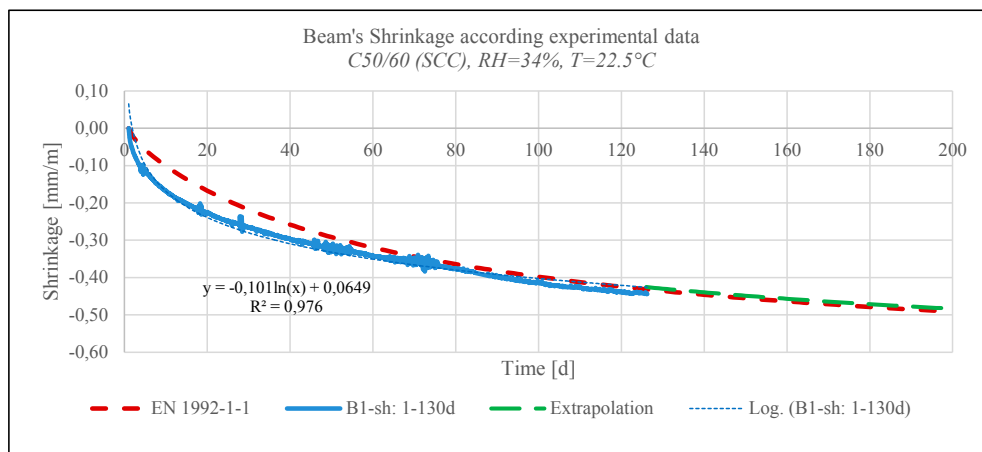
Figure 5 – Beam shrinkage according to experimental data (B1-sh) vs EN 1992-1-1.
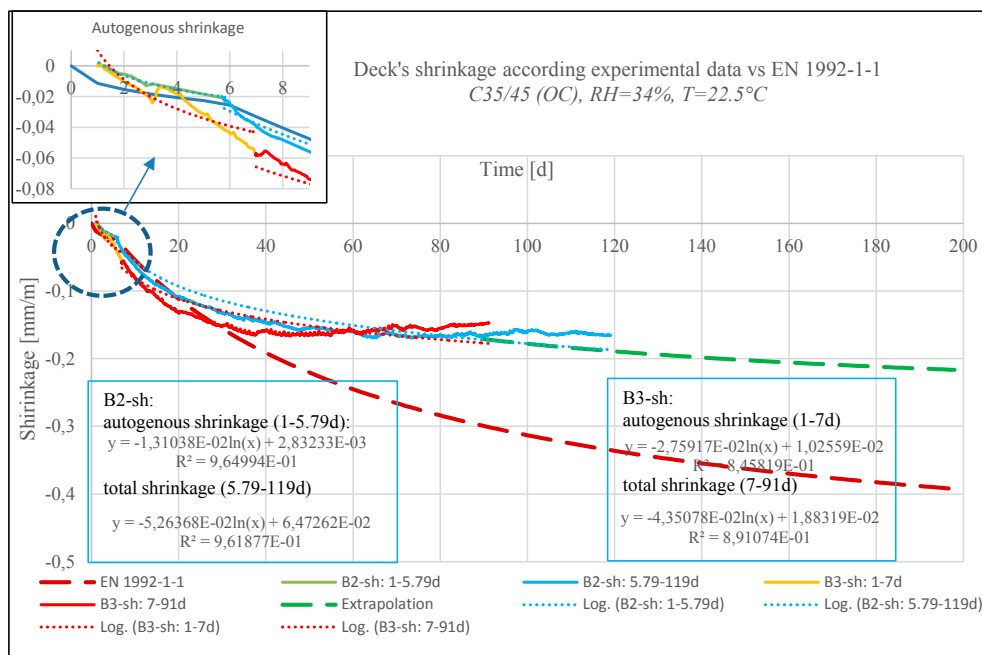

Figure 6 – Deck shrinkage according to experimental data (B2-sh, B3-sh) vs EN 1992-1-1.

Shrinkage values of different parts of the the cross-section are interesting in this study, because their difference causes restraint moments. It is generally understood that the precast beam in the composite concrete section has completed a significant part of its total shrinkage by the time the deck is cast, so the deck slab will shrink by a relatively greater amount and cause axial force and sagging moment into the composite section. This then causes negative restraint moments into the statically indeterminate structures. This happens if the beam and deck shrinkages are

supposed to develop according to Eurocode formulas. However, the results of the experimental study show that the deck OC's shrinkage is so minor compared to the beam SCC's shrinkage that differential shrinkage changes the sign and starts bending the structure upwards. This indicates that, with these concrete mixtures, differential shrinkage could cause positive restraint moments to the statically indeterminate composite structures instead of negative moments.

Figures 7 and 8 show the development of the creep coefficient for the beam and deck concrete. The development of both factors has been drawn according to EN 1992-1-1 and experimental data. The creep strain is obtained by subtracting the tested shrinkage strain (B1-sh, B2-sh and B3-sh) from the total strain measured from the creep specimens (B1-cr, B2-cr and B3-cr). Also, with the creep test the logarithmic trend line is fitted to the experimental data to illustrate the mathematical form of the measured creep coefficient factor. The creep growth prediction after the end of the data is made according to EN 1992-1-1 and formula (B.7) [9, 26].
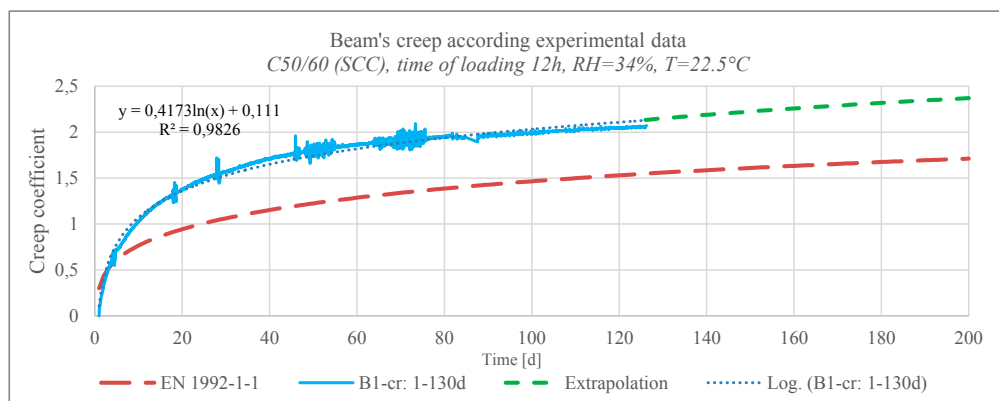

Figure 7 – Beam creep according to experimental data (B1-cr) vs EN 1992-1-1.
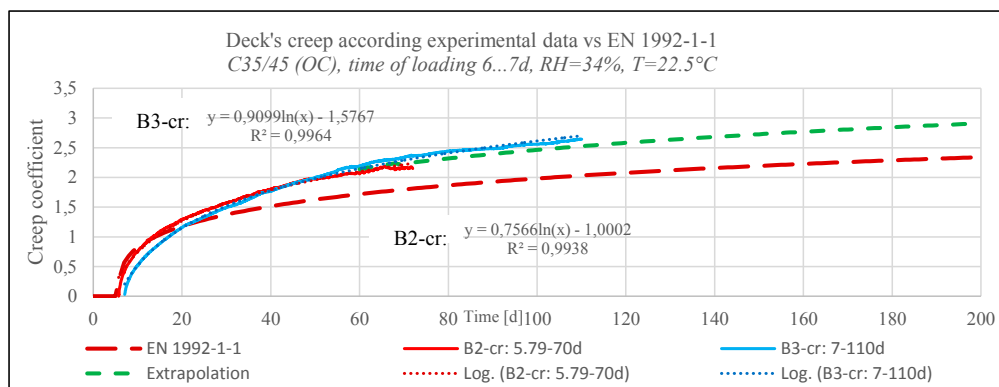

Figure 8 – Deck creep according to experimental data (B2-cr, B3-cr) vs EN 1992-1-1.

From Figure 7, it can be seen that the creep coefficient measured from the test beam made from SCC is about 40% higher compared to the creep coefficient calculated according to Eurocode. The result was anticipated, because many references state that SCC's high paste content causes higher creep deformations than that of OC of equal strength. This measured data exceeds the

creep variation ±20% defined in EN 1992-1-1 [2, 9]. Also the OC deck seems to creep more than Eurocode models would predict. Fig. 8 indicates that the creep strains of deck concrete test beams are about 20% higher than Eurocode models predict. Once again it is clear that two different deck creep test beams yield similar results, although the concrete mixtures were not exactly the same. When the beam's creep coefficient factor grows, the restraint moment for creep increases at the same time. Deck's higher creep factor increases the release of restraint moments caused by differential shrinkage.

The experimental test was conducted in the structural engineering laboratory in TUT, where relative humidity is quite dry (34%) compared to RH values commonly used in the design phase. This may cause a source of error to the conclusions made from this study. On the other hand, one main topic of interest in the study is the comparison of the properties of the two materials with each other. Such an experiment is also possible in a dry climate, because the condition is the same for both materials. The experimental test lasted three to four months, which is a short time compared to the structure's service life of 50-100 years. Then again, according to Eurocode a significant part (55-70%) of creep and shrinkage has developed during the testing period. Based on that, it is possible to make quite reliable models according to available data [9].

5.2 Modulus of elasticity test results

Figure 9 shows E_{cm} development for beam and deck concrete. In the plots it has been drawn both modulus according to EN 1992-1-1 and experimental tests. Measured compressive strength values are also added to the figure. It can be seen that the testing of both types of concrete has yielded lower elastic modulus values than EN 1992-1-1 would predict. The tests indicate that the elastic modulus of the concrete types was 10 to 15% lower compared to the Eurocode values. The beam concrete's measured data showed a growth in the elastic modulus with time, and it was possible to fit the logarithmic trend line to data points in the time period $t_0 ... 180d$. After that the beam's elastic modulus is assumed to be constant. The deck's test values had such a large variance that the modulus time dependence was selected to represent as a constant average after 7 days. Different elastic modulus time dependence and lower modulus values increase prestressing losses and affect restraint moments.
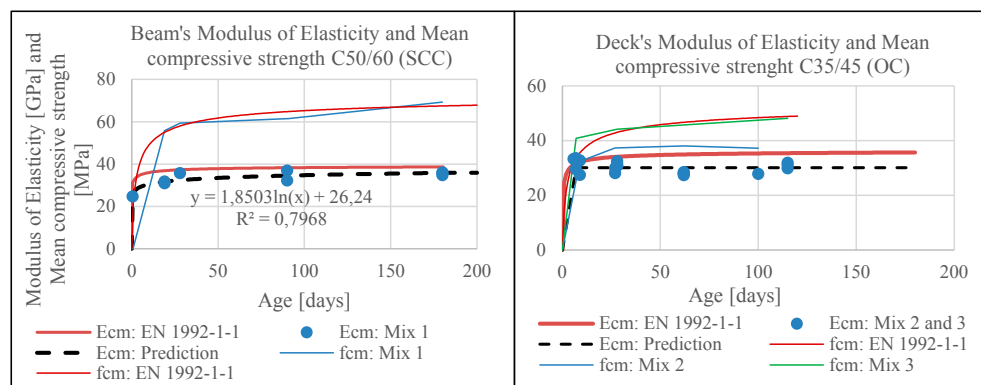

Figure 9 – Elastic modulus and mean compressive strength of tested concrete according to experimental data (Mix 1, 2 and 3) vs EN 1992-1-1

5.3 Effective width variation for differential shrinkage

Composite structures restraint forces produced by differential strains were determined with the finite element analysis software LUSAS. Forces calculated with LUSAS were compared to hand-calculated forces which were determined under the assumption that the width of the whole slab was effective in determining axial force. The effective width for differential shrinkage loading, determined according to the LUSAS analysis regarding the selected parking garage top deck structure, was 95% of the whole deck width. The amount or direction of the shrinkage load has no effect on the effective width. A noteworthy observation made from this simple study was that the usage of effective width of flanges determined with Eurocode formulas yields results that are clearly too small in this loading type.

5.4 Time-dependent restraint moments in example structure

Example structures' calculated restraint moments developed in time in the centre support with two different material models are plotted in Figure 10. Negative restraint moments produce tension to the diaphragm's top side, while positive restraint moments seek to crack the diaphragm's soffit.
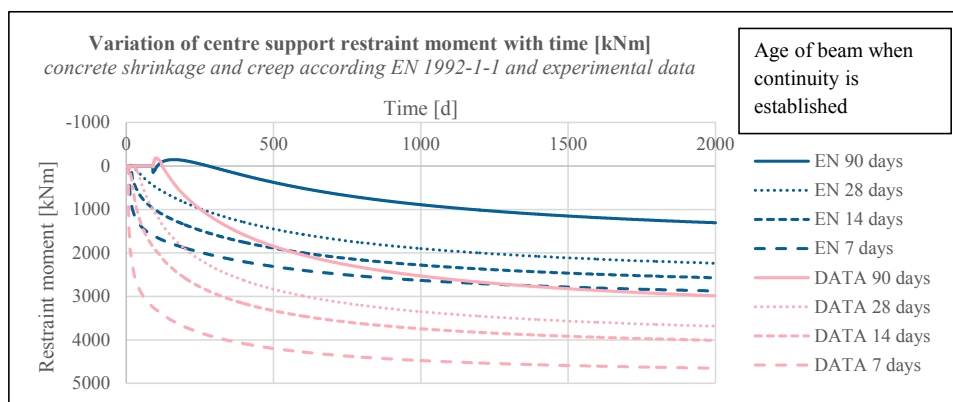

Figure 10 – Variation of example structures' (Fig. 4) centre support restraint moment with time according to EN 1992-1-1.

The blue lines in the figure represent restraint moments calculated with Eurocode material models. The shape of the Eurocode set of curves is similar to time-dependent restraint moment diaphragms presented in earlier studies made from this topic [13, 27]. If the age when continuity is established is young, the shrinkage difference between the slab and the beam is small and the negative moment produced by differential shrinkage is likewise small. In this case, the positive restraint moment grows the most. On the other hand, when the beam is older when connected for continuity, differential shrinkage plays a bigger role and the restraint moments are negative in the first year. In this case the final positive restraint moment remains smaller because differential shrinkage decreases it. For the selected example, the structure soffit's cracking moment is 1 375 kNm if the diaphragm is made from C35/45 concrete. According to the models

of EN 1992-1-1, it can be seen that restraint moments remain under this cracking moment for the first 2 000 days if the beams are 90 days old when connected.

The same analysis is presented for converted material properties with light red lines. In this analysis used shrinkage, creep and modulus of elasticity models are according to experimental data presented in Sections 5.1, 5.2 and 5.3. In the analysis, conducted according to tested material properties, positive restraint moments grow about two times bigger when converted to blue Eurocode curves. This difference results from the deck slab shrinkage test results. According to experimental data, deck shrinkage was so minor that beam shrinkage was more intense in comparison, despite the age of the beam when continuity was established being 90 days. This difference caused an unexpected result, according to which differential shrinkage also causes a positive restraint moment. With these deformation properties, both creep and differential shrinkage cause a positive restraint moment, and the resulting moments are considerably larger. In addition, beams' creep coefficient factor was 40% larger converted to the EN 1992-1-1 model. Beams' larger creep coefficient increases the restraint moments produced from the change in the static system

Field tests conducted by various researchers do not show the effects of differential shrinkage. It has been stated that the problem is not the structural model, because the model seems to give consistent results when evaluating restraint moments caused by temperature difference. It is believed that the problem might instead be the values used for deck shrinkage [3,28]. The experimental data gained from this research supports this claim. This observation is important, because if the differential shrinkage does not resist positive restraint moments as the models predict, the actual positive moments that develop may be worse than predicted.

In Ref. [3], creep and shrinkage restraint moments are allowed to taken to be zero if the girder's minimum age is at least 90 days when continuity is established. According to the analysis made in this study, restraint moments cannot be neglected in this studied example structure even if the minimum age of the precast girder would be extended to three months. This is because experimental data suggests that positive moments are not mitigated by the deck slab shrinkage in the way that the usual design models predict, and the structure is also different. However, as the analysis shows, the older the girder age is when continuity is established, the smaller the resulting restraint moments are.

6.   CONCLUSIONS

The experimental study showed a notable difference in the tested shrinkage and creep behaviour of selected concrete types compared to Eurocode prediction models. It also proved the need for an experimental study before evaluating restraint moments due to changes in the static system and differential shrinkage. The shrinkage strains measured were 0-40% less than expected and creep strains were 20-40% greater. The tested modulus of elasticity values were 10-15% lower compared to values used in the design.

Restraint moments were calculated with two different concrete deformation properties for the selected parking deck structure. In the example calculation, two simple-span composite beams were made continuous after a period of 7 to 90 days from the beam casting. The magnitude of one parking deck's restraint moments was resolved as a result of this study.

The analysis shows that positive restraint moments grow about two times greater, if tested material properties are used instead of Eurocode creep and shrinkage prediction models. Lager positive restraint moment values result mainly from shrinkage test results, which show that the direction of differential shrinkage restraint moments is opposite compared to the one that was expected. As a result creep and differential shrinkage, restraint moments are additive and the resulting total moment grows considerably.

No appearance of negative restraint moments is in agreement with prior studies, which claim that shrinkage values used computing restraint moments due to differential shrinkage are not correct. The calculation results of this study indicate how sensitive the restraint moments are to the creep and shrinkage models used. It seems that the inaccuracy of design methods for calculating restraint moments increases if the composition of the concrete types used for beam and deck structure differs considerably from each other. If the concrete types used were more similar, the direction of the restraint moments could be easier to predict.

This experimental study was conducted with merely two types of concrete and under one testing condition. In order to gain a more comprehensive understanding of the restraint moments of this kind of structure, more material testing is required. However, according to the results of this study it could be recommendable to accurately define a required concrete composition for the deck and the beam in the design phase so that creep and shrinkage could be better predicted. The use of SCC in the precast beam should be considered in detail. The advanced age of the girder when establishing continuity seems to also have an effect on minimising the restraint moment.

These conclusions have been made according to measurements which have taken three to four months. Long-term measurements of test samples will be continued and more SCC test samples are going to be studied in order to gain more data. The next phase of this study is the evaluation of the effect of restraint moments on the building structure's continuity. Analytical study and physical testing will be conducted to determine the potential of simple-span prestressed beams made continuous in building structures.

Measured shrinkages for deck concrete mixtures 2 and 3 were surprisingly low. Further investigation on these concrete mixes should be made to clarify the reason for small shrinkage test results. The findings of experimental tests made on SCC beams indicate that the creep coefficient is bigger and early age modulus of elasticity smaller than the used design specifications predict. SCC is a widely used material in Finnish prestressed concrete fabrication, but its use isn't taken into account in any way at the design phase. More testing and analysis of SCC's usage in prestressed concrete beams is needed.

REFERENCES

1. Finnish Concrete Society: "Concrete Textbook 2018, by201," Vaasa, Finland, 2018, 568 pp. (In Finnish).
2. International Federation for Structural Concrete (fib): "CEB-FIP, Model Code 2010," Final draft, Volume 1, *Bulletin* 65, Switzerland, 2012, 357 pp.
3. American Association of State Highway and Transportation Officials: "AASHTO LRFD Bridge Design Specifications, Customary U.S. Units," Section 5, "Concrete Structures," Washington DC, USA, 2012, 332-589 pp.

4. Miller R A, Castrodale R, Mirmiran A & Hastak M: "NCHRP Report 519, Connection of Simple Span Precast Concrete Girders for Continuity," *Transportation Research Board*, Washington DC, 2004, 202 pp.

5. Abdalla O A, Ramirez J A & Lee R H, "Strand Deponding in Pretensioned Beams – Precast Prestressed Concrete Bridge Girders with Deponded Strands, Continuity Issues," Purdue University, West Lafayette, Indiana, USA, 1993, 265 pp.

6. McDonagh M D & Hinkley K B, "Resolving Restraint Moments: Designing for Continuity in Prestressed Concrete Girder Bridges," *PCI Journal*, July-August 2003, 16 pp.

7. Freyermuth C L: "Design of Continuous Highway Bridges with Precast, Prestressed Concrete Girders," *PCI Journal,* April 1969, pp. 14-39.

8. Meyerson R, Weyers R E, Via C E, Mokarem D W & Lane D S: "Evaluation of Models for Predicting (Total) Creep of Prestressed Concrete Mixtures," Virginia, USA, 2002, 55 pp.

9. "EN 1992-1-1, Eurocode 2: Design of Concrete Structures. Part 1-1: General rules for buildings," Brussels, Belgium, 2004.

10. Bazant Z: "Mathematical Modeling of Creep and Shrinkage of Concrete," Chapter 3, "Creep Analysis of Structures," Chichester, New York, Brisbane, Toronto, Singapore, 1988, pp. 217-273.

11. ACI Committee 209: "Publication SP-76, Design for Creep & Shrinkage on Concrete Structures," Chapter SP76-10, "Prediction of Creep, Shrinkage and Temperature Effects in Concrete Structures", Detroit, USA, 1982, pp. 193-300.

12. Menn C: "Prestressed Concrete Bridges", Basel, Boston, Berlin, 1990, 546 pp.

13. "EN 1992-2, Eurocode 2: Design of Concrete Structures. Concrete Bridges. Design and Detailing Rules," Brussels, Belgium, 2005.

14. "EN 1992-2:2005/AC, Eurocode 2: Design of concrete structures. Concrete bridges. Design and Detailing Rules," Brussels, Belgium, 2008.

15. Trost H: "Creep, Relaxation and Shrinkage of Structural Concrete," *IABSE reports*, Switzerland, 1991, Vol. 62, pp. 59-76.

16. Trost H: "Auswirkungen des Superpositionsprinzips auf Kriech- und Relaxationsprobleme bei Beton und Spannbeton," *Beton- und Stahlbetonbau* (Berlin – Wilmersdorf), No. 10, 1967, pp. 230-238 (in German).

17. Bazant Z: "Prediction of Concrete Creep Effects Using Age-Adjusted Effective Modulus Method," *Journal of the American Concrete Institute*, Vol 69, 1972, p.p 212-217

18. CEB: "Structural Effects of Time-Dependent Behaviour of Concrete," *Bulletin* No. 215, Lausanne, Switzerland, 1993, 308 pp.

19. Keitel H: "Selecting an Advanced Creep Model or a Sophisticated Time-Integration? A new Approach by means of Sensitivity Analysis," *International Journal of Mathematical and Computational Sciences*, Vol. 6, No. 7, 2012, pp. 724-731

20. International Federation for Structural Concrete (fib): "CEB-FIP, Model Code 2010," Final draft, Volume 2, *Bulletin* 66, Lausanne, Switzerland, 2012, 377 pp.

21. Tadros M K, Girgis M A, Tuan C Y & Alex A A: "Simplified Design for Positive Restraint Continuity Moment in Bridge Girders." *PCI Journal*, July-August 2018, pp. 62-78.

22. Hendy C R & Smith D A: "Designer's Guide to EN 1992-2, Eurocode 2: Design of Concrete Structures. Part 2: Concrete Bridges," London, UK, 2007, 196 pp.

23. ACI Committee 209: "Publication SP-76, Design for Creep & Shrinkage on Concrete Structures," Chapter SP76-13, "A Simple Method to Analyse Time-Dependent Forces Developed in Continous Concrete Structures" Detroit, USA, 1982, pp. 325-339

24. Betonikeskus Ry: "SCC – Self Consolidating Concrete," Loviisa, Finland, 2004. (In Finnish).
25. "EN 12390-13, Testing Hardened Concrete, Part 13: Determination of Secant Modulus of Elasticity in Compression," 2013.
26. Tia M, Liu Y & Brown D: "Modulus of Elasticity, Creep and Shrinkage of Concrete," University of Florida, USA, 2005, 185 pp.
27. Mattock A H:"Precast-prestressed concrete bridges 5, Creep and Shrinkage studies," *Journal of the PCA Recearch Laboratories*, Vol 2, No. 2, 1961, pp. 32-66.
28. Mirmiran A, Kulkarni S, Castrodale R, Miller R & Hastak M: "Nonlinear Continuity Analysis of Precast, Prestressed Concrete Girders with Cast-in-Place Decks and Diaphragms," *PCI Journal*, September-October 2001, pp. 60-80.
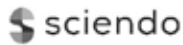
Influence of Cracking on Effects of Restrained Deformations in a Post-tensioned Concrete Bridge

Kimmo Jalonen, M. Sc.
Graduate researcher, Tampere University of Technology
Department of Civil Engineering
Korkeakoulunkatu 10, 33101, Tampere, Finland
k.k.jalonen@gmail.com

Joonas Tulonen, M. Sc.
Post-graduate researcher, Tampere University of Technology
Department of Civil Engineering
Korkeakoulunkatu 10, 33101, Tampere, Finland
joonas.tulonen@tut.fi

Anssi Laaksonen, Dr. Tech.
Professor, Tampere University of Technology
Department of Civil Engineering
Korkeakoulunkatu 10, 33101, Tampere, Finland
anssi.laaksonen@tut.fi

ABSTRACT

Imposed and restrained deformations cause stresses in continuous concrete bridges, and in analyses of the superstructure these stresses are usually reduced to some degree due to creep and cracking of concrete. This study examines cracking and redistribution of stresses in a bridge superstructure under the loads and load combinations used in the original bridge design. The subject of this study is a three-span post-tensioned continuous concrete cantilever beam bridge. The bridge was analysed with non-linear calculation utilising the general force method and

moment-curvature relationships. The analysis yielded the bending stiffness of the post-tensioned bridge superstructure as a function of bridge length under different loads. It was discovered that the secondary moment from prestressing force increased as the bending stiffness of the central span decreased due to cracking under external loads, which is not normally considered in design. The bending moment effects of linear temperature difference and support settlement decreased as expected as the superstructure bending stiffness decreased. The analysis provided new information on the effects of secondary moment from the prestressing force and on the difference between the cracked state and the linear elastic analysis of the concrete bridge superstructure.

Keywords: restrained deformations, concrete cracking, post-tensioned concrete, bridge

1. INTRODUCTION

The magnitude of the stresses from imposed and restrained deformations (later restrained deformations) depends on the bending stiffness of the superstructure, so it is clear that the stress level changes when the concrete superstructure cracks. This study considers cracking as the main factor affecting structural bending stiffness. The Finnish Transport Agency has an application guideline of the Eurocode [4] for determining the effect of cracking and creep on restrained deformations in bridge designs. In the corresponding Eurocode, EN 1992-2 [10], it is not instructed how the effects of cracking and creep on restrained deformations in bridge design should be considered. It has been found that a more detailed investigation of the subject is required in order to obtain certainty as to how much stresses from restrained deformations could be reduced in the design of a structure. In this article, a post-tensioned continuous beam bridge is examined, and further studies on a continuous reinforced beam bridge can be found in a master's dissertation [2] written on the topic.

Approximately 530 post-tensioned concrete bridges were built in Finland from 1970 to 1990. These bridges are now reaching an age when they need to undergo their first major renovations and repairs. The increase in vehicle loads has been substantial during their lifespan, so much so that the maximum vehicle is now 72 tonnes. More accurate calculations are needed in assessing the bearing capacity of bridges in order to avoid costly and unnecessary bridge strengthening operations. The results can also be utilised in the design of new bridges to produce better performing and more cost-effective structures. [2]

Generally, in bridge design, stresses from thermal loads and support settlement can be ignored in the ultimate limit state design of a reinforced concrete beam bridge, provided that critical structural components have sufficient rotation capacity. [3,4] Restrained deformation loads have to be included in the serviceability limit state design, but these can be sometimes reduced. The creep coefficient is used to calculate the extent to which the deformation loads of the elastic state are to be taken into account in designing a new bridge. The results of this study have been compared with the permitted reductions given in the Finnish Transport Agency's guidelines. [2]

2.   ANALYSIS

2.1   The bridge

The selection of the post-tensioned bridge for this study was made in consideration of the general properties of all built bridges. A significant portion of the prestressed bridges in Finland have three spans. A bridge built in 2015 was selected for this study. The bridge is a post-tensioned continuous cantilever beam integral bridge. The bridge's prestressing steel is inside metal sheet ducts that are injected with cement grout. The horizontal and vertical geometry of the bridge is curved.

The studied bridge was chosen so that it would represent ordinary Finnish prestressed concrete bridges designed and built in the 21st century. The original bridge was designed in accordance with the Eurocodes and the Finnish guidelines for Eurocodes, [3,4] which are non-contradictory information that complement the Eurocodes. The choice to use an "ordinary" bridge was done so as to limit the amount of needed calculations, since comprehensive parametrisation of the calculation model was not conducted.

For this study, the geometry of the bridge was simplified in order to enable two-dimensional calculations by the general force method while utilising the symmetry of the superstructure. The bridge is assumed to be straight without end cantilevers in calculations (Figure 5) since it is difficult to take soil stresses into account in calculations based on the general force method. The span lengths of the bridge were 24.97 m + 31.17 m +24.97 m. Figure 1 shows the cross-sections of the bridge where effective width of the deck slab has been taken into account. The reinforcement bars and prestressing steel cables taken into account in the calculations are also shown.
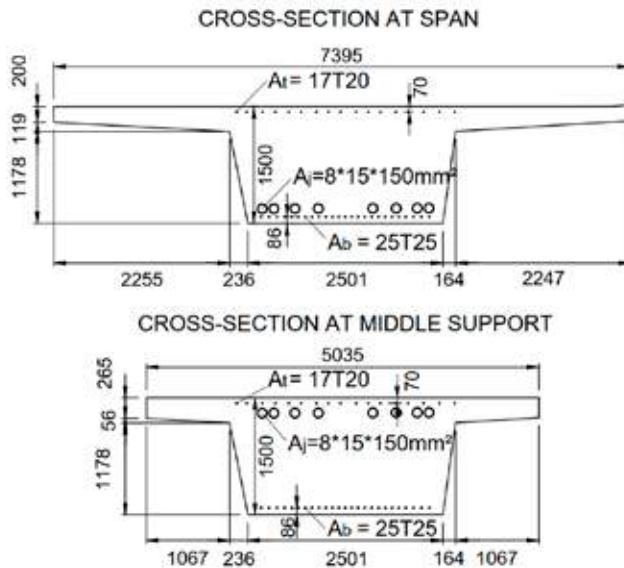

Figure 1 – Effective cross-section at spans and at middle supports.

2.2   Calculation steps

The analysis of the bridge is conducted with the following steps:

1. Moment-curvature relationships for bridge beam cross-sections are calculated
2. Calculation of the superstructure bending stiffness under all permanent and transient loads
3. Calculation of bending moments from linear temperature difference and secondary effects of prestressing force using calculated bending stiffness from step 2
4. Calculation of bending moments in a linear elastic situation, as would be done in design
5. Comparison of bending moments from non-linear and linear analyses

In the calculations of the moment-curvature relationships, it was assumed that planes remained plane and that the calculations were conducted with the actual geometries of the cross-sections, taking into account the effective widths of the flange. The effective widths of the cross-sections were determined according to SFS-EN 1992-1-1 [7].

49 moment-curvature relationships of cross-sections were calculated, with different reinforcement ratios and the location of the prestressing steel varying according to the bridge design drawings. Using moment-curvature relationships, it is possible to take into account e.g. flexural stiffness in a cracked and uncracked state with different load levels, complex cross-section shapes, non-linear material behaviour, etc. that have an influence on bending stiffness of the studied bridge superstructure. Furthermore, the moment-curvature relationship also contains information of the different material properties, the position and amount of steel and prestressing steel in a cross-section, cross-section dimensions and prestressing force. The material models used are from Eurocode SFS-EN 1992-1-1 and are presented in more detail in Section 2.4 [2].

Moment-curvatures are used as initial data in the analysis of the whole superstructure. The bending stiffness of every cross-section in a load-bearing superstructure can be calculated with moment-curvatures (Eq. 1) when the bending moment distribution of a superstructure has been calculated. In the first iteration of bending moment calculation, it is assumed that superstructure behaviour is linear elastic. After the bending moments have been calculated, the bending stiffness is recalculated and a second iteration is made. If the bending moments in middle supports are different than in the previous iteration, a new iteration will be made with a recalculated bending stiffness. This iteration will continue until the average moment of both middle supports is equal in subsequent iterations. The end of the iteration loop means that loads and bending stiffness are in equilibrium. Load-stiffness equilibriums are calculated with many live load positions and load history combinations in order to determine the most adverse bending stiffness degradation of the superstructure during its lifetime.

$$EI = \frac{M}{v''} \qquad\qquad\qquad (1)$$

In this study the following loads have been used: dead loads, traffic loads, support settlement and linear temperature difference, as well as the tendon force and its secondary moment. The traffic load has been modelled with a more realistic vehicle shown in Figure 3 instead of the SFS-EN 1991-2 Load Model 1 (later LM1) [8] used in the original design of the bridge. The loads from the vehicle have been scaled so that the bending moments on this bridge would be approximately equal to those caused by LM1.

Bending moments from loads are calculated using the general force method [1]. The method allows arbitrary bending stiffness to be used anywhere in the superstructure. For instance, the general force method can be used in the analysis of a simple two-span beam with a uniform load and arbitrary bending stiffness, as shown in the following equations and in Figure 2.

$$a(x) = \int_0^L \frac{\bar{M}_1(x)^2}{EI(x)} dx \tag{2}$$

$$u(x) = \int_0^L \frac{M_0(x) * M_1(x)}{EI(x)} dx \tag{3}$$

$$X(x) = \frac{-u(x)}{a(x)} \tag{4}$$

$$M_t(x) = M_0(x) + X(x) * M_1(x) \tag{5}$$
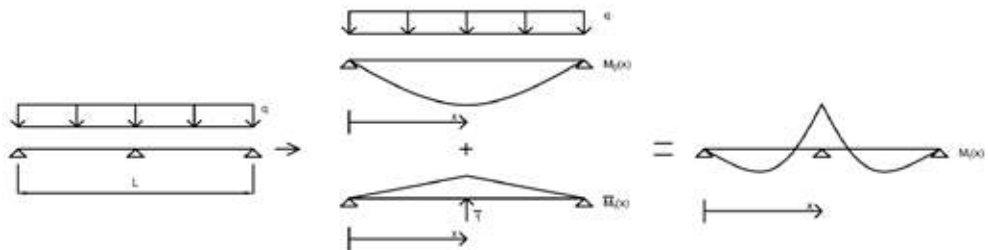
Figure 2 – Calculating the bending moment of a two-span continuous beam.

2.3 Loads

The loads and load combinations in this study were ones that are usually used in bridge design in Finland [3]. The loads in Finnish national guidelines [3,4] are based on Eurocode 1, while load combinations are based on Eurocode SFS-EN 1990 [9], though some of the recommended combination values have been modified nationally. Either traffic load or thermal load was chosen as the leading action in load combination. The structure was analysed with both serviceability limit state and ultimate limit state load combinations. In this study, only the results from the serviceability limit state are presented. The serviceability limit state quasi-permanent combination was also used to examine the effects of creep. Short-term and long-term prestress force losses were also taken into account. Serviceability limit state load combinations and load factors are shown in Table 1.

Support settlement was not present in the first calculation step, and for the second calculation step it was taken into account with factor 1.0. All other loads were included in every calculation step. Prestress force includes primary bending moment and secondary bending moment.

Table 1 – Serviceability state load combinations and combination factors [3].

Leading action	Characteristic combination (CHAR)	
	TEMPERATURE	TRAFFIC
Dead load	1.0	1.0
Tendon force	1.0	1.0
Support settlement	0/1.0	0/1.0
Linear temperature difference	1.0	0.6
Traffic load, UDL	0.4	1.0
Traffic load, TS	0.75	1.0

The vehicle load was modelled by vehicle AA 13/76 (Figure 3) [5], which is a vehicle determined for bridge assessment that corresponds to the largest truck allowed in public roads, to make the traffic load correspond more closely to actual vehicles than the LM1 that is used in design. The LM1 is by definition a design load model, and it was seen that the bending moment envelope along the bridge length would be more realistic with load model AA 13/76 used in the bridge assessment, since it is based on actual axle configurations of real vehicles. Peak moments from basic load model AA 13/76 are different from those of LM1, and this research takes design stresses of the structure into account, so the axle weights in load model AA 13/76 were scaled with scale factors so that the peak bending moments would match.

On the studied bridge were two road lanes, and two AA 13/76 vehicles were placed on both lanes. On one lane, the distance between the vehicles was set equal to the length of the side span. The vehicles on both lanes were driven simultaneously across the bridge. The stress induced by the vehicles was scaled so that it would be equally high as the impact of LM1 at the intermediate supports and mid-span. The calculated factors were different for maximum bending moment at the intermediate supports and the central span. The smallest factor was used in the calculations, for it does not overestimate the cracking of the structure. The impact of the LM1 varied depending on the used combination factors for combining the uniformly distributed load (UDL) for LM1 and the tandem system for LM1, as shown in Table 1.

When linear temperature difference was the leading action, the used scale factor was 0.92, and for traffic load leading action the used scale factor was 1.60. The linear structural model was used to determine the most critical traffic load positions, which were varied by ±4 metres in actual non-linear calculations. It was necessary to have variation of the traffic load positions because the calculations were non-linear, as well as to ensure that the maximum effect of the traffic load was uncovered.
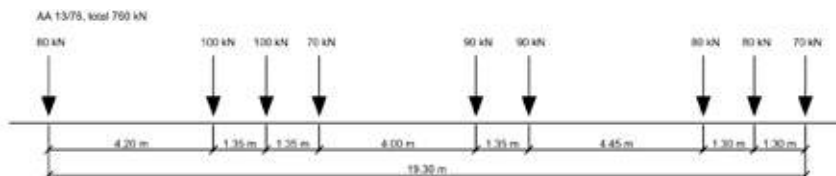
Figure 3 – Vehicle load model [5] used to calculate traffic load.

Support settlement and linear temperature difference were determined according to Finnish national guidelines [3]. Support settlement was 10 mm in each pier. Linear temperature

difference between the bottom and top of the structure was 9.9°C when the top of the structure was warmer and 8°C when the bottom of the structure was warmer. Calculation of the reduced values of linear temperature difference has been made according to Eurocode 1991-1-5 Table 6.1 and Table 6.2 according to the thickness of the bridge surface layer (110 mm). Tables 6.1 and 6.2 in Eurocode 1991-1-5 are the same in the Finnish national guidelines [3].

2.4   Materials

Material properties for reinforcing steel, prestressing steel and concrete specified in SFS-EN 1992-1-1 were used: for concrete Figure 3.3 in Ref. [7], for reinforcing steel Figure 3.8 3 in Ref. [7] and for prestressing steel Figure 3.9 3 in Ref. [7]. The bilinear stress-strain relationship was used to represent the behaviour of reinforcement and prestressing steel while the parabola-rectangle model was used for the concrete. No strain hardening of either prestressing steel or reinforcement was considered. Plastic elongation of reinforcement or prestressing steels was not limited when determining moment-curvature relationships of cross-sections. Table 2 shows the material strength and initial Young's modulus for each material used in the calculations. Characteristic material properties were used because they are typically used in designing the bridge in a serviceability limit state.

To take into account the change in tendon geometry and effective width of top flange, the moment-curvature relationships were calculated at several points in the beam's length. Figure 4 shows the moment-curvature relationship of the superstructure at the centre of the mid-span and at the intermediate support. Moment-curvature relationships of cross-sections were used to represent differing beam lengths of 0.3 m to 1.2 m. The centre of gravity of tendons and mean prestressing force were used in each cross-section. The location and amount of reinforcing steel, which are shown in Figure 1, remained unchanged for all calculated cross-sections.

The y-axes of the calculated moment-curvatures were modified so that the moment-curvature relationship would pass through point (0,0) of the graph. This shift was done because primary moment from prestress was already included as load in the calculation of total bending moment. Therefore, the magnitude of the shift was approximately the same as the primary moment from prestress. Figure 4 shows the calculated and shifted moment-curvature relationship at the centre of the mid-span and at the middle span.

Creep was not considered in the calculation of the moment-curvature relationships. Long-term loss of prestress force was assumed to be 15%.

Table 2 – Material properties.

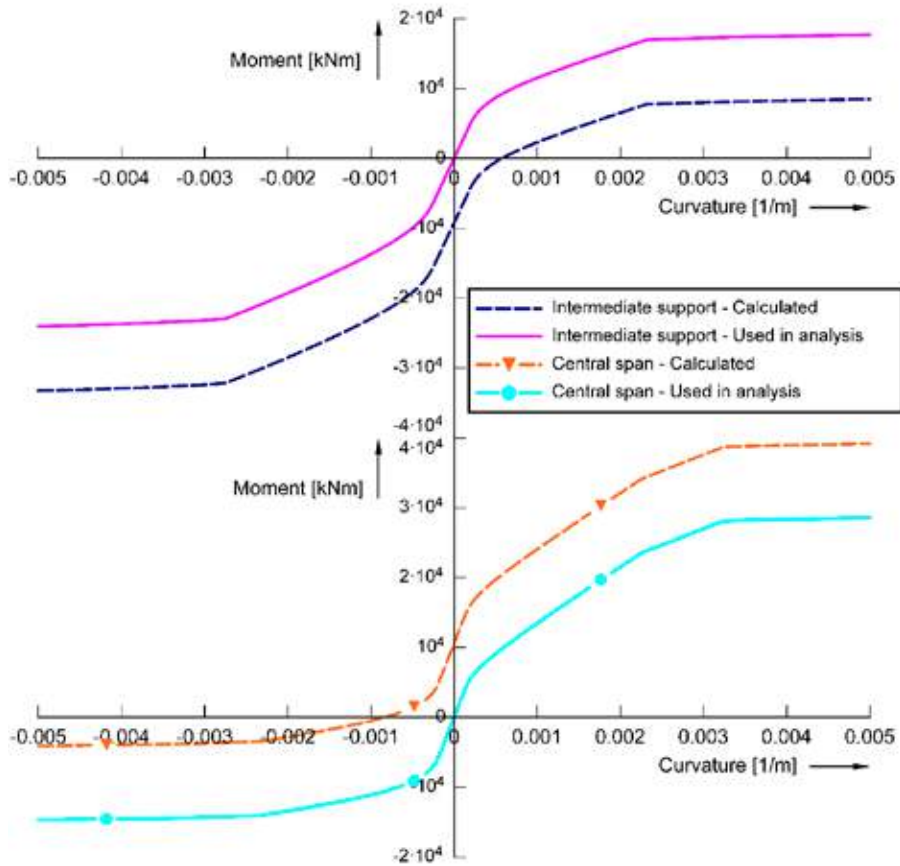|			Materials		
	Concrete		Reinforcement steel		Prestressing steel
f_{ck} [MPa]	35	f_{yk} [MPa]	500	f_{pk} [MPa]	1600
E_{cm} [GPa]	34	E_s [GPa]	200	E_p [GPa]	195
γ_c	1.35	γ_s	1.1	γ_p	1.1

Figure 4 – Example of moment-curvature relationship at the middle of the central span and at the intermediate support.

2.5 Structural model

The bridge was modelled as a straight, continuous three-span beam bridge (Figure 5). In reality, the bridge was attached rigidly to all piers, but this was ignored in the model since the columns were slender. The calculation was further simplified by eliminating the end cantilevers from the model and adjusting the side spans to take advantage of symmetry. Because the cantilevers were eliminated from the beam model, bending moments representing the dead weight of the bridge ends were added to the ends of the beam model (Figure 5). Figure 6 shows the tendon geometry and prestress force used in the calculation.
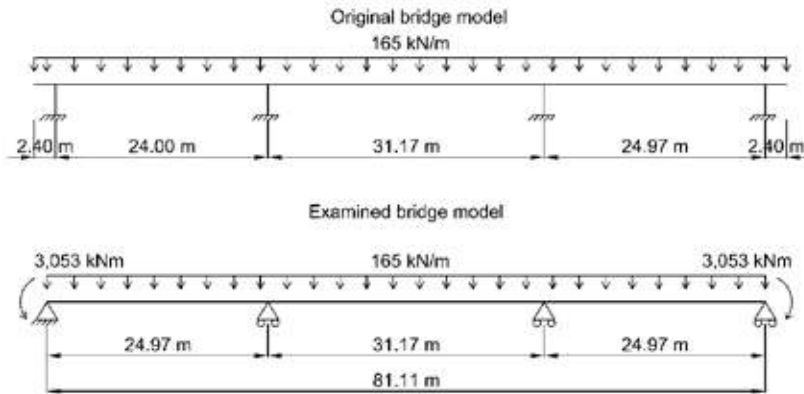
Figure 5 – Actual bridge geometry and geometry in the model.
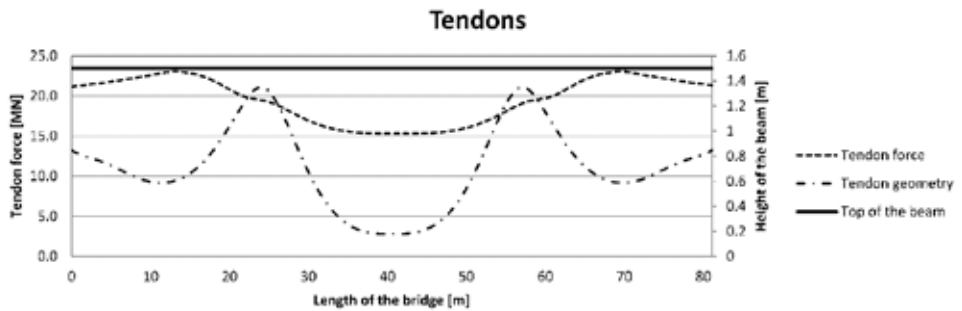
Figure 6 – Tendon geometry and prestress force used in the calculation.

The bending moment from the prestressing on the superstructure was calculated from Eq. 6

$$M_p = M_p^{(0)} + M_p', \tag{6}$$

where $M_p^{(0)}$ is the primary bending moment from the prestress force and M_p' is the secondary moment induced by restraining the primary deformations from prestress. The primary moment from the prestress force was derived from Eq. 7

$$M_p^{(0)}(x) = P(x) * e(x), \tag{7}$$

where $P(x)$ is prestress force and $e(x)$ is the distance of the tendon from the centroid of the cross-section.

3.   RESULTS

After each iteration, step calculations yielded residual bending stiffness of the bridge as a function of bridge length. Figure 7 shows residual bending stiffness as a function of bridge length in the characteristic combination where the traffic load was the leading action. Figure 7 shows that the largest change in the bending stiffness of the superstructure was at the middle of the central span.

The bending stiffness of the superstructure did not decrease compared to the initial situation at the intermediate supports or the side spans. The slight difference in the bending stiffness of the bridge superstructure between the elastic state and the characteristic combination resulted from the calculations of the moment-curvature relationship with non-linear materials. In a typical structural analysis of a bridge in its design state (linear elastic model with homogenous cross-section), the elastic bending stiffness does not include the effects of the reinforcement or the prestressing steel. Also, the stress-strain relationship of the concrete was different in the elastic state. These differences caused calculated bending stiffness to be slightly larger compared to the elastic state. Bending stiffness in the elastic state is shown for comparison, and the conclusions of the research are drawn from the analysis where change in bending stiffness is calculated with moment-curvature relationships.
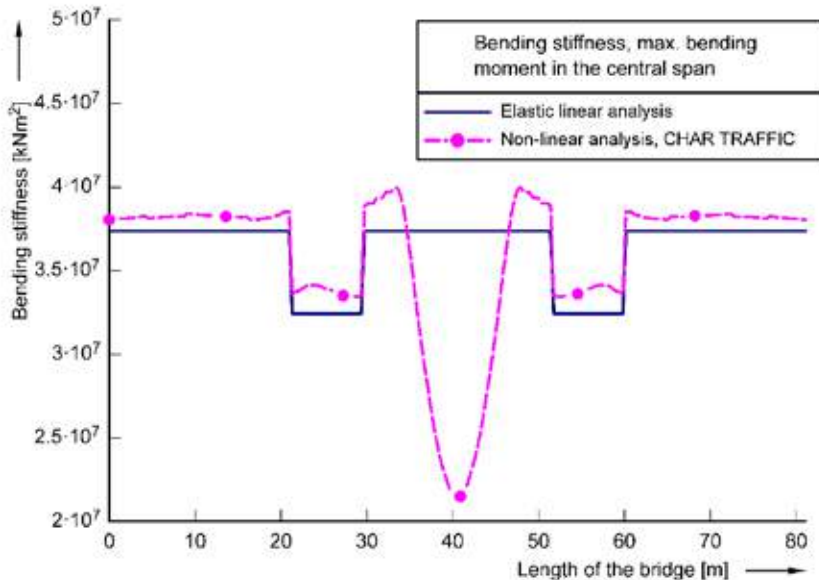

Figure 7 – Calculated bending stiffness and bending stiffness in an elastic state.

Decreasing the bending stiffness of the superstructure changed the bending moment distribution along the bridge length. Because the bending stiffness changed at the central span, the bending moments from external loads increased at intermediate supports and decreased at the central span. Bending moment redistribution was not significant at the side spans. Figure 8 shows the magnitude of the bending moments from external loads in characteristic combination.

Bending moments from support settlement and linear temperature difference decreased only slightly in the characteristic combination, while traffic load was the leading action as shown in Figure 9. The secondary moment from prestressing force increased by 0.5 MNm as the bending stiffness of the central span decreased more than in the rest of the superstructure. The combined effect of all restrained deformations was therefore larger than in the elastic state.
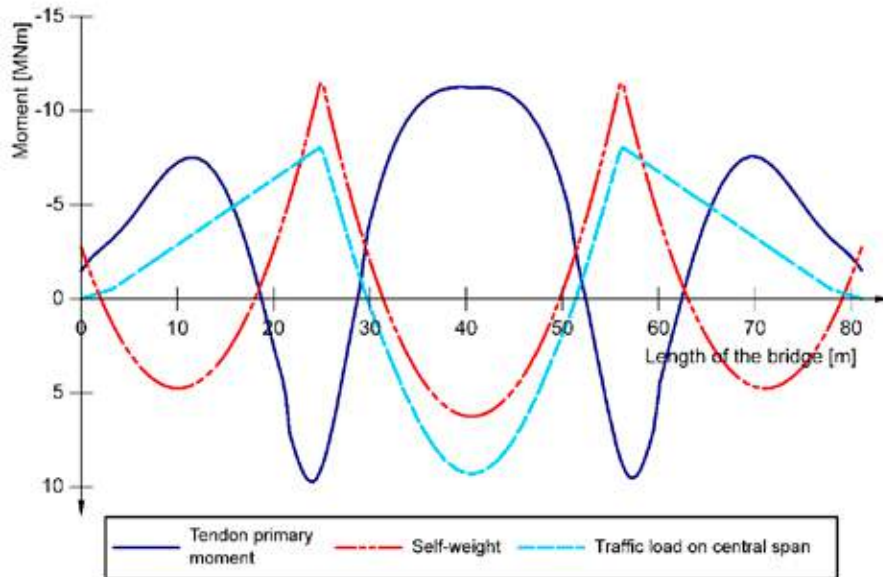

Figure 8 – Bending moments due to loads in characteristic combination of cracked bridge.

The abbreviation 'CHAR_Traffic_All' in Figure 9 and 10 means that non-linear calculations have been made with characteristic load combination while traffic load was the leading action and all loads were acting in the bridge. The abbreviation 'Elastic' means that calculations have been made using linear material properties while other assumptions were the same as above.
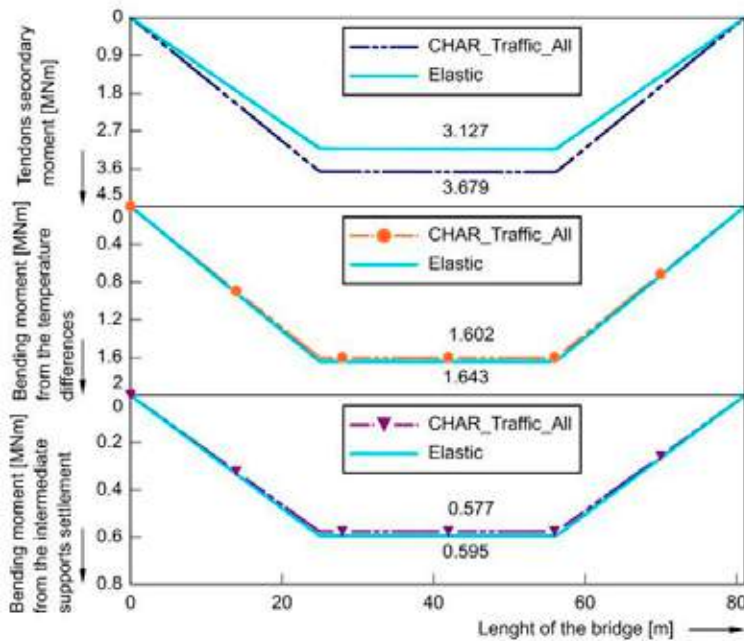
Figure 9 – Stresses from restrained deformations in the elastic state and after the stiffness degradation from loads.
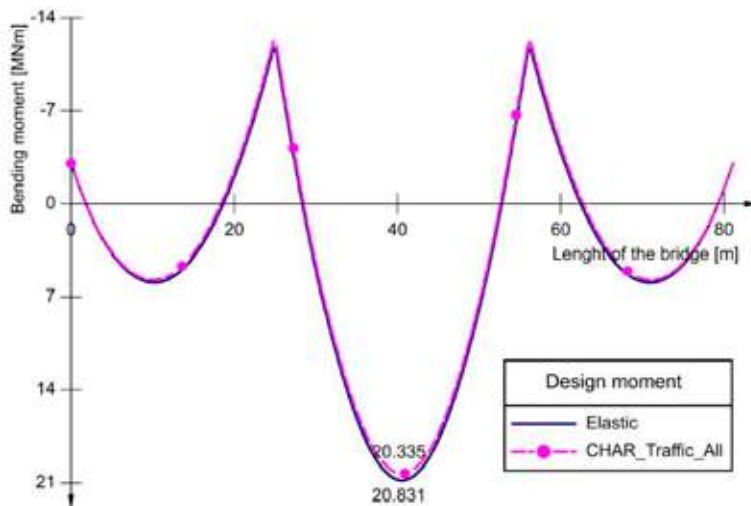

Figure 10 – Bending moments from all loads (excl. primary moment from prestressing force) in characteristic combination (with traffic load as leading action) and elastic state.

The difference between the elastic state and the characteristic combination with vehicle traffic load as the leading action is about 0.5 MNm at the middle of the central span. In the

characteristic combination, about 1 MNm of dead load and traffic load bending moments were transferred from the central span to the intermediate supports. Because the secondary moment of the tendon prestressing force increased at the same time, the difference of total bending moment decreased by only 0.5 MNm at the middle of the central span. Figure 10 shows that the changes were small compared to total bending moments.

In characteristic combination with temperature load leading actions, the bending moments from linear temperature difference were about the same as in the elastic state. When traffic load was the leading action, the bending moments from linear temperature difference were decreased because slightly more cracking occurred as shown in Table 3. In the characteristic combination, cracking of the bridge superstructure was significant only when traffic load was the leading action and maximum stresses were at the central span.

The values in parentheses in Table 3 and Table 4 are the results from calculations with serviceability limit state material models while loads were factored with ultimate limit state load factors. This calculation was done to provide results with loading that is closer to the maximum design load.

Table 3 – Stresses from linear temperature difference on cracked bridge in relation to elastic state (results where loads were factored with ultimate limit state load factors).

Max bending moment at	Loads included/ Leading action	THERMAL	TRAFFIC
Central span	All loads, excluding support settlement	1.03 (0.98)	0.99 (0.93)
	All loads	1.02 (0.95)	0.97 (0.91)
Intermediate supports	All loads, excluding support settlement	1.05 (1.05)	1.05 (0.98)
	All loads	1.05 (1.05)	1.05 (0.98)

Secondary bending moment of prestressing force from characteristic combination in relation to the elastic state is presented in Table 4. The results show that the secondary bending moment increased when the central span of the superstructure cracked under the characteristic combination of loads. Bending moment increased by up to 18% compared to the elastic state, which primarily occurred with load combinations where stresses in central span and cracking were larger than in intermediate supports. When observing secondary effects with load combinations where the maximum bending moment was at the intermediate support, the superstructure cracked at both the central span and intermediate supports which reduced the secondary moment from prestressing compared to the elastic state, and total bending moments remained essentially unchanged.

The results show that the relative change in bending stiffness of different parts of the bridge was the most important factor in determining the magnitude of effects from restrained deformations.

Table 4 – Secondary moment due to post-tensioning with design reinforcement in relation to elastic state (results where loads were factored with ultimate limit state load factors).

Max bending moment at	Loads included/ Leading action	THERMAL	TRAFFIC
Central span	All loads, excluding support settlement	1.04 (1.17)	1.13 (1.29)
	All loads	1.08 (1.22)	1.18 (1.34)
Intermediate supports	All loads, excluding support settlement	0.97 (0.98)	0.98 (0.89)
	All loads	0.96 (0.98)	0.98 (0.81)

Figure 9 shows that the secondary moment from prestressing resulted in considerably larger stresses than that caused by support settlement or linear temperature difference when the central span was cracked. If the total load on the central span was increased, the increase in secondary moment would also be larger, as shown in the results in parenthesis in Table 4. As the loading on the central span decreased, the stresses from the secondary moment also decreased. When bending stiffness is reduced uniformly in the length of the bridge superstructure, or in the central span and intermediate supports simultaneously, the tendon secondary moment remains unchanged compared to the elastic state. The behaviour of the secondary bending moment when bending stiffness changes due to cracking is entirely different compared to the effects from linear temperature difference. Currently, secondary bending moment from prestressing is often grouped with other restrained deformations, and its effects are relieved accordingly.

4.   CONCLUSIONS

The structural design of a bridge is usually simplified by using linear elastic models, and the non-linearity in the actual behaviour of the structure is taken into account with empirical factors. In order to provide more information on this non-linear behaviour, a three-span post-tensioned concrete bridge designed in 2014 was studied with a structural model that would take into account the cracking of the concrete superstructure. The results of this study are summarised in Figure 11, which shows how the stresses of the bridge superstructure from restrained deformations change when the bending stiffness is decreased from loading in the central span only or in the central span and intermediate supports. The study revealed that, as central span bending stiffness decreased from loading, stresses from support settlement and linear temperature difference also decreased while secondary moment from prestressing was found to increase. When bending stiffness decreased from loading in the central span as well as in the intermediate supports, stresses from all restrained deformations decreased.

It is usual when designing a new bridge to reduce stresses caused by restrained deformations due to creep and cracking of concrete, but in this case the behaviour of the structure was opposite. The change in bridge bending stiffness occurred gradually, under normal design loads. If bending stiffness would decrease uniformly in the whole length of the superstructure, such as due to creep, the secondary moment from prestress would remain unchanged.
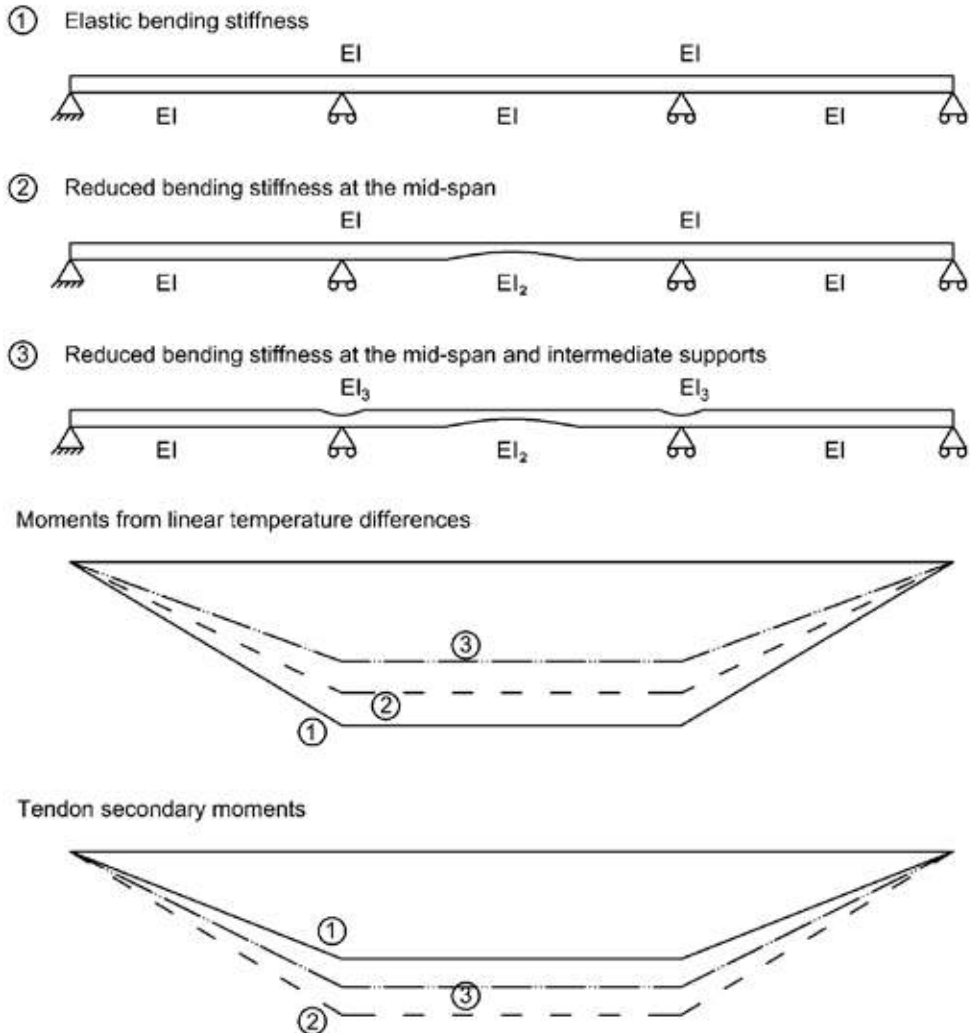
Figure 11 – Impact of change in bending stiffness on stresses from restrained deformations.

In the serviceability limit state, stresses from support settlement and linear temperature difference were not reduced as a result of cracking. Therefore, it would be justified to use stresses from linear elastic analysis when designing a new bridge. When creep was considered in the serviceability limit state, stresses decreased by up to 35% compared to the elastic state. The reduction in stresses was mainly due to the effect of creep on bending stiffness rather than cracking of the bridge. The effects of creep on the stresses were of an expected magnitude.

The increase in the secondary moment from prestress force was due to the cracking of the central span. The results indicate that the change in secondary moment from prestress depends on the location of the cracking of the superstructure.

This study on the behaviour of a post-tensioned bridge was conducted based on only one bridge cross-section with symmetrical spans, since the scope of the research was the effect of flexural cracking of the superstructure on the secondary bending moments in the case of an ordinary bridge structure. Parametrisation was excluded from the research, as the focus of this study was to test the calculation method and see how the structure would behave under some basic assumptions. The results of this study cannot be generalised due to these limitations. In the future, research should be done with parametrisation of several variables, including at least different reinforcement and span ratios, the variation in cross-section size and the variation in concrete strength classes. Results from future research should include generally applicable guidelines for design or for calculation of load-bearing capacity. The impact of cracking could also be examined with test loading of a continuous prestressed beam with a uniform load and support settlement.

ACKNOWLEDGEMENTS

REFERENCES

1. Arnold A: ”Zum Einfluss der Zwangschnittgrößen aus Temperatur bei Tragwerken aus Konstruktionsbeton mit und ohne Vorspannung,” Dissertation, Dortmund Techn. Univ., Dortumund, Germany, 2008. (In German).
2. Jalonen K: “Imposed and restrained deformations on concrete bridge,” *Master Thesis*, Tampere University of Technology, Tampere, Finland, 2016. (In Finnish.)
3. Liikenneviraston ohjeita 24/2014. 2014. Eurokoodin soveltamisohje – Siltojen kuormat ja suunnitteluperusteet NCCI 1 (5.9.2014) (Guidelines of the Finnish Transport Agency). 24/2014. 2014. Guidelines for the application of the Eurocode – Bridge loads and basis of structural design NCCI 1 (5.9.2014)). Liikennevirasto, Helsinki, Finland. (In Finnish.)
4. Liikenneviraston ohjeita 25/2014. 2014. Eurokoodin soveltamisohje – Betonirakenteiden suunnittelu NCCI 2 (16.9.2014) (Guidelines of the Finnish Transport Agency 25/2014. 2014. Guidelines for the application of the Eurocode – Design of Concrete Structures NCCI 2 (16.9.2014)). Liikennevirasto, Helsinki, Finland, 2014. (In Finnish.)
5. Liikenneviraston ohjeita xx/2015 Siltojen kantavuuslaskentaohje (Kommenttiversio) (Guidelines of the Finnish Transport Agency xx/2015 Guidelines for assessment of bridges (Comment version)). Liikennevirasto, Helsinki, Finland, 2014. (In Finnish.)
6. SFS-EN 1991-1-5. Eurocode 1: Actions on structures. Part 1-5: General actions. Thermal actions. Suomen Standardoimisliitto ry. Finland, 2005.
7. SFS-EN 1992-1-1. Eurocode 2: Design of concrete structures – Part 1-1: General rules and rules for buildings. Suomen Standardoimisliitto ry. Finland, 2005.
8. SFS-EN 1991-2. Eurocode 1: Actions on structures. Part 2: Traffic loads on bridges. Suomen Standardoimisliitto ry. Finland, 2009.
9. SFS-EN 1990. Eurocode – Basis of structural design. Suomen Standardoimisliitto ry. Finland, 2010.
10. SFS-EN 1992-2. Eurocode 2: Design of concrete structures. Concrete bridges. Design and detailing rules. Suomen Standardoimisliitto ry. Finland, 2009.
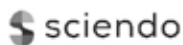
sciendo

Impact of Accelerated Carbonation on Microstructure and Phase Assemblage

Andres Belda Revert
PhD student
Norwegian University of Science and Technology (NTNU),
Department of Structural Engineering
Richard Birkelands vei 1 A, 7491. Trondheim
andres.b.revert@ntnu.no

Klaartje De Weerdt
PhD, Associate Professor
Norwegian University of Science and Technology (NTNU),
Department of Structural Engineering
Richard Birkelands vei 1 A, 7491. Trondheim
klaartje.d.weerdt@ntnu.no

Ulla Hjorth Jakobsen
PhD, Senior Consultant
Danish Technological Institute (DTI)
Concrete Centre
Gregersensvej 4, DK 2630 Taastrup
uhj@teknologisk.dk

Mette Rica Geiker
PhD, Professor
Norwegian University of Science and Technology (NTNU),
Department of Structural Engineering
Richard Birkelands vei 1 A, 7491. Trondheim
mette.geiker@ntnu.no

ABSTRACT

The paper summarizes preliminary results on characterization of the microstructure and phase assemblage of mortar and concrete samples containing Portland and Portland-fly ash cement carbonated at either natural conditions, 60% *RH* and 1% CO_2, 90% *RH* and 5% CO_2 or 60% *RH* and 100% CO_2. Different characterization techniques were used: thermogravimetric analysis to study the solid phases, SEM-EDS point analysis to investigate the chemical composition of the

solid phases, optical microscopy to investigate the microstructure, and cold water extraction to characterize the chemical composition of the pore solution. The combined results on microstructure and phase assemblage indicate that carbonation up to 5% CO_2 appears representative for natural carbonation. Pore solution analysis revealed similar trends for the three accelerated carbonation conditions.

Key words: Carbonation, microstructure, solid phases, pore solution, Portland-fly ash cement.

1. INTRODUCTION

Carbonation is the reaction of the CO_2 present in the atmosphere with the phases in the hydrated cement paste. Carbonation causes a change in the microstructure, solid phases, and lowers the pH of the pore solution [1]. Carbonation in natural exposure is a slow process. For performance testing, carbonation is therefore usually accelerated by means of optimal relative humidity (60-70%) [1] and increased CO_2 concentration (25-250 times higher than natural) [2]. However, it is not clear to which extent the microstructure and phase assemblage developed upon accelerated carbonation mirrors that for natural carbonation.

Castellote et al. [3] investigated cement paste exposed to various CO_2 concentrations (0.03 (natural), 3, 10 and 100%). The samples were prepared with Portland cement and a water-to-binder ratio (w/b) of 0.5. Phase changes due to carbonation were investigated using ^{29}Si solid-state nuclear magnetic resonance (^{29}Si MAS-NMR), thermogravimetry (TGA) and X-Ray Diffraction (XRD). The authors concluded that accelerated carbonation up to 3% CO_2 gives similar products compared to natural carbonation. For 10% and 100% CO_2 the C-S-H was more extensively carbonated and silica gel was formed.

Auroy et al. [4] investigated cement paste (w/b = 0.40) containing a ternary blend (50% PC + 25% FA + 25% GGBFS). Exposure conditions were 25℃, 55% RH, and 0.04 or 3% CO_2. Carbonation was investigated using XRD, TGA and ^{29}Si NMR They found that similar products were formed upon carbonation at the two different CO_2 concentrations. Some calcium hydroxide was found in the carbonated area, and C-S-H decomposed to a Ca-enriched silica gel (Ca/Si ≈ 0.5). The calcium hydroxide and carbonate contents were similar in both exposures. After further research using XRD, TGA and ^{29}Si NMR the authors confirmed that the carbonation products formed at 3% CO_2 were representative of the products formed at long term natural carbonation [5]. In agreement, Shah et al. using XRD, TGA and SEM-EDS point analysis found that the products formed at 60% RH, 3% CO_2 compared to products formed at natural carbonation [6]. No results on carbonation at relative humidity higher than 75% were found.

Table 1 presents the summary of pore solution investigations of carbonated cementitious materials found in the literature. For the studies reported in [7, 8], the pore solution was obtained by high pressure squeezing on moisturized samples. Carbonated concrete is usually dry and therefore pore solution squeezed by mechanical procedures requires that the samples are moisturized. The water added in the samples in [7, 8] was however not reported and the dilution was not taken into account when determining the pore solution composition. For the studies reported in [9, 10] cold water extraction (CWE) and inductively coupled plasma mass spectrometry (ICP-MS), a rapid leaching method on ground mortar or concrete, was used to study the pore solution composition.

All studies show that the amount of alkali metals (Na and K) in the carbonated pore solution is reduced compared to pore solution of non-carbonated samples [11]. Anstice et al. [7] found similar amounts of alkali metals in the pore solution of carbonated mortars (first carbonated and then moisturized) at different CO_2 concentrations while higher amounts of sulphates and chlorides were found in the samples exposed to 100% CO_2. Pu et al. [8] reported higher amounts of free alkali metals compared to [7]. The addition of fly ash reduces the amount of alkali metals in the pore solution in non-carbonated samples [11]. The studies reported in [9, 10] using CWE showed that the amount of free alkali metals in the pore solution of Portland cement and Portland-fly ash cement mortar were similar when carbonated at 60% *RH,* 1% CO_2, .

The current paper summarizes observations of the impact of different exposure conditions on the microstructure and phase assemblage of carbonated mortar and concrete. Various techniques were applied: SEM-EDS point analysis (chemical composition of the solid phases), optical microscopy (microstructure), cold water extraction (chemical composition of the pore solution), and thermogravimetric analysis (solid phases).

The aim was to characterize the influence of the exposure condition on the carbonation reaction products. The investigation was part of the larger project with the overall purpose to study the impact of fly ash on the corrosion rate of steel embedded in carbonated concrete. In the corrosion study, exposure to 90% *RH,* 5% CO_2 was used to promote a relatively high carbonation rate (5% CO_2) and at the same time a relatively high corrosion rate when carbonated [12]. This to limit the need for changing the exposure condition before the corrosion studies. Moisture has a strong impact on the corrosion rate and a well-defined moisture state facilitates the comparison of corrosion rate data in different samples.

Table 1 – Summary of pore solution investigations in carbonated mortar and cement paste found in the literature. T is given in [°C], RH in [%] and CO_2 in [%].

Ref	Cement	w/b	Exposure			Technique	Composition				Unit
			T	RH	CO_2		Na	K	Cl	S	
[7]	CEM I	0.6	22	75[a]	100	Squeezed pore solution (300 MPa) + Ion chromatographic analysis	4	10	21	17	mmol/l
		0.6	22		5		4	9	13	20	
		0.6	22		0.03		3	15	4	1	
		0.6	22	65[b]	100		2	6	11	15	
		0.6	22		5		7	16	12	24	
		0.6	22		0.03		4	13	8	11	
		0.6	22	55[c]	100		5	11	23	18	
		0.6	22,		5		0	1	8	2	
		0.6	22		0.03		3	26	8	2	
		0.6	22	55[d]	100		10	17	23	20	
		0.6	22		5		1	1	11	7	
		0.6	22		0.03		1	1	9	5	
[8]	CEM I	0.5	20	40[e]	0	Squeezed pore solution (300 MPa) + pH meter	1.1	1020	-	-	mmol/l
		0.5	20	40[e]	5		0.2	190	-	-	
	CEM II/B-V (15% FA)	0.5	20	40[e]	0		0.9	580	-	-	
		0.5	20	40[e]	5		0.2	190	-	-	
[9]	CEM I	0.55	20	60[e]	0	CWE + ICP-MS	24	30	1	3	mmol/kg
		0.55	20	60	1		6	2	2	11	
		0.55	20	90[f]	0		26	30	0	1	
	CEM II/B-V (30% FA)	0.55	20	60[e]	0		17	23	1	1	
		0.55	20	60	1		5	2	2	12	
		0.55	20	90[f]	0		17	24	0	0	
		0.55	20	90	5		5	3	15	18	
[10]	CEM I	0.55	20	Sealed		CWE + ICP-MS	26	30	-	-	mmol/kg
	CEM I	0.55	20	60	1		4	2	-	-	
	CEM II/B-V (30% FA)	0.55	20	Sealed			18	22	-	-	
		0.55	20	60	1		3	1	-	-	
		0.40	20	60	1		3	1	-	-	

Note: Salt solutions used to keep *RH* at a certain value: [a]: sodium chloride, [b]: ammonium nitrate, [c]: magnesium nitrate, [d]: sodium dichromate, [e]: sodium bromide, [f]: barium chloride, CWE: Cold water extraction, ICP-MS: Inductively Coupled Plasma Mass Spectrometry

2.   EXPERIMENTAL

The experimental investigation comprises three sets of series. The investigated materials and exposure conditions (including the used legends) are given in Table 2 and Table 3, respectively. The legends for the samples combine material (fly ash replacement (FA)) and exposure (RH and CO_2), <% FA>-<% *RH*>-<% CO_2>, e.g. 30-60-1 is a sample containing 30% fly ash which was exposed to 60% *RH,* 1% CO_2.

Table 2 – Material and cement compositions investigated.

Description		Cement type according to EN 197 [13] and fly ash content (FA)		
		CEM I (0% FA)	CEM II/B-M (18% FA)	CEM II/B-V (30% FA)
Series 1	Concrete prisms	x	x	x
Series 2	Mortar prisms			x
Series 3	Mortar disks	x		x

Table 3 – Exposure conditions investigated (all 20°C except XC3 (16-22°C)).

	Non-carbonated				Carbonated		
	Sealed cured	Dried at 60%	Non-carb. sample	Natural XC3	60% RH, 1% CO_2	90% RH, 5% CO_2	60% RH, 100% CO_2
Legend	<%FA>-Sealed	<%FA>-60-0	<%FA>-Bulk	<%FA>-XC3	<%FA>-60-1	<%FA>-90-5	<%FA>-60-100
Series 1			x	x		x	
Series 2	x			x	x		
Series 3	x	x			x	x[*]	x

* only CEM II/B-V as CEM I samples were not fully carbonated

2.1 Samples

Three commercially available Norwegian cements were used: CEM I (0% FA), CEM II/B-M (18% FA) or CEM II/B-V (30% FA). Tables 4 and 5 provide the chemical composition of the cements.

For Series 1, concretes prism (120*150*260 mm) and wall elements (1200*1500*250 mm) were cast at a concrete plant from concrete (*w/b* = 0.55) containing all three cements. Further information on casting and compaction can be found in [12]. The concrete prisms were kept in the mould for three days and when demoulded wrapped in plastic for 11 days. After this period, the prisms were exposed to accelerated carbonation for 20 weeks. The walls were exposed to natural carbonation in sheltered condition (XC3). Drilled cores with a diameter of 100 mm were investigated.

For Series 2, mortar prisms (140*40*160 mm) containing CEM II/B-V and having *w/b* = 0.40 or 0.55 and paste-to-sand ratio (*p/s*) of 0.73 in volume were prepared. Further information on casting and compaction can be found in [10]. The mortars were cast in steel moulds and compacted using a vibrating table. Two 20-mm layers were compacted by applying 5 seconds of vibration for the *w/b* = 0.55 and 10 seconds for the *w/b* = 0.40 on each layer. After casting, the prism were covered with plastic for one day and subsequently stored sealed in plastic at 20°C for 13 days. At the age of 14 days, the mortar prisms were exposed for 9 weeks to different conditions.

For Series 3, mortars (*w/b* = 0.55) containing CEM I and CEM II/B-V were mixed and cast in polyethylene bottles 50 mm in diameter and 100 mm in height. Further information in casting and compaction can be found in [9]. Each bottle was filled in three layers and each layer jolt-compacted applying 30 strokes. The bottles were kept sealed at 20°C for two weeks and then wet-cut in disks of 15 mm in thickness using a saw. At the age of 14 days the disks were exposed to different carbonation conditions until they were fully carbonated. When the samples did not show any change in colour after spraying thymolphthalein on a freshly split sample they were classified as "fully carbonated".

Table 4 – Chemical composition and fineness of the cements used in Series 1 by XRF [% by mass].

Cement	% FA	SiO_2	Al_2O_3	Fe_2O_3	CaO	MgO	SO_3	P_2O_5	K_2O	Na_2O	Blaine [m^2/kg]
CEM I	0	19.6	4.9	3.1	60.8	2.3	3.7	0.1	0.9	0.5	548
CEM II/B-M	18	25.5	7.6	4.2	50.7	2.1	3.3	0.2	1.1	0.6	477
CEM II/B-V	30	28.4	8.8	4.4	46.9	2.2	2.7	0.2	1.2	0.6	459

Table 5 – Chemical composition and fineness of the cements used in Series 2, 3 by XRF [% by mass].

Cement	% FA	SiO_2	Al_2O_3	Fe_2O_3	CaO	MgO	SO_3	P_2O_5	K_2O	Na_2O	Blaine [m^2/kg]
CEM I	0	20.4	4.8	3.4	61.7	2.2	3.5	0.2	0.9	0.5	420
CEM II/B-V	30	29.5	10.8	4.5	44.6	2	3.2	0.4	1.1	0.5	501

2.2 Methods

Table 6 provides an overview of methods applied and the types of samples used.

Carbonation depth was detected spraying a pH indicator (thymolphthalein, 1%) on a freshly split surface (120*150 mm). For Series 1, carbonation depths were also determined on the thin sections (50*50 mm) using crossed polarized light.

Thin sections were prepared by the Danish Technological Institute according to NT Build 361 [14]. The concrete samples were impregnated with an epoxy resin containing fluorescent dye, mounted on a glass plate, ground to a thickness of 20 µm, and then covered with a glass. The thin sections were investigated with a Leica DM 2500P microscope using polarized, crossed polarized and fluorescent light.

Polished sections containing carbonated, transition zone, and non-carbonated concrete were prepared by the Danish Technological Institute according to [15]. The polished sections were investigated using scanning electron microscope Quanta 400 ESEM from FEI operated at high vacuum mode, accelerating voltage of 15 kV, spot size 5 and working distance of 10 mm were used. The specimens were carbon coated and the data were Proza corrected. The points were manually selected (typical 50 points in each zone) in the outer hydration products in carbonated and non-carbonated areas avoiding unreacted fly ash, clinker grains and aggregates. During scanning electron microscopy energy dispersive spectroscopy (SEM-EDS) point analysis a volume of approx. 1 μm^3 comprising a combination of different phases is analysed.

Cold water extraction (CWE) was applied as described in [16] on homogenized ground powder. The powder was passed through 80 µm mesh sieve and mixed with deionized water and filtrated. The filtrated solution was diluted and acidified. The composition of the filtrated solution was analysed using inductively coupled plasma mass spectrometry (ICP-MS). The chemical composition of the pore solution was determined in mmol/kg of mortar.

Thermogravimetric analysis (TGA) was performed on homogenized ground powder using a Mettler Toledo TGA/DSC 3+. Aluminium oxide crucibles were loaded with ca. 300 mg of powder. The samples were heated from 40°C to 900°C at a rate of 10°C/min while the oven was

purged with N_2 at 50 ml/min. The weight loss of the samples was monitored as a function of the temperature.

Table 6 – Methods applied.

Method		Carbonation depth	Microstructure	Solid phases		Pore solution
		pH indicator	Optical microscopy	SEM-EDS	TGA	CWE
Type of sample		Freshly split surface	Fluorescent thin section	Polished section	Powder	Powder
Series 1	Concrete prisms	x	x	x		
Series 2	Mortar prisms	x				x
Series 3	Mortar disks	x			x	x

3. RESULTS

3.1 Microstructure

Table 7 presents a summary of the characteristics of the microstructure of the paste of the samples investigated in Series 1. Micrographs illustrating the transition from carbonated (top) to non-carbonated (bottom) concrete are given in Figure 1. The micrographs were taken on a CEM II/B-V concrete sample exposed to 90% *RH*, 5% CO_2 using different light settings.

Generally, the concrete samples appear with a plane and intact surface, though several small micro-cracks formed in the plastic stage are present in the surface. The concrete containing CEM II with 18% FA seems to have the highest amount of surface defects.

All the concretes samples have a relatively porous paste as well as a somewhat inhomogeneous paste texture with alternating porous and less porous (patchy) areas. Furthermore, adhesions defects (formed in the plastic stage) between paste and aggregate are observed in most of the concretes. In general, the capillary porosity of the carbonated surface is higher compared to the capillary porosity of inner non-carbonated paste. However, this higher porosity is not considered an effect of carbonation but an initial defect, formed when the concrete was still plastic.

The paste of the concretes is, dependent on the exposure condition, carbonated to varying depths (Table 7). Deepest carbonation and the most even carbonation front is seen in the concretes exposed to 60% *RH,* 1% CO_2. The carbonation is also deep in the concretes exposed to 90% *RH,* 5% CO_2, but the carbonation front is very uneven, varying from 4-15 mm (Figure 1). Lowest depth of carbonation is seen in the natural exposed concrete where the maximum carbonation depth is 5 mm (Table 7).

The carbonation depths determined by the pH indicator and on the thin sections using crossed polarized light are comparable, taking into account the variation of the carbonation front as reported in [17], see Table 7.

Partially hydrated and non-carbonated cement grains are present in the carbonated paste, especially near the surface. This feature is most pronounced in the concretes containing CEM I and CEM II with 18% FA and exposed to natural carbonation or at 60% *RH,* 1% CO_2. In concrete containing CEM II with 30%FA, and in the concretes exposed to 90% *RH,* 5% CO_2 most of the cement grains in the carbonated paste are fully hydrated and the formed inner C-S-H is fully carbonated.

As the paste in general has a patchy appearance, the carbonated paste also appears patchy with less or even non-carbonated "islands" embedded in carbonated paste. The most distinct patchy feature is seen in concrete without fly ash, and to some extent in the concretes exposed to 90% *RH,* 5% CO_2.

The concretes containing CEM I and CEM II with 18% FA has a normal carbonation texture, whereas the concrete containing 30% FA a popcorn-like texture is observed.

Other characteristics which were investigated were the presence of CH in the carbonated area or in the bulk, the width of the transition zone from carbonated to non-carbonated concrete, adhesion and surface cracks, and the air content. A characteristic feature of the samples exposed to 90% and 5% CO_2 was a densification in front of the carbonation front. This issue should be investigated in more detail; potentially it is due to an accumulation of sulphates.

Overall, the microstructure of the carbonated concretes depended more on inhomogeneities prior to carbonation (mixing, casting) than on the exposure conditions.
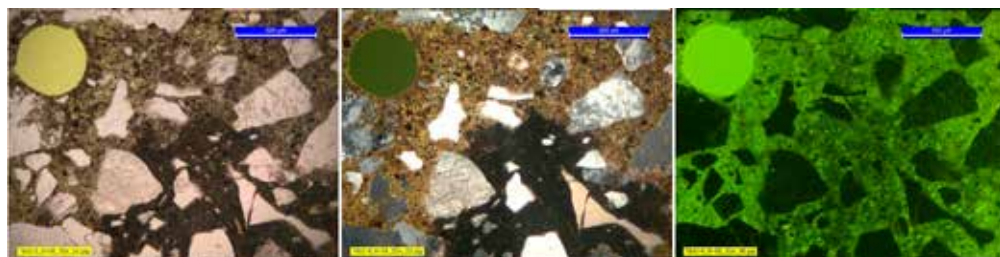
Figure 1 – Micrographs illustrating transition from carbonated (top) to non-carbonated (bottom) in 30-90-5 (Series 1). Optical microscopy on fluorescence epoxy impregnated thin sections. From left to right: polarized, crossed polarized and fluorescent light.

Table 7a and 7b – Characteristic microstructure of the carbonated and non-carbonated paste determined on thin sections and carbonation depth determined by thymolphthalein on companion samples (Series 1).

| Label | Xc Microscopy [mm] | Xc THY [mm] | Carbonated surface region | | | Paste porosity, rel. to non-carbonated paste |
			Front	Popcorn carb.	Non-carb. islands	
0-60-1	12	12-15	Even	-	Many	Slightly increased
18-60-1	12-14	17-20	Rel. even	-	Some	Slightly increased
30-60-1	20-22	22-25	Rel. even	X	None	Slightly increased
0-90-5	4-14	5-17	Un-even	-	Many	Increased
18-90-5	7-14	8-16	Un-even	-	Few	Increased
30-90-5	11-15	6-20	Un-even	X	Some	Increased
0-XC3	2-5	2.5-3	Un-even	-	Some	Slightly increased
18-XC3	2-5	3.5-5	Un-even	-	None	Slightly increased
30-XC3	4	2.5-4	Even	X	Few	Slightly increased

Note. Xc: carbonation depth (minimum and maximum), THY: thymolphthalein

Table 7b.

Label	Transition zone		Non-carbonated				
	Width [mm]	Porosity	Patchy	Paste porosity	CH	Air, rel. amount	Adhesion cracks
0-60-1	1.2	-	Distinct	High	High	High	Some
18-60-1	1.2	-	Somewhat	Medium	Medium	Low	Many
30-60-1	-	-	Weak	Medium	Low	Low	Some
0-90-5	1	Decreased	Distinct	High	High	High	Few
18-90-5	1	Decreased	Somewhat	Medium	Medium	Low	Few
30-90-5	-	Decreased	Somewhat	Medium	Low	Low	Few
0-XC3	0.8	-	Somewhat	High	High	High	Few
18-XC3	0.8	Decreased	Somewhat	Medium	Medium	Low	Some
30-XC3	1	-	Somewhat	Medium	Low	Low	Some

3.2   Solid phases

Figure 2 presents the differential weight loss curves of the investigated mortar disks (Series 3). Table 8 presents the calculated amounts of CH (calcium hydroxide) and C$\underline{C}$ (calcium carbonate) related to the weight at 850°C. Additionally, Table 8 includes the theoretical maximum amount of C$\underline{C}$ formed upon carbonation assuming all the CaO available in the systems carbonates, and the degree of carbonation related to this maximum amount.

Even for the samples exposed to 100% CO_2, the calculated degree of carbonation was less than 100%. This is probably due to incomplete carbonation of the clinker grains. When comparing the plain Portland cement (0%) samples, a slightly increased amount of carbonates was formed at 100% CO_2 compared to 1% CO_2 (degree of carbonation 70% versus 90%). Compared to 1% CO_2 exposure, the 100% CO_2 exposure led to a reduction of the peak(s) in the temperature range 100-150°C corresponding to calcium silicate hydrate (C-S-H), ettringite (AFt), monosulfate or monocarbonate (AFm) and gypsum. Similar trends are observed for mortar disks with 30% FA. The fly ash samples were also carbonated at 90% *RH,* 5% CO_2, which led to slightly less carbonates compared to carbonation at 60% RH (degree of carbonation 70% versus 80% and 90%).
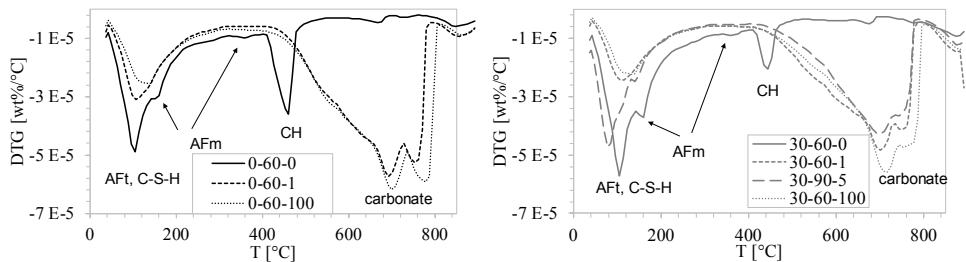
Figure 2 – Differential weight loss (DTG) for mortar disks (Series 3) exposed to 60% RH and 0%, 1% or 100% CO_2, and 90% RH, 5% CO_2. Left 0% FA, right 30% FA. After [9].

Table 8 – Measured amounts of CH and CC [% of weight at 850°C] and calculated theoretical maximum and degree of carbonation (rounded to nearest 5) for mortar disks (Series 3) exposed to 60% RH and 0%, 1% or 100% CO_2, and 90% RH, 5% CO_2.

	CH [%]	CC [%]	CC [%] Theoretical maximum	Degree of carbonation [%]
0-60-0	4.5	1		0
0-60-1	-	18	25	70
0-60-100	-	22		90
30-60-0	2	1		0
30-60-1	-	15	18	80
30-90-5	-	13		70
30-60-100	-	17		90

The chemical composition of the carbonation reaction products was investigated using SEM-EDS on the polished sections of carbonated and non-carbonated parts of the concrete samples (Series 1). The points were manually selected (typical 50 points in each zone) in the outer hydration products in carbonated and non-carbonated areas avoiding unreacted fly ash, clinker grains and aggregates. This investigation is also reported in [18]. Figure 3 presents a summary of the data. SEM-EDS point analysis data are presented as Si/Ca versus Al/Ca molar ratios in order to identify phases. In a dot plot, a data point lays in between the ideal stoichiometry of the phases it comprises. The ideal composition of the following hydration phases are included: ettringite (AFt), monosulphate (AFm), and portlandite (CH), in addition calcium carbonate (CC) is added. A certain volume is analysed in a SEM-EDS point analysis. This volume will typically contain a mixture of phases and the resulting point lies in between the stoichiometric compositions of these phases. The finer the intermixing of the phases is the fewer points will be near the stoichiometric compositions.

The approximate C-S-H composition of the non-carbonated concretes with fly ash (Si/Ca=0.65) and without fly ash (Si/Ca=0.5) was determined. The Si/Ca decreased to 0.15-0.35 upon carbonation due to the fine intermixing of decalcified C-S-H with CC. The CC originates from the C-S-H, CH and other carbonated hydrate phases. During carbonation, dissolution and precipitation reactions change both the phase assemblage and the distribution of the phases resulting in the fine intermixing of the decalcified C-S-H and CC. Based on the results presented in Figure 3 no clear difference in the composition of the reaction products in the carbonated concretes for the tested cements and exposures conditions could be observed.
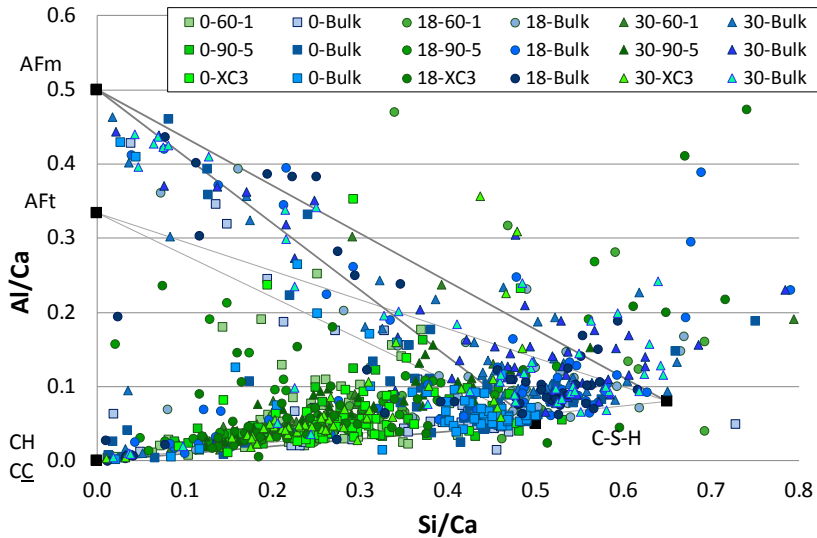
Figure 3 – SEM-EDS point analysis data presented as Si/Ca versus Al/Ca molar ratios for carbonated and non-carbonated concrete samples (Series 1). Squares: CEM I (0% FA), circles: CEM II/B-M (18% FA), triangles: CEM II/B-V (30% FA). Green colours: carbonated, blue colours: non-carbonated. After [18].

3.3 Pore solution composition

Data for pore solution analysis of mortar prisms from Series 2 are given in Figure 4. The results include data of the fully carbonated part of the exposed samples (according to the pH indicator) and of the sealed samples. The free alkali metal ion (Na and K) concentrations were lower in the carbonated samples compared to the sealed samples. The sodium and potassium concentrations in the carbonated mortars were not influence by the *w/b* (0.40 (30*-60-1) versus 0.55 (30-60-1)). In addition to the data given in Figure 4, the sodium and potassium concentrations of the samples exposed to natural carbonation were measured. These were found to be slightly higher (Na 7, and K 5 mmol/kg) than those of the same samples exposed to 60% *RH,* 1% CO_2. However, the measured higher free alkali metal contents in the naturally carbonated samples could be due to contamination of the samples with non-carbonated material due to a limited carbonation depth, about 2 mm, after 9 weeks of exposure.
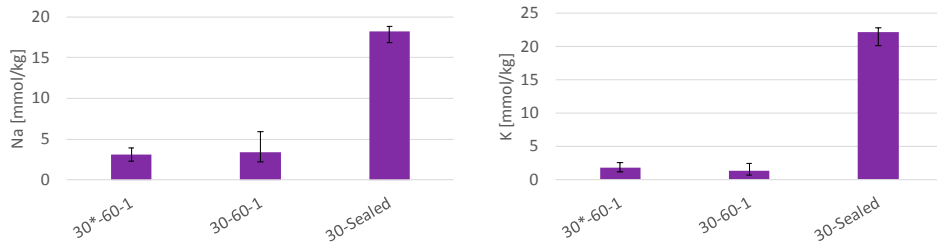
Figure 4 – Free alkali metal (Na and K) content (mmol/kg of mortar) using CWE on mortar samples from Series 2. Solid bars (average) and error bars (range) of 3 measurements. Sample 30*-60-1 has w/b = 0.40 and 30-60-1 w/b = 0.55. Partly after [10].

Figure 5 presents the free alkali metals, sulphur and chloride content of the mortar disks carbonated at different exposure conditions as well as sealed samples as reference (Series 3). The pore solution composition obtained using CWE yielded a comparable sodium and potassium content in the carbonated mortars, irrespective of the cement composition and the exposure. Similar to observations for Series 2 (Figure 4), the free sodium and potassium content was significantly reduced by carbonation. The free sulphur and chloride contents were considerably higher in the carbonated mortars compared to the non-carbonated mortars. The free sulphur content in the carbonated mortars was comparable for the two cements, but slightly higher in the samples exposed to 60% *RH*, 100% CO_2 than in the samples exposed to 60% *RH*, 1% CO_2. The free chloride content was slightly lower in the samples exposed to 100% CO_2 than the samples exposed to 1% CO_2. The fly ash samples exposed to 90% *RH*, 5% CO_2 showed comparable amounts of sulphur and chlorides to the samples carbonated at 60% *RH*, 100% CO_2.
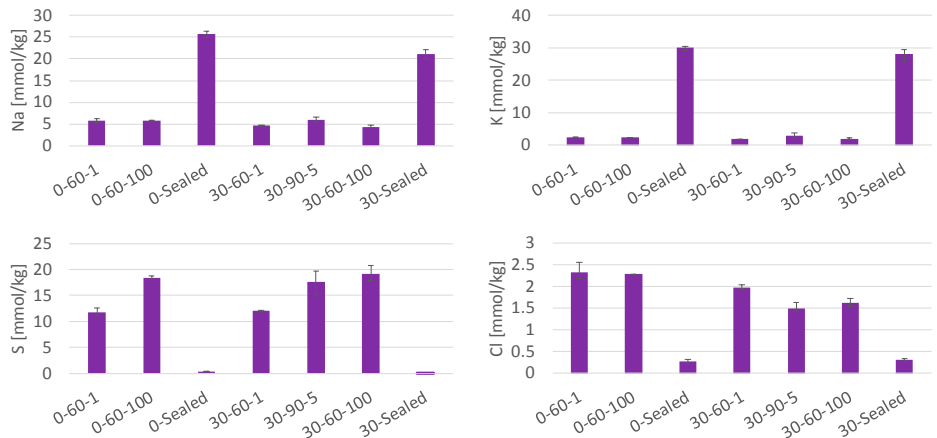
Figure 5 – Free alkali metal (Na and K), sulphur (S) and chloride (Cl) content (mmol/kg of mortar) using CWE on mortars from Series 3. Solid bars (average) and error bars (range) of 3 measurements. Partly after [9].

4.   DISCUSSION

Petrographic analysis of thin sections revealed that the microstructure of the carbonated samples (natural carbonation (XC3), 60% *RH*, 1% CO_2, or 90% *RH*, 5% CO_2) depended more on local initial plastic defects formed prior to carbonation than on the exposure condition or cement type. The concrete containing 30% FA presented a popcorn-like texture in the carbonated zone. As carbonation is a dissolution-precipitation reaction, a difference in the degree of saturation could lead to different distribution. However, with the applied techniques such features were not observed.

TGA indicated that the phase assemblage of samples carbonated at 1% and 100% CO_2 (60% *RH*, 20°C) is comparable. Difference in moisture content between samples carbonated at 60% and 90% RH does not allow detailed comparison.

SEM-EDS point analysis showed that the composition of the outer reaction products formed upon carbonation were independent of the exposure conditions (XC3, 60% *RH*, 1% CO_2, or 90% *RH*, 5% CO_2) and cement types (0-30% fly ash) investigated.

The pore solution analysis of the carbonated samples showed that sodium and potassium are bound by the reaction products upon carbonation, while sulphate and chloride are released into the pore solution. Higher amounts of alkali were found in the naturally carbonated samples compared to samples exposed to 1% CO_2, but it is not clear whether this was due to either the exposure condition or intermixing of carbonated and non-carbonated material during the sampling. The three accelerated carbonation exposure conditions resulted in comparable pore solution compositions.

Table 9 presents a summary of the findings. In summary, the results suggests that accelerated carbonation at 90% *RH*, 5% CO_2 might be used for corrosion studies.

Table 9 – Summary of the of findings on the difference in microstructure and phase assemblage due to variation in exposure conditions during carbonation.

Exposure	Method	Findings
XC3 60% *RH*, 1% CO_2	Optical microscopy	• The microstructure of carbonated samples was similar regardless cement type and exposure condition except that the C<u>C</u> had a popcorn-like texture in the 30% FA samples.
90% *RH*, 5% CO_2	SEM-EDS	• The chemical composition of the outer reaction products was similar regardless type and exposure condition.
60% *RH*, 1% CO_2 60% *RH*, 100% CO_2 90% *RH*, 5% CO_2	CWE + ICP-MS	• The amount of free alkali metals (Na and K) upon carbonation was similar regardless the exposure condition and cement type. • The amount of sulphates increased slightly upon carbonation at 90% *RH*, 5% and 60% *RH*, 100% CO_2 compared to 60% *RH*, 1% CO_2. • The amount of chlorides decreased slightly upon carbonation at 90% *RH*, 5% and 60% *RH*, 100% CO_2 compared to 60% *RH*, 1% CO_2.
	TGA	• Carbonation at 100% CO_2 slightly increased the amount of carbonates and reduced the phase in the 100-150°C range compared to carbonation at 1% CO_2. At 90% *RH*, 5% CO_2 slightly less carbonates were formed compared to 60% *RH*, 1% CO_2.
XC3 60% *RH*, 1% CO_2	CWE + ICP-MS	• The results are non-conclusive due to the limited carbonation of the naturally carbonated samples.

5.   CONCLUSIONS

The influence of the exposure condition on the carbonation reaction products was studied to assess the applicability of exposure at 90% *RH*, 5% CO_2 of samples for corrosion rate studies of steel embedded in carbonated concrete.

The results suggest that accelerated carbonation at 90% *RH*, 5% CO_2 might be used for corrosion rate studies. The influence of the exposure conditions was minor compared to the changes upon carbonation (from non-carbonated to carbonated state).

ACKNOWLEDGEMENTS

REFERENCES

1. Bertolini L, Elsener B, Pedeferri P, Redaelli E & Polder R: "Chapter 5: Carbonation-induced corrosion. Corrosion of steel in concrete," Weinheim, Germany, Wiley-VCH Verlag GmbH & Co, 2013. pp. 79-91.
2. Harrison TA, Jones MR, Newlands MD, Kandasami S & Khanna G: "Experience of using the prTS 12390-12 accelerated carbonation test to assess the relative performance of concrete," *Magazine of Concrete Research*, Vol. 64, 2012, pp.737-47.
3. Castellote M, Fernandez L, Andrade C & Alonso C: "Chemical changes and phase analysis of OPC pastes carbonated at different CO_2 concentrations," *Materials and Structures*, Vol. 42, 2009, pp. 515-25.
4. Auroy M, Poyet S, P. LB, Torrenti J-M, Charpentier T & Moskura M: "Representativeness of accelerated carbonation testing of cement pastes," *Proceedings*, XXII Nordic Concrete Research Symposia, Reykjavik, Iceland, 2014, pp. 447-450.
5. Auroy M, Poyet S, Le Bescop P, Torrenti J-M, Charpentier & T, Moskura M: "Comparison between natural and accelerated carbonation (3% CO_2): Impact on mineralogy, microstructure, water retention and cracking," *Cement and Concrete Research*, Vol. 109, 2018, pp. 64-80.
6. Shah V, Scrivener K, Bhattacharjee B & Bishnoi S: "Changes in microstructure characteristics of cement paste on carbonation," *Cement and Concrete Research*, Vol. 109, 2018, pp. 184-97.
7. Anstice DJ, Page CL, & Page MM: "The pore solution phase of carbonated cement pastes," *Cement and Concrete Research*, Vol. 35, 2005, pp. 377-83.
8. Pu Q, Jiang L, Xu J, Chu H, Xu Y & Zhang Y: "Evolution of pH and chemical composition of pore solution in carbonated concrete," *Construction and Building Materials*, Vol. 28, 2012, pp. 519-524.
9. Langedal SL: "Investigation of resistivity, porosity and pore solution composition in carbonated mortar prepared with ordinary Portland cement and Portland-fly ash cement," *Master Thesis*, Norwegian University of Science and Technology, Trondheim, Norway, 2018.
10. De Weerdt K, Plusquellec G, Belda Revert A, Geiker MR & Lothenbach B: "Effect of carbonation on the pore solution of mortar," Submitted to *Cement and Concrete Research*, 2018.
11. Vollpracht A, Lothenbach B, Snellings R & Haufe J: "The pore solution of blended cements: a review," *Materials and Structures*, Vol. 49, 2015:1-27, 2016, pp. 3341–3367.
12. Belda Revert A: "Corrosion in carbonated fly ash concrete," *PhD Thesis*, Norwegian University of Science and Technology, Trondheim, Norway, 2018.
13. EN-197-1. Cement - Part 1: Composition, specifications and conformity criteria for common cements, 2011.
14. Nordtest- NT Build 361. Concrete, hardened: Water-cement ratio, 1991.
15. Detwiler RJ, Powers LJ, Jakobsen UH, Ahmed WU, Scrivener K & Kjellsen KO: "Preparing Specimens for Microscopy," *Concrete International*, Vol. 23, 2001, pp. 50-58.
16. Plusquellec G, Geiker MR, Lindgård J, Duchesne J, Fournier B & De Weerdt K: "Determination of the pH and the free alkali metal content in the pore solution of concrete: Review and experimental comparison," *Cement and Concrete Research*, Vol. 96, 2017, pp. 13-26.
17. Belda Revert A, De Weerdt K, Hornbostel K & Geiker M: "Carbonation Characterization of Mortar with Portland Cement and Fly Ash, Comparison of Techniques," *Nordic Concrete Research*, Vol. 54, 2016, pp. 60-76.

18. Belda Revert A, De Weerdt K, Geiker MR & Jakobsen UH: "SEM-EDS analysis of products formed under natural and accelerated carbonation of concrete with CEM I, CEM II/B-M and CEM II/B-V," *Proceedings*, XXIII Symposium on Nordic Concrete Research & Development, Aalborg, Denmark, 2017, pp. 85-88.